

2008

## **Design and Fabrication of a Wireless Strain Gage for Gas Turbine Engine Applications**

Carlos Daniel Arellano Echeverria  
*University of Rhode Island*

Follow this and additional works at: <https://digitalcommons.uri.edu/theses>

Terms of Use

All rights reserved under copyright.

---

### **Recommended Citation**

Arellano Echeverria, Carlos Daniel, "Design and Fabrication of a Wireless Strain Gage for Gas Turbine Engine Applications" (2008). *Open Access Master's Theses*. Paper 1387.  
<https://digitalcommons.uri.edu/theses/1387>

This Thesis is brought to you by the University of Rhode Island. It has been accepted for inclusion in Open Access Master's Theses by an authorized administrator of DigitalCommons@URI. For more information, please contact [digitalcommons-group@uri.edu](mailto:digitalcommons-group@uri.edu). For permission to reuse copyrighted content, contact the author directly.

DESIGN AND FABRICATION OF A WIRELESS STRAIN GAGE

FOR GAS TURBINE ENGINE APPLICATIONS

BY

CARLOS DANIEL ARELLANO ECHEVERRIA

A THESIS SUBMITTED IN PARTIAL FULFILLMENT OF THE

REQUIREMENTS FOR THE DEGREE OF

MASTER OF SCIENCE

IN

ELECTRICAL ENGINEERING

UNIVERSITY OF RHODE ISLAND

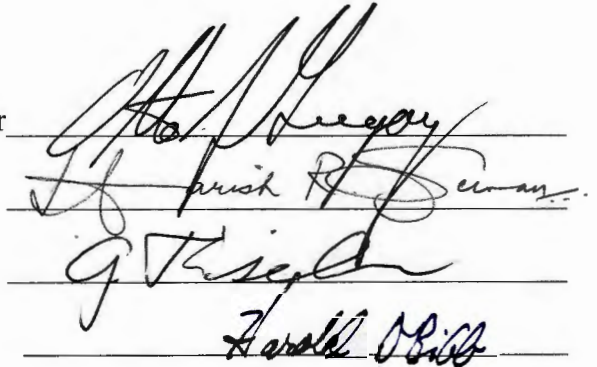
2008

MASTER OF SCIENCE THESIS  
OF  
CARLOS DANIEL ARELLANO ECHEVERRIA

APPROVED:

Thesis Committee:

Major Professor

  
The image shows four handwritten signatures on horizontal lines. The first signature is the most prominent and appears to be 'A. P. Gregory'. The second signature is 'Joseph R. Seymour'. The third signature is 'G. Thiel'. The fourth signature is 'Harold B. Biss'.

DEAN OF THE GRADUATE SCHOOL

UNIVERSITY OF RHODE ISLAND

2008

## **Abstract**

This thesis describes the design and fabrication of a wireless strain gage (WSG) prototype that utilizes a radio-frequency (RF) transponder for the compressor section of a gas turbine engine. The passive transponder will be printed, welded or deposited directly onto the compressor blades, and thus several key issues have to be addressed in the design of the distributed-element microwave circuit. Some of these issues are the temperature inside the engine, which may vary from 300 °F to 1,600 °F; the large “g” forces experienced by the blades rotating at 12,000 RPM; the RF transponder thickness, which should be below that of the boundary layer thickness (~ 800 microns) so the gas flow path through the engine is not affected. The footprint of the RF transponder circuit should not be larger than a few millimeters in any direction to accurately measure strain. The proposed WSG concept employs a capacitive/inductive RF transponder design with a specific resonant frequency, which responds to a short band pulse of energy from a transceiver module, such that the return signal has been modulated by the strain transmitted by the component. The goal is to correlate the frequency shift of the modulated signal to the strain in the substrate. The specifics of the transceiver module are beyond the scope of this research. However, a literature review was conducted to determine some possible technologies and approaches to solve this problem. Specifically, this research explored four different approaches for the design and fabrication of RF transponders; including one based on thin film planar structures; one based on thick film technology; one based on a “free standing” structure with a buckled-beam capacitor and one with an antenna being the actual sensing element. Results from this investigation have shown that the “free standing” structures yielded the largest gage factor, i.e. ~1000, compared to the thin-film and thick-film transponders which had gage factors between 11 and 14.

## **Acknowledgements**

I would like to express my gratitude to my advisor, Dr. Otto J. Gregory, for his support, guidance, advice and encouragement throughout my research project and thesis work at the University of Rhode Island. In addition, I appreciate his kindness and willingness to help me in any situation.

I would also like to thank the other members of my thesis committee, Dr. Godi Fischer and Dr. Harish Sunak, who provided valuable comments and suggestions during the writing of this thesis.

To my dearest friends, Rocio Escalante and Gema Viñuales, I extend my deepest thankfulness for their endless encouragement, motivation and invaluable support.

I feel a deep sense of gratitude for my parents who taught me the values needed to achieve my goals, who believed in me, kept endlessly encouraging me to continue my work, and gave me the foundation that guided me to be standing where I am today.

## Table of Contents

Abstract.....	ii
Acknowledgements .....	iii
Table of Contents .....	iv
List of Tables .....	vii
List of Figures.....	viii
CHAPTER 1 Introduction .....	1
1.1 Gas-turbine engine environment .....	1
1.2 Research objective.....	4
1.3 Wireless strain gage concept.....	5
CHAPTER 2 Literature review.....	7
2.1 Surface Acoustic Wave (SAW) devices .....	7
2.1.1 Nature of surface acoustic waves .....	8
2.1.2 Principle of operation of SAW sensors.....	9
2.1.3 Interdigital Transducer (IDT).....	9
2.1.4 Wireless SAW devices.....	11
2.1.5 Torque SAW sensors .....	15
2.1.6 Proposed SAW design for the WSG concept and shortcomings .....	17
CHAPTER 3 Thin/thick film designs and simulations .....	20
3.1 Thin film approach: parallel capacitor vs interdigital capacitor .....	20
3.2 Thin film interdigital capacitor: design parameters and simulations .....	23
3.3 Thick film interdigital capacitor: design parameters and simulations.....	30
CHAPTER 4 Free standing structure approach.....	39
4.1 Development of the buckled beam capacitor concept.....	40

4.1.2	Design parameters .....	43
4.1.3	Expected base capacitance and gage factor .....	46
4.2	Antenna strain gage design .....	47
4.2.1	Antenna gage configurations.....	49
CHAPTER 5	Fabrication process .....	53
5.1	Fabrication steps of thin-film interdigital capacitor .....	53
5.2	Fabrication steps of thick-film capacitor .....	58
5.3	Fabrication steps of buckled beam capacitor .....	61
5.4	Fabrication steps of antenna strain gage .....	64
CHAPTER 6	Testing and results .....	66
6.1	Thin-film capacitor: analysis and results .....	67
6.2	Thick-film capacitor: analysis and results .....	69
6.3	Buckled beam capacitor: analysis and results .....	70
6.3.1	Second buckled beam cap design: shorter top rail .....	73
6.3.2	Third buckled beam capacitor design.....	74
6.4	Antenna strain gage: analysis and results .....	76
CHAPTER 7	Conclusions .....	81
CHAPTER 8	Future work .....	84
8.1	Temperature compensation .....	84
8.2	Dynamic testing.....	85
APPENDIX A	SAW resonator design .....	87
APPENDIX B	Design and simulations of thin-film interdigital capacitor.....	91
APPENDIX C	Sputtering procedure.....	95
APPENDIX D	Fabricated thin-film and thick-film capacitors.....	96
APPENDIX E	Additional buckled beam capacitor designs .....	99

APPENDIX F Laser-welding machine parameters.....	104
APPENDIX G Fabricated antenna gage prototypes with modified parameters.....	106
APPENDIX H Frequency shift vs deflection for antenna strain gage .....	107
APPENDIX I Additional antenna gage measurement details.....	108
Bibliography .....	109



## List of Tables

Table 2.1 Physical properties of PVDF .....	17
Table 2.2 Piezoelectric and acoustic properties of PVDF .....	18
Table 2.3 Electrical properties of PVDF .....	18
Table 3.1 Sets of parameters for interdigital capacitor .....	22
Table 3.2 Comparison of capacitance values and gage factors .....	22
Table 3.3 Design parameters of thin-film capacitor.....	24
Table 3.4 Design parameters of thick film capacitor .....	32
Table 3.5 Comparison of capacitance values and gage factors .....	35
Table 4.1 Parameters of initial buckled beam capacitor design.....	45
Table 6.1 Capacitance measurements of thin-film capacitors .....	67
Table 6.2 Capacitance measurements of thick-film capacitor.....	69
Table 6.3 Buckled beam capacitor: component values .....	72

## List of Figures

Figure 1.1 Typical components of a turbine engine (DeAnna 2000).....	2
Figure 1.2 Temperature profile for gas-turbine engine (Pratt and Whitney 1982).....	3
Figure 1.3 Location of RF transponder and transceiver.....	5
Figure 1.4 Wireless Strain Gage System.....	6
Figure 2.1 Direction of propagation of SAW.....	8
Figure 2.2 SAW delay line showing configuration of IDTs (Morgan 1973).....	10
Figure 2.3 Schematic layout of a wireless SAW device (Reindl et al. 1998).....	12
Figure 2.4 SAW device configurations.....	12
Figure 2.5. Wirelessly interrogable SAW resonator (Pohl 1998).....	14
Figure 2.6 Comparison of RF responses of SAW delay lines and resonators.....	15
Figure 2.7 Typical setup for wireless torque SAW sensors (Pohl and Seifert 1997)..	16
Figure 3.1 Layout of parallel capacitor (left) and interdigital capacitor (right).....	21
Figure 3.2 Capacitance plot given by Sonnet Lite.....	25
Figure 3.3 Conductance plot of interdigital capacitor.....	26
Figure 3.4 Susceptance plot of interdigital capacitor.....	27
Figure 3.5 Resonance condition for different antenna lengths.....	28
Figure 3.6 Shift in resonant frequency when using a 6-mm antenna.....	29
Figure 3.7 Skin depth vs Frequency.....	31
Figure 3.8 Cross-section area of thick-film capacitor.....	33
Figure 3.9 Capacitance plot for thick-film capacitor given by Sonnet Lite.....	34
Figure 3.10 Resonant frequency of thick-film capacitor.....	36
Figure 3.11 Effect of the antenna in the thick-film capacitor resonant frequency.....	37
Figure 3.12 Shift in resonant frequency when using a 10-mm antenna.....	38

Figure 4.1 Capacitor model of a steel wire belt of a tire thread.....	40
(Matsuzaki and Todoroki 2005).....	40
Figure 4.2 Tire specimen and interdigital electrode configuration.....	41
(Matsuzaki and Todoroki 2005).....	41
Figure 4.3 Schematic of buckled beam amplification scheme .....	42
(Guo et al. 2004) .....	42
Figure 4.4 Schematic of the buckled beam capacitor.....	44
Figure 4.5 Side view of antenna element (not to scale); initial configuration.....	48
Figure 4.6 Side view of antenna height modified configuration (not to scale) .....	48
Figure 4.7 Top view of strain antenna design.....	50
Figure 4.8 Side view of strain antenna design .....	51
Figure 4.9 Top and side view of modified antenna gage design.....	52
Figure 5.1 YSZ ceramic constant strain beam.....	53
Figure 5.2 Photolithography and lift-off process .....	55
Figure 5.3 Front view of thin-film capacitor .....	56
Figure 5.4 Back view of thin-film capacitor: ground plane.....	57
Figure 5.5 Schematic of electric circuit for electroplating .....	59
Figure 5.6 Thick-film capacitor fabricated by electroplating .....	60
Figure 5.7 Cross-sectional view of buckled beam capacitor .....	62
Figure 5.8 Photograph of buckled beam capacitor.....	63
Figure 5.9 Antenna strain gage fabricated according to original parameters .....	65
Figure 6.1 Physical sketch of buckled beam capacitor; circuit components .....	71
Figure 6.2 Circuit model of buckled beam capacitor .....	71
Figure 6.3 Setup for measurements of buckled beam capacitor .....	72
Figure 6.4 Resonance of third buckled beam capacitor design; no beam deflection..	75

Figure 6.5 Resonance of third buckled beam capacitor design; 400 $\mu$ train .....	76
Figure 6.6 Resonance of antenna gage with solderable wire (no strain).....	78
Figure 6.7 Resonance of antenna gage with solderable wire bent 3mm.....	78
Figure 6.8 Second harmonic response - no beam deflection.....	79
Figure 6.9 Second harmonic response – 2 mm deflection.....	80
Figure 8.1 Antenna gage with temperature compensation approach.....	85
Figure 8.2 Dynamic test setup for RF strain measurements.....	86
Figure 8.3 Prototype for dynamic testing.....	86
Figure A.1 Lumped equivalent circuit of a SAW resonator.....	87
Figure A.2 Cross-section of an electrode section .....	89
Figure B.1 Strained and unstrained capacitance values for design 1 .....	91
Figure B.2 Strained and unstrained capacitance values for design 2.....	91
Figure B.3 3D view of interdigital capacitor .....	92
Figure B.4 Bottom layer of interdigital capacitor .....	93
Figure B.5 Top layer of interdigital capacitor .....	94
Figure D.1 Second fabricated thin-film capacitor on ceramic beam: 6mm.....	96
Figure D.2 Third fabricated thin film capacitor on ceramic beam: 6 mm.....	97
Figure D.3 Additional fabricated thick-film capacitor; antenna length: 10mm .....	98
Figure E.1 Buckled beam capacitor close-up and proposed modifications.....	99
Figure E.2 Schematic of modified buckled beam capacitor.....	100
Figure E.3 Fabricated capacitor with non-buckled shorter rails .....	101
Figure E.4 Fabricated buckled beam capacitor with 60 interdigital fingers.....	103
Figure G.1 Modified antenna gage with solderable wire .....	106
Figure G.2 Modified antenna gage with solderable wire .....	106
Figure H.1 Frequency shift vs deflection for antenna gage.....	107

## **CHAPTER 1 Introduction**

The current technology for measuring strain on compressor blades of a jet engine uses wire strain gages bonded onto the rotating components. The wire leads are then routed from the strain gages to the data acquisition system through a slip-ring assembly. Slip-ring systems are used extensively in the industry to collect data from rotating parts and have been the mainstay for many years. But assembling the equipment can be expensive and time consuming: from six to nine months and several million dollars (DeAnna 2000). Furthermore, several specific problems in contact slip-ring systems have been identified (Bates 1999), among which are inadequate capacity, size and reliability as well as the wear of the brush/ring contacts which makes the signal noisy and changes the electrical characteristic of the gages over time. Such performance degradation leads to high maintenance costs beyond the normal installation costs. In addition, the end of the rotating shaft has to be accessible to install the slip-rings; otherwise the slip-rings have to be installed in series between shafts (DeAnna 2000). All these disadvantages have motivated the development of non-contact systems to measure strain on compressor blades of gas-turbine engines, including telemetry systems.

### **1.1 Gas-turbine engine environment**

The gas-turbine environment is a very challenging one for RF transponders in that it is characterized by high temperatures, large “g” forces on the compressor blades, high ambient radio-frequency (RF) noise and highly-conductive metallic materials. The challenges of the gas-turbine environment can be appreciated from Figure 1.1.



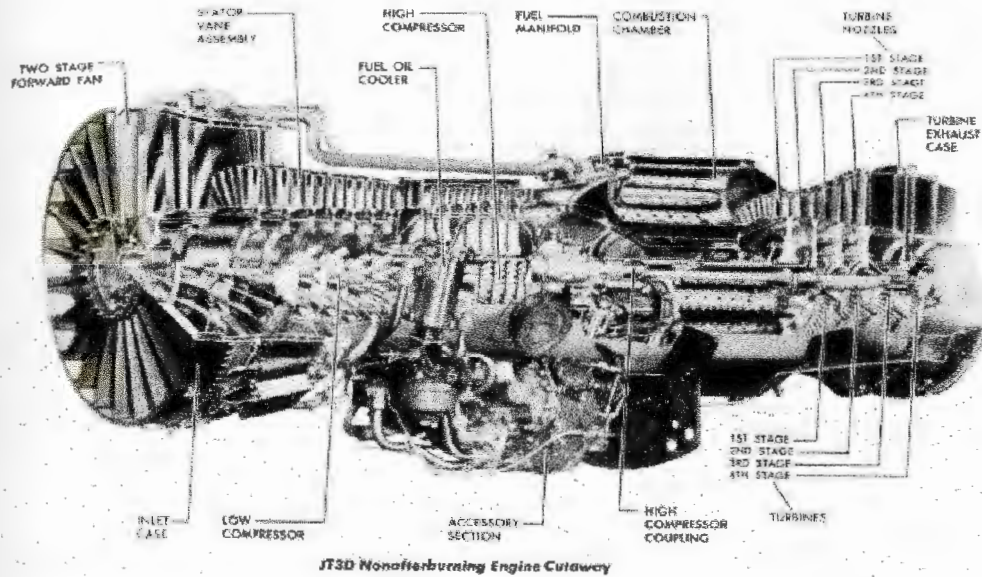


Figure 1.1 Typical components of a turbine engine (DeAnna 2000)

As shown in Figure 1.1, the turbine engine has several intricate gas flow paths which result in high gas velocities. The individual components that have to be instrumented include the fan blades, the inlet case, the low pressure compressor section, the high pressure compressor section, the burner section, the high and low pressure turbine sections, the exhaust duct and the exhaust duct nozzle (Pratt and Whitney 1982). Each section performs a specific function from compressing the air, mixing it with fuel, and burning the fuel-air mixture to accelerate the hot exhaust gas through the duct nozzle and generate thrust.

The low pressure compressor region typically operates at temperatures below 400 °F but the temperature increases in the engine as one move back until reaching the high pressure turbine section as shown in Figure 1.2 where the inlet temperatures can reach 1,600 °F for some large gas-turbine engines.

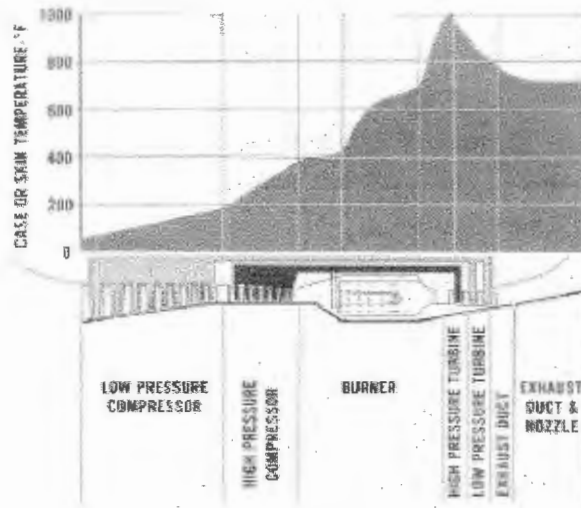


Figure 1.2 Temperature profile for gas-turbine engine (Pratt and Whitney 1982)

In addition to the high temperatures inside the engine, the blades can experience large “g” forces between 75,000 – 100,000 g (DeAnna 2000) for rotating components that operate at speeds approaching 12,000 rpm. Another important challenge inside the turbine engine is the propagation path of RF signals. Metallic objects in the propagation path may reflect RF signals. Depending on the frequency of operation and the thickness of the material of the turbine housing, RF propagation can be attenuated. The depth of penetration of an RF field is defined by

$$\delta = \frac{1}{\sqrt{\pi f \mu \sigma}} \quad (1)$$

where  $f$  is the frequency of the field,  $\sigma$  is the conductivity of the material and,  $\mu$  is the permeability of the conductor. It can be deduced from equation (1) that the skin depth at practical RF frequencies is much smaller than the thickness of the turbine engine casing. Therefore, it is not possible to transmit RF signals from inside the turbine

engine to an external signal processing system without line of sight access to the transponder circuit.

Furthermore, another constraint for the development of a wireless strain gage concept is the resolution and sensitivity of the sensor, since the strain experienced by the blades can vary from a few microstrain to 1400 microstrain. Finally, the dimensions of the transponder are important for stability of the turbine engine. The blade can only accommodate a few micro grams of additional mass of the transponder and its thickness should be well below the gas phase boundary layer thickness (~ 800 microns).

## **1.2 Research objective**

This thesis describes the design and fabrication of a prototype passive radio-frequency transponder that works as a wireless strain gage for gas-turbine engine applications. The research is focused on the development of a wireless strain gage to be used in the low pressure compressor section. Some studies (Gregory and Luo 2000) have reduced the temperature dependence of thin film strain gages by combining active strain elements with positive and negative temperature coefficients of resistance. The scope of this research is limited to the development of a few techniques that can be used in the wireless strain gage concept to self-compensate strain measurements to reduce temperature effects, i.e. apparent strain.

Additionally, the signal processing concept to be employed by the WSG system is beyond the scope of the research work. The signal processing limitations were taken into account only for the design of the RF transponder.



### 1.3 Wireless strain gage concept

The wireless strain gage (WSG) concept consists of a passive RF transponder that is printed or welded onto the blade within the low pressure compressor section of the engine. The distributed-element microwave circuit consists of a strain gage, i.e. resonator, capacitive/inductive/resistive element, and a small antenna. A transceiver unit is located outside the turbine engine housing (See Figure 1.3). The placement of the Tx/Rx antenna of the transceiver unit is chosen to be close to the instrumented blade without requiring major modifications to the casing.

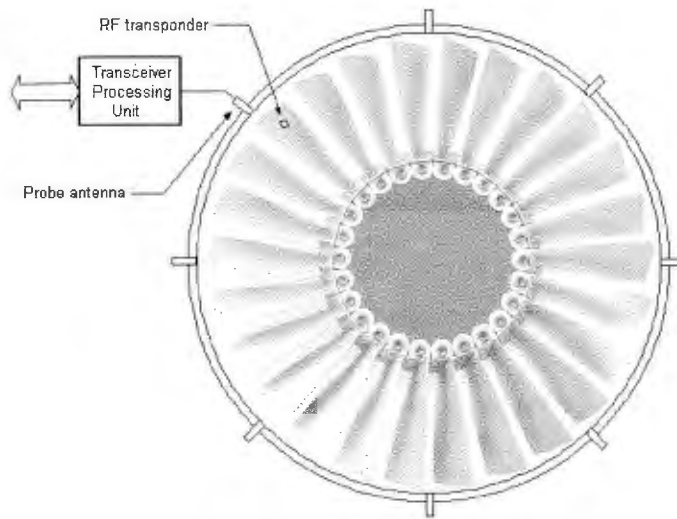


Figure 1.3 Location of RF transponder and transceiver

Initially, the passive transponder receives a short wide-band pulse of energy from the transceiver unit. Then, the transponder modulates the input signal and returns an impulse response signal as shown in Figure 1.4. The response of the transponder changes as a function of strain in the blades. For the resonant circuit, a change in the capacitance due to strain changes the resonant frequency of the circuit and thus, provides a correlation of the frequency shift with strain.

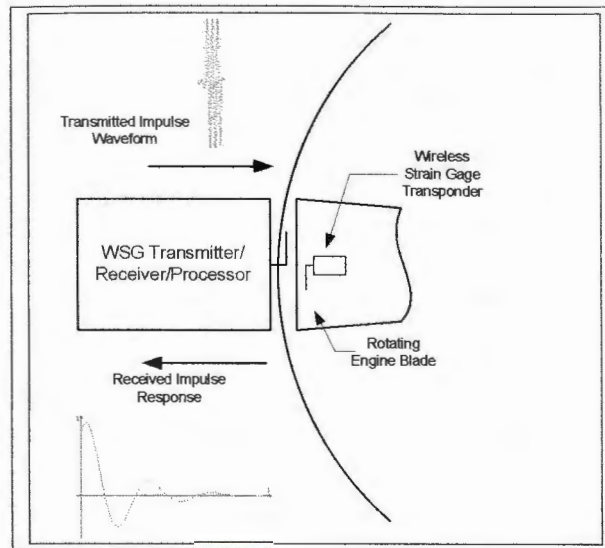


Figure 1.4 Wireless Strain Gage System

For signal processing purposes, the passive transponder can be modeled as lumped parameter RLC resonant circuit and that the strain on the blade induces a change in the capacitance of the resonant circuit. The two key parameters for the design of the RF transponder are the gage factor  $G$  and the quality factor  $Q$ .

The gage factor is the product of the quotient of change in resistance, capacitance, or frequency and strain  $\epsilon$ . This is:

$$G = \frac{\Delta\kappa}{\kappa} \cdot \frac{1}{\epsilon} \quad (2)$$

where  $\kappa$  can be resistance, capacitance or resonant frequency. The gage factor is a measure of the sensitivity of the sensor or a quantity change per unit applied strain.

The quality factor is the ratio of energy stored per cycle vs. the energy dissipated in a cycle. For a resonant circuit, the quality factor measures how sharp a resonance is. The quality factor is very important since it determines how fast a system loses stored energy.

## **CHAPTER 2 Literature review**

This chapter discusses the different technologies reviewed previous to the proposal for a feasible design of a wireless strain gage. The intention of this literature review was to determine if there was some information on strain sensors that could be utilized in the development of the wireless strain gage concept. Information collected during the literature review determined the direction of this research, by either ruling out some of the technologies and/or techniques, or contributing to a combination of different devices to achieve a feasible wireless strain gage for the compressor section of a gas turbine engine.

### **2.1 Surface Acoustic Wave (SAW) devices**

One of the technologies considered during the early stages of this research was the use of SAW devices for the wireless strain gage. Research on this family of devices as potential sensors started in the early 1970s. Some of the earliest studies on sensors using SAW devices were performed by Das (1978) and Wohltjen (1979), on sensors used to measure pressure and chemical properties of thin films respectively. SAW devices are also used as high performance signal processing elements such as filters and delay lines (Campbell 1989; Morgan 1991).

It was our purpose to investigate the use of SAW devices as wireless and passive sensors. Some of these contactless sensors measure temperature (Schmidth et al. 1994; Buf et al. 1994; Buff 2002), pressure (Pohl et al. 1997; Pohl and Seifert 1997) and torque (Wolff et al. 1996; Beckley et al. 2002; Kalinin 2004). The latter type of sensors has significance for our purposes since torque can be seen as a rotational force that causes stress on the surface of a given material. Some of the torque sensors based on wireless SAW devices are reviewed in the following sections.

### 2.1.1 Nature of surface acoustic waves

The term SAW is used to describe a non-dispersive surface wave that is bound to the surface of a solid medium. This wave, discovered in the nineteenth century by Lord Rayleigh, has two particle displacement components: a surface normal component and a surface parallel component. As mentioned by Auld (1990), the particle displacements occur “both in the direction of wave propagation and perpendicular to the direction of propagation while normal to the substrate surface”. Figure 2.1 shows the direction of propagation of a SAW.

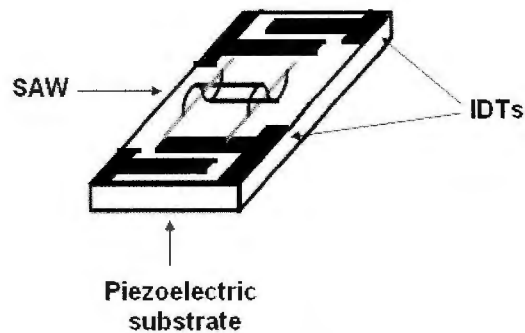


Figure 2.1 Direction of propagation of SAW

The particle displacements decay exponentially away from the surface. Most of the energy, i.e. more than 95%, is contained within a depth equal to one wavelength (Morgan 1973). The wave longitudinal velocity is determined by the substrate material and the cut of the crystal but it is typically in the range of 1500 to 4000  $\text{ms}^{-1}$ .

There are several types of acoustic waves (Hoummady et al. 1997) including shear horizontal surface acoustic wave (SH SAW), the shear horizontal acoustic plate mode (SH APM), the flexural plate wave (FPW) and the thickness shear mode (TSM) among others. However, these acoustic waves are beyond the scope of this research work and will not be considered further.

### **2.1.2 Principle of operation of SAW sensors**

A SAW sensor consists of piezoelectric substrate with thin-film interdigital transducers (IDTs) and reflectors deposited on the surface (Morgan 1991). An IDT is a structure of overlapping metal fingers fabricated on the substrate using photolithography.

The electrical signal in the IDT induces a SAW on surface of the substrate due to the piezoelectric effect. Likewise, a SAW generates an electric charge distribution at the IDT, creating an electric response. Therefore, the IDT converts electrical energy to mechanical energy in the form of a SAW, and conversely the process is partially reversible. Based on this effect, the principle of operation of a SAW sensor relies on the acoustic wave propagating time, amplitude and phase velocity between IDTs and reflectors change with the variation of physical variables such as temperature, stress and pressure.

### **2.1.3 Interdigital Transducer (IDT)**

An IDT consist of several interleaved electrodes made from thin metal lines or fingers deposited on a piezoelectric substrate as shown in Figure 2.2. As mentioned in the previous section, piezoelectricity in the substrate material is necessary for the operation of IDTs.

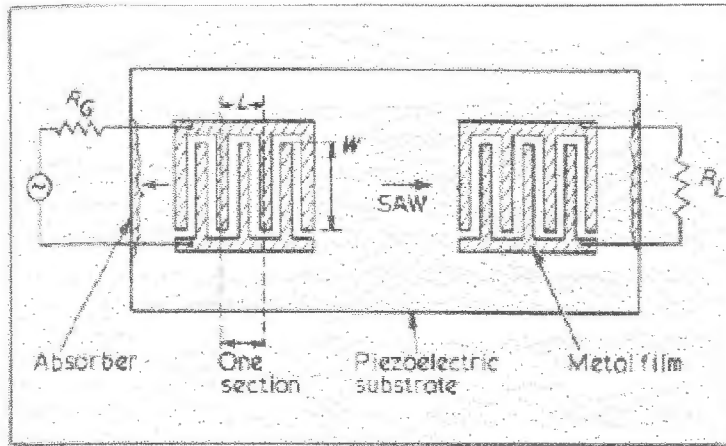


Figure 2.2 SAW delay line showing configuration of IDTs (Morgan 1973)

The line width of the interleaved electrodes is typically equal to the spacing between electrodes. Then, the periodicity of the IDT,  $L$ , is four times the linewidth of the electrodes as shown in Figure 2.2. As mentioned by Morgan (1973), when a voltage is applied to the IDT, a strain pattern of periodicity  $L$  is created. If the frequency is such that  $L$  is similar to the surface wave wavelength, the electrical energy is coupled into surface wave energy.

The frequency of operation or synchronous frequency of the IDT is given by:

$$f_o = \frac{v}{L} \quad (3)$$

where:

$f_o$  is the synchronous or resonant frequency

$v$  is the speed of the acoustic wave propagating on the substrate

$L$  is the periodicity of the IDT

The IDT has  $N$  sections, each section of length (periodicity)  $L$ , so the total number of interleaved fingers is  $2N + 1$ . Another important value is the aperture of the IDT,



$W$ , which is related to the total capacity of the transducer as discussed later in this section.

IDTs can be modeled by an approximate simplified theory (Smith et al. 1969). In this model, the IDT is considered an array of sources, each one being related to a piezoelectric plate transducer for launching bulk waves. Each bulk wave transducer is represented by an equivalent circuit in which a piezoelectric coupling constant has a value suitable for surface waves (Morgan 1973). Some of the necessary parameters to design an IDT for SAW sensors are obtained from this model. These parameters are: the static capacity per section ( $C_s$ ), the piezoelectric coupling constant ( $k^2$ ), the resonant frequency ( $f_a$ ) and the number of sections ( $N$ ).

It must be noted that the piezoelectric coupling constant is an indicator of the effectiveness with which a piezoelectric material converts electrical energy into mechanical energy. So, when choosing a substrate material, the piezoelectric coupling constant should be as large as possible. Additionally, the static capacity per section is proportional to the aperture  $W$  and is independent of the periodicity  $L$  (Farnell et al. 1970).

#### **2.1.4 Wireless SAW devices**

Wireless interrogation of a SAW sensor is achieved by connecting an antenna to the IDT. The antenna receives a burst of energy, i.e. a high frequency electromagnetic wave, emitted from the interrogation unit. The IDT converts the electrical energy to mechanical energy as mentioned before, by the reverse piezoelectric effect. Figure 2.3 shows a schematic of a wireless SAW device.

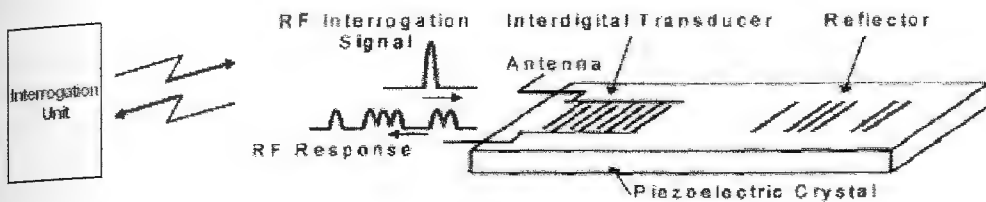


Figure 2.3 Schematic layout of a wireless SAW device (Reindl et al. 1998)

There are four basic designs of wireless SAW devices (Atashbar et al. 2003): delay line, reflective delay line, one-port resonator and two-port resonator as shown in Figure 2.4

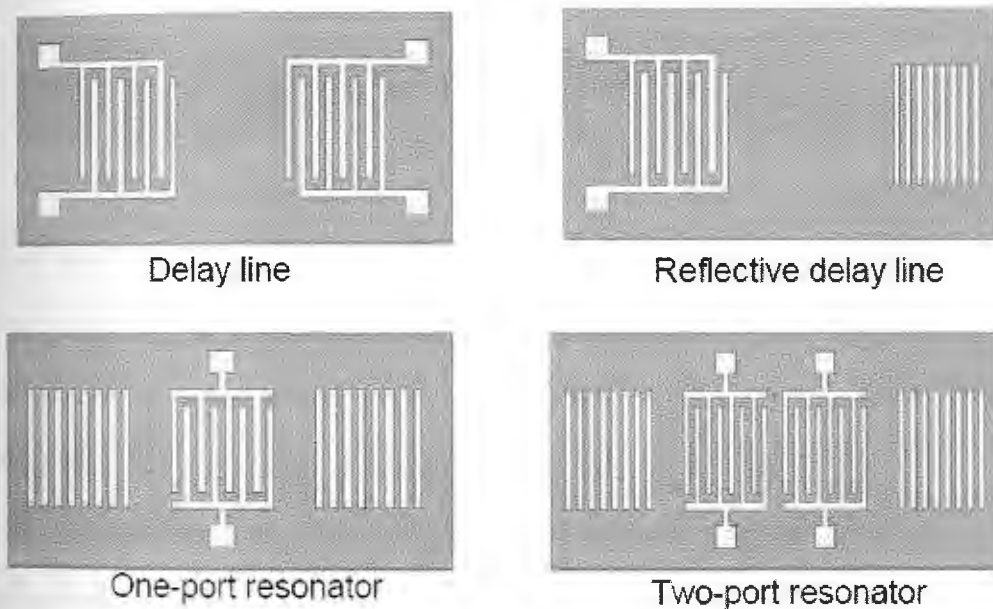


Figure 2.4 SAW device configurations

A delay line consists of two IDTs. In this configuration, the acoustic wave launched by the electromagnetic signal propagates from the input IDT or port through the surface of the piezoelectric to the output port where the mechanical energy is converted back to an electrical signal. A slight variation of a delay line is a reflective



delay line which instead of two ports it consists of only one IDT and a set of reflectors placed at a certain distance. The effect is that the SAW propagating from the input port is partially reflected back by the reflectors, generating echo pulses that arrive back to the IDT with a certain delay. When a strain  $\varepsilon$  is applied in the x-direction along the length of the substrate of a SAW delay line, the change of geometry changes the propagation velocity (Grossman et al. 1996). The result is a change in the phase difference given by:

$$\frac{\Delta\varphi_{ik}}{\varphi_{ik}} = \frac{\Delta l_{ik}}{l_{ik}} - \frac{\Delta v}{v} \approx 1.24\varepsilon \quad (4)$$

where:

$l$  is the distance between reflectors

$v$  is the wave propagation velocity

This type of saw devices has been used as ID-tags for remote sensing identification applications (Nysen et al. 1986; Bulst and Ruppel 1994) and more specific information on the design of reflective delay lines can be found in Reindl et al. (1998) and Pohl (2000).

As opposed to SAW delay lines, SAW resonators have the IDT(s) positioned in the middle of the cavity with reflectors on both sides as shown in Figure 2.4. A one-port resonator has only one IDT which is connected electrically whereas a two-port resonator has two IDTs. The induced SAW has a resonant frequency  $f_0$  given in Eq. 2. The response of a SAW resonator is a damped harmonic oscillation has shown in Figure 2.5.

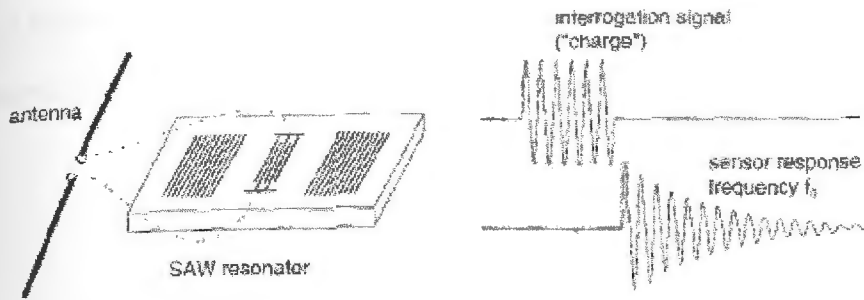


Figure 2.5. Wirelessly interrogable SAW resonator (Pohl 1998)

When the RF interrogation signal excites the resonator, the received burst of energy is stored in the cavities of the resonator. After the RF signal is switched off, the resonator uses part of the stored energy to generate a decaying pulse response.

When a strain  $\epsilon$  is induced in the x-direction of the substrate of a SAW resonator, the effect is a change in the resonant frequency given by:

$$\frac{\Delta f_o}{f_o} = -\frac{\Delta L}{L} + \frac{\Delta v}{v} \approx 1.24\epsilon \quad (5)$$

where:

$L$  is the periodicity of the IDT

$v$  is the wave propagation velocity

This type of SAW devices have been used for remote railroad car identification and torque measurements on rotating transmission shafts (Grossmann et al. 1996; Beckley et al. 2002; Kalinin et al. 2004), as well as other applications (Reindl et al. 1998; Pohl et al. 1998, 2000; Atashbar et al. 2003).

Figure 2.6 shows a visual comparison between the response of a SAW delay line and the response of a resonator when these devices are used for wireless measurements.

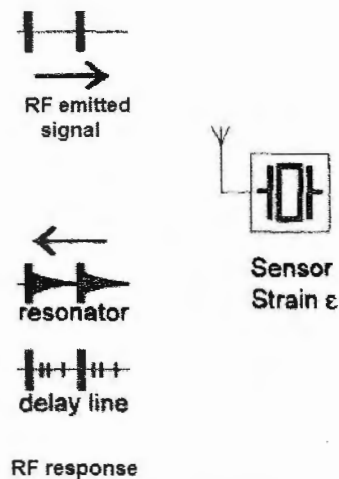


Figure 2.6 Comparison of RF responses of SAW delay lines and resonators

### 2.1.5 Torque SAW sensors

SAW devices have been used to measure torque on rotating shafts. SAW resonators are more popular than SAW delay lines when used in passive sensors since resonators have less insertion loss as opposed to delay lines (Kalinin 2004). However, both SAW reflective delay lines (Wolff et al. 1996) and SAW resonators (Grossmann et al. 1996; Beckley et al. 2002) have been used as remote sensors during the past 18 years to measure torque for stress analysis and process control.

Strain on the rotating shaft is proportional to the applied torque at  $\pm 45^\circ$  angles with respect to the axis of rotation. Typically, two SAW resonators are applied to the surface of the rotating shaft for differential measurement. Each SAW resonator has its own antenna wound around the shaft. The resonant frequencies of each resonator change in opposite direction when torque is applied. So by measuring the difference between the two resonant frequencies, the torque applied can be measured.

Additionally, temperature compensation can be achieved with this setup since a temperature change will affect both SAW sensors but the absolute difference in resonant frequency will remain the same. Figure 2.7 shows a typical setup for wireless torque measurements using SAW resonators.

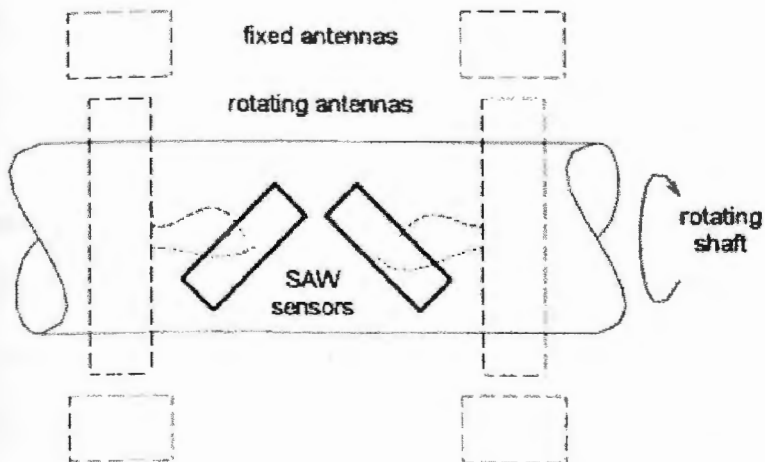


Figure 2.7 Typical setup for wireless torque SAW sensors (Pohl and Seifert 1997)

Kalinin et al. (2004) developed a commercial contactless torque sensor based on 4 one-port SAW resonators using quartz as a piezoelectric substrate. The contactless system operates in the 430 to 430 MHz range with a sensitivity of 2.8 kHz/ $\mu$ strain or a GF of approximately 6.5.

The authors did not elaborate in the specifics of the design of this sensor, however, to estimate the basic parameters, the frequency of operation has to be taken into account as well as the substrate material to determine longitudinal speed of the acoustic wave and the periodicity of the IDT. Using a SAW resonator operating in the 430 MHz range using a Y+34° rotated cut of quartz as the propagation surface and assuming a 6000 m/s longitudinal speed for this type of cut of quartz (Kushibiki et al. 2002), the periodicity of the IDT is approximately 15  $\mu$ m by equation (3). This

implies that the spacing between the IDT electrodes and the line width of the electrodes themselves is around one fourth of the periodicity or about 3.8  $\mu\text{m}$ .

Based on this literature review on SAW resonators as torque sensors, it was decided to explore this type of devices for the WSG concept. As it is shown in the next section, a number of issues arose that were addressed in the design of a SAW resonator for gas-turbine applications.

### 2.1.6 Proposed SAW design for the WSG concept and shortcomings

To verify the feasibility of SAW devices as a wireless strain gage, an initial SAW generator design was proposed. First, a suitable substrate was needed for piezoelectricity. The substrate of choice was a thermoplastic fluoropolymer (PVDF or Polyvinylidene fluoride). The following tables (Precision 2007) show typical values for some properties of poled PVDF films. Highlighted are the properties that are most important for SAW devices.

Table 2.1 Physical properties of PVDF

Description	Semi-crystalline polymer consisting of crystallites embedded within amorphous polymer chains	
Density	$\rho$	1780 kg m <sup>-3</sup>
Melting Temperature	$T_m$	175-180°C
Glass Transition Temperature	$T_g$	-42 °C
Curie Temperature	$T_c$	None observed but extrapolates to 205°C
Young's Modulus	E	8.3 GPa
Bulk Modulus	K	4.3 GPa
Shear Modulus	U	3.5 GPa
Poisson's Ratio	$\nu$	0.18



Table 2.2 Piezoelectric and acoustic properties of PVDF

Longitudinal Velocity	$c_L$	2250 m/s
Shear Velocity	$c_s$	1410 m/s
Piezo Strain Constant (shear mode direction 1)	$d_{31}$	Uniaxial Film: 22 pC/N Bi-axial Film: 6 pC/N
Piezo Strain Constant (shear mode direction 2)	$d_{32}$	Uniaxial Film: 3 pC/N Bi-axial Film: 5 pC/N
Piezo Strain Constant (thickness mode)	$d_{33}$	-30 pC/N
Piezo Stress Constant (shear mode direction 1)	$g_{31}$	Uniaxial Film: 0.216 Vm/N Bi-axial Film:
Piezo Stress Constant (shear mode direction 2)	$g_{32}$	Uniaxial Film: Bi-axial Film:
Piezo Stress Constant (thickness mode)	$g_{33}$	-0.33 Vm/N
Electromechanical Coupling Factor	$k_c$	14%

Table 2.3 Electrical properties of PVDF

Coercive Field Strength	$E_c$	50-80 MV/m
Breakdown Field Strength	$E_B$	200 MV/m
Relative Dielectric Constant	$\epsilon_r$	10-12

There is some variation in the material properties, depending on the manufacturer, but some of the advantages and disadvantages of this material as a substrate can be directly assessed.

Even though the acoustic waves travel at a slower speed (longitudinal speed = 2250 m/s) compared to other substrates which are not suitable for our purposes such as quartz or PZT, the piezoelectric coupling factor of PVDF ( $k_c = 14\%$ ) is much higher relative to other substrates for SAW devices as lithium niobate or aluminum oxide which are not above 5%.

The next most important component to be designed was the IDT since this will determine the resonant frequency of the SAW resonator. One of the design constraints for the development of a WSG was the operational frequency in the GHz range. The problem with SAW devices for our purposes was that the line width and spacing of the IDT electrodes are beyond the capabilities of most labs, especially if compressor blades are to be patterned.

Specifically, using equation (3) and solving for the periodicity  $L$ , and using the longitudinal speed for PVDF (2250 m/s) shown in Table 2.2, one can calculate the minimum line width and spacing of the IDT electrodes. If the frequency of operation needed needs to be at least 1 GHz, then the periodicity of the IDT is about 2.25  $\mu\text{m}$ , or approximately 0.5  $\mu\text{m}$  for line width and spaces. Any feature size below 1  $\mu\text{m}$  becomes very difficult to fabricate on the convoluted surface of compressor blades. So, if 25  $\mu\text{m}$  is the minimum feature size achievable, then the frequency of operation of the wireless strain gage using PVDF as substrate is around 22.5 MHz, which is well below the microwave range required. For a more details on the design parameters of the proposed SAW design, see Appendix A.

Because of the fabrication limitations, the idea of using SAW devices to develop a wireless strain gage was eliminated. Although, no additional research on this type of devices was pursued, this initial approach helped sort out to understand the fabrication constraints. Therefore, a different approach using thin film and thick film deposited sensors was explored to develop a wireless strain gage. Furthermore, two other approaches using “free standing” structures are explored and introduced in Chapter 4.

### **CHAPTER 3 Thin/thick film designs and simulations**

This chapter discusses the different designs used for both the thin film and thick film approaches and it addresses the importance of the simulations for the next stage of the research: the fabrication process. The simulations were used to make some important decisions regarding the type of materials and design parameters such as: dielectric material, the thickness of the metal layer, the line width and spacing of electrodes of the transducer and its general dimensions. The software tool used for simulations is called Sonnet Lite, which is an electromagnetic high frequency software that allows the simulation of many of the planar structures used in this research. The simulations were of great importance since they allowed us to pick the best combination of parameters, not spending extra time fabricating prototypes that would not comply with the requirements and constraints of the project. First, the design parameters of thin-film approach is presented, including multiple simulations, followed by the thick- film designs.

#### **3.1 Thin film approach: parallel capacitor vs interdigital capacitor**

The first approach explored was a thin film capacitor using a couple of interdigital electrodes, similar to the IDTs discussed in Chapter 2. The idea was to create a stacked capacitor by depositing a thin metal layer, followed by a dielectric material and then a second metal layer. The reason why these thin film metals have the shape of an IDT is because simulations showed a bigger change in capacitance when using interdigital shaped electrodes as compared to a typical capacitor made out of parallel plates. Figure 3.1 shows the layout of a parallel plate capacitor and capacitor using interdigital electrodes



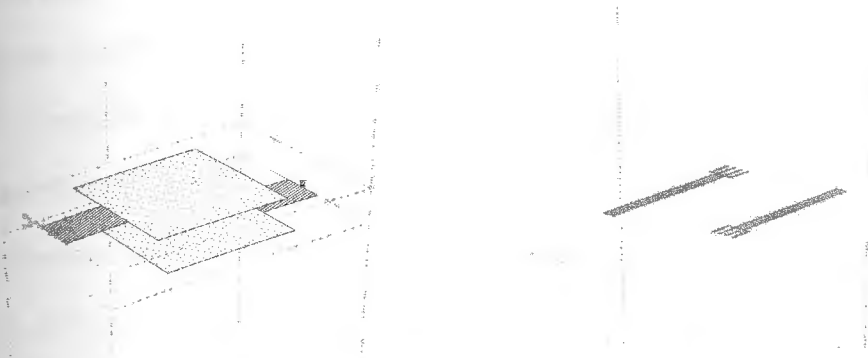


Figure 3.1 Layout of parallel capacitor (left) and interdigital capacitor (right)

For comparison purposes, the same strain was applied to both planar structures. The specifications of these two layouts are as follows: for the parallel capacitor, the overlapping area of the parallel plates is about 2 mm x 2mm and for the interdigital capacitor the line width of the interdigital fingers is about 150  $\mu\text{m}$  by 2 mm long. For both designs, the dielectric material used is called polyimide with a thickness of 8  $\mu\text{m}$  and a dielectric constant of 3.5. It must be noted that the different dimensions just mentioned are not at the same scale in Figure 3.1.

The simulations showed that the parallel capacitor had a base capacitance of about 17.6 pF and when the structure was strained by the value increased to 20.3 pF. Therefore using equation (2) and a strain value of 20,000  $\mu\text{strain}$ , the gage factor is about 7.6. The reason why such a large amount of strain was induced was that the version of the software tool Sonnet Lite was a free, limited one and it would not allow us to input smaller values of strain. Still, it was sufficient for the decision-making process since the same strain was applied to the interdigital capacitor. The simulation results for the interdigital capacitor design showed a base capacitance of about 4.9 pF and when the planar structure was strained the capacitance value increased to 6.5 pF,

for a gage factor of about 14. Therefore, the interdigital capacitor was chosen over the regular parallel plate capacitor design because of its larger gage factor.

During the design of the interdigital capacitor, several parameters were varied to determine the best gage factor achievable by this type of planar structure. The parameters varied were the line width and spacing of the interdigital electrodes. Table 3.1 shows the two sets of parameters used in Sonnet to determine the best combination of line width and spacing.

Table 3.1 Sets of parameters for interdigital capacitor

	Line width ( $\mu\text{m}$ )	Spacing ( $\mu\text{m}$ )	Ratio line width/spacing
<b>Design 1</b>	150	550	0.27
<b>Design 2</b>	200	600	0.33

The results of the simulations showed a slightly better gage factor for design 1 and are shown in Table 3.2. Additional plots of the simulations can be found in Appendix B.

Table 3.2 Comparison of capacitance values and gage factors

	Base capacitance (pF)	Strained capacitance (pF)	$\Delta C$ (pF)	$\mu\text{Strain}$	Gage factor
<b>Design 1</b>	4.921	6.491	1.57	22,222	14.35
<b>Design 2</b>	6.496	8.066	1.57	19,230	12.56

From Table 3.2 it can be seen that the change in capacitance is the same and the reason for this is that since the designs have different dimensions, when strain is applied the increase in the overlapping area of the interdigital fingers is the same, resulting in the same  $\Delta C$ . If the applied strain is the same in both designs, then the  $\Delta C$  will be different. In the end, the definition of the gage factor takes into account the change in capacitance with respect to the base capacitance and the strain. An additional interdigital capacitor design with a smaller line width and spacing ratio was simulated, yielding even a higher gage factor of about 15. As a result, it can be determined that the smaller the line width/spacing ratio the larger the gage factor. The limitation is the minimum feature size. As the line width and spacing between electrodes decreases, the fabrication process becomes more complicated as described in Chapter 5. Therefore, it was decided to use the parameters of design 1.

### **3.2 Thin film interdigital capacitor: design parameters and simulations**

In order to save time and resources, it was important to run some simulations before fabricating a prototype with the design parameters to be described in Table 3.3. During these simulations, not only the expected base capacitance value was estimated but also, the strained capacitance value (See Table 3.2 and Appendix B). Interestingly enough, the simulations showed in fact that the interdigital capacitor itself acted as a resonant structure. Unfortunately, its resonant frequency was outside the 1 – 2 GHz frequency of operation range desired. Therefore, an antenna element was added to the structure to try to shift that resonant frequency.

First of all, the parameters used for both the simulation and fabrication of a thin film interdigital capacitor are show in Table 3.3. For a visual representation of these design parameters, see Appendix B.

Table 3.3 Design parameters of thin-film capacitor

<b>Metal type</b>	Copper
<b>Metal thickness</b>	1 $\mu\text{m}$
<b>Dielectric material</b>	Polyimide
<b>Dielectric constant</b>	3.5
<b>Dielectric thickness</b>	8 $\mu\text{m}$
<b>Dielectric loss tan</b>	0.003
<b>Electrodes line width</b>	150 $\mu\text{m}$
<b>Electrodes spacing</b>	550 $\mu\text{m}$
<b>Number of fingers</b>	4
<b>Antenna length</b>	6 – 7 mm
<b>Antenna width</b>	1 mm

Somet Lite calculates the capacitance by using the admittance and impedance formulas. The admittance formula can be use when the resistance of the capacitor is negligible. These formulas are given by:

$$Y_c = Z^{-1} \quad (6)$$

$$Z_c = \frac{1}{j2\pi fC} \quad (7)$$

where  $Y_c$  is the admittance of the circuit

$Z$  is the impedance of the circuit

$f$  is the frequency

$C$  is the capacitance of the interdigital transducer

Combining equations (5) and (6), the capacitance can be written in terms of the admittance. This is:

$$C = \frac{1}{j\left(\frac{1}{Y_c}\right)2\pi f} \quad (8)$$

Therefore, the capacitance plot given by Sonnet Lite is actually a plot of the admittance of the interdigital capacitor. This is shown in Figure 3.2.

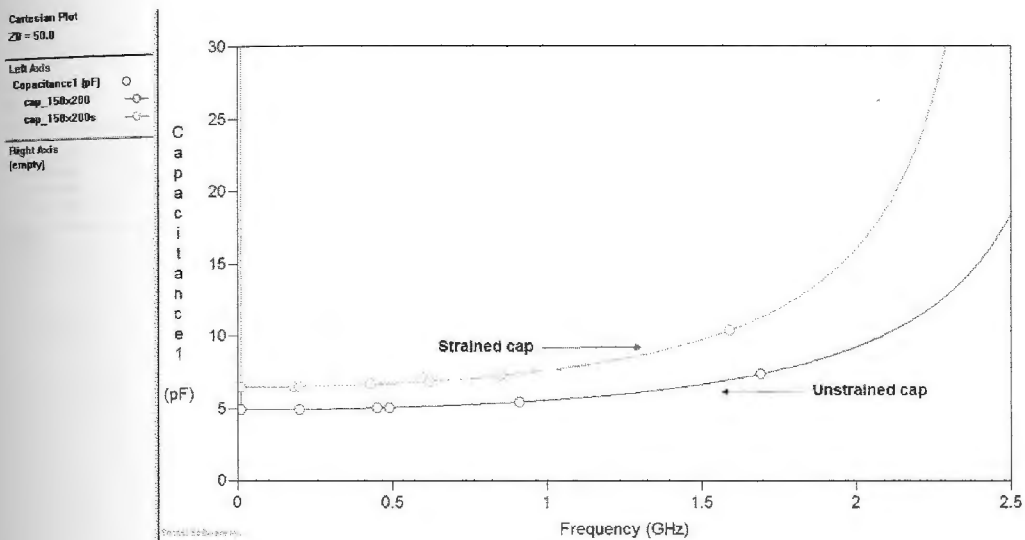


Figure 3.2 Capacitance plot given by Sonnet Lite

As it was expected, it can be seen in Figure 3.2 that the capacitance value increases as the frequency increases, and the only reason for this is because of how the EM simulator calculates the capacitance. For our purposes, the estimated capacitance value was taken when  $f$  is equal to 1, and these values are shown in Table 3.2 for design 1. Additionally, it must be noted that the plot shows a spike when  $f$  is

close to zero. This is because the frequency is in the numerator in equation (8), which makes the estimated capacitor value go to infinite when  $f$  is very small.

Furthermore, when the simulation was swept from DC to 3 GHz, it was found the interdigital capacitor behaved like a resonant circuit. This is that a resonance condition was observed at a frequency when the admittance was at a maximum point. These can be seen by plotting either the real part of the admittance, called conductance ( $G$ ), or the imaginary part, called susceptance ( $B$ ). Figure 3.3 and 3.4 show the resonance condition.

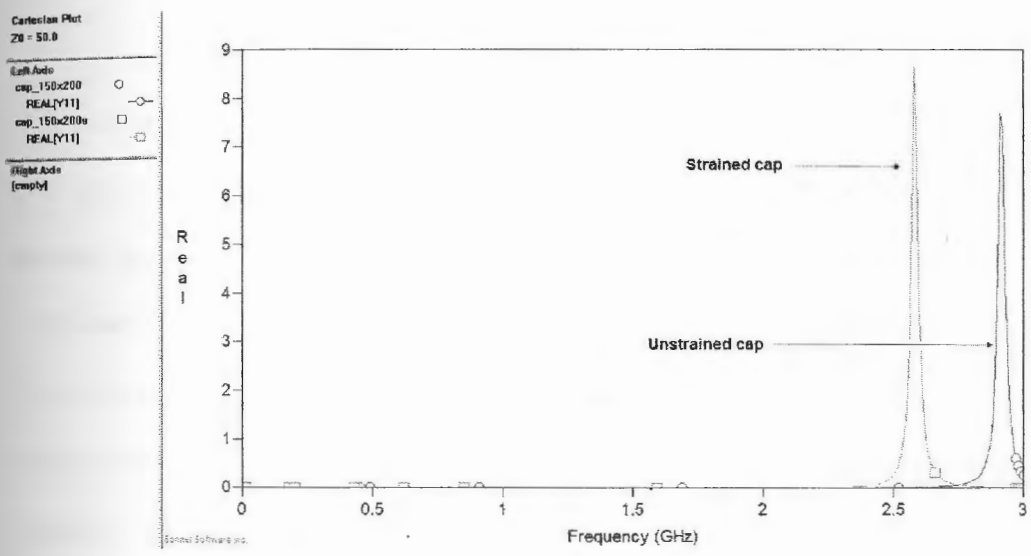


Figure 3.3 Conductance plot of interdigital capacitor



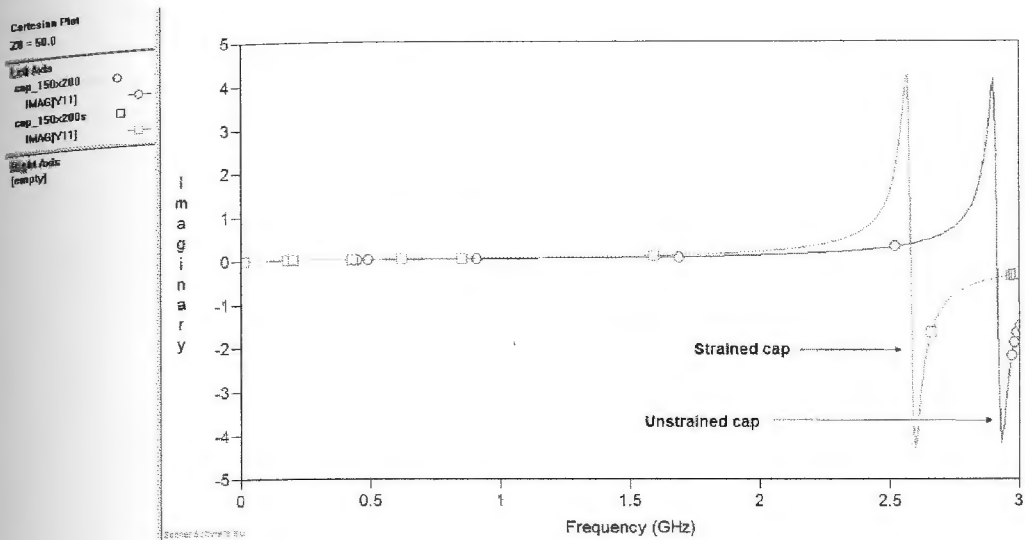


Figure 3.4 Susceptance plot of interdigital capacitor

From the previous figures, the resonant condition is achieved at a frequency of 2.91 GHz when the interdigital capacitor is not under stress. This compares to a resonant frequency of 2.58 GHz when the planar structure is strained. Using equation (2) to calculate the gage factor in terms of resonant frequency, it yields a value of 5.1. This value compares to gage factor of around 14 when the only the capacitance value is taken into account. Furthermore, the resonant frequency of the strain and unstrained conditions are outside the desire frequency of operation. Therefore, an antenna element was added to the top layer of the interdigital capacitor to try to shift the resonant frequency.

Two different antenna lengths were used for simulations: 6 mm and 7 mm. For fabrication reasons that are mentioned in the fabrication chapter of this thesis, the length of the antenna could not be any longer or smaller. The results of the simulations using these two different antenna lengths are shown in Figure 3.5.

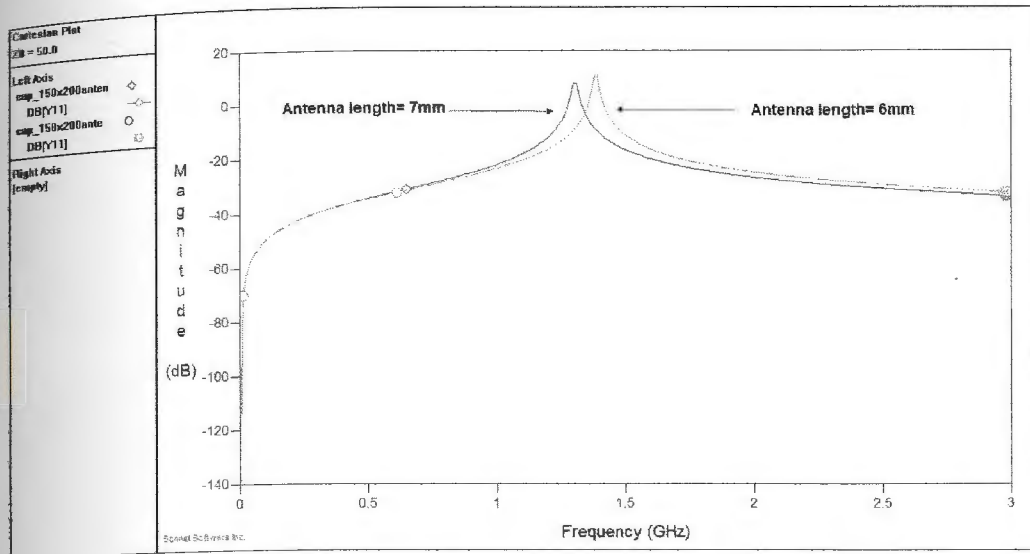


Figure 3.5 Resonance condition for different antenna lengths

It can be seen in Figure 3.5 that the resonant frequency of the interdigital capacitor is 1.39 GHz and 1.31 GHz, for an antenna length of 6 mm and 7 mm respectively. This frequency range is now within the 1 – 2 GHz range of operation needed.

Finally, a couple more simulations were executed to determine the expected gage factor when using an antenna length of 6 mm and 7 mm. Previously, the gage factor in terms of frequency without an antenna element and at an operating frequency above 2 GHz was about 5.1. Figure 3.6 shows the shift in the resonant condition when the interdigital capacitor including a 6 mm antenna was under about 20,000  $\mu$ strain.



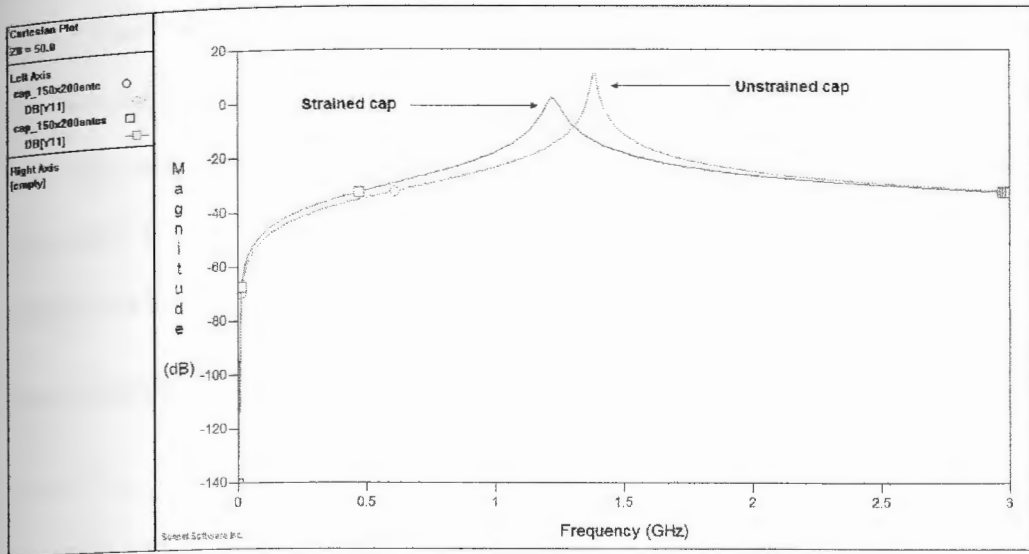


Figure 3.6 Shift in resonant frequency when using a 6-mm antenna

The resonant frequency of the interdigital capacitor is 1.38 GHz and 1.24 GHz when the structure is at normal condition and when stress is applied respectively. This yields a gage factor of 4.56 which is very similar to the 5.1 gage factor obtained when the antenna element is not included. Therefore, the antenna is only shifting the resonant frequency to the desired range while keeping a similar gage factor in terms of frequency. A similar gage factor was also obtained when the antenna length was increased to 7 mm.

The next step was to fabricate the thin-film interdigital capacitor using the design parameters previously mentioned following the fabrication steps described in Chapter 5. Next section of this chapter explains a different approach using a thick-film capacitor design.

### 3.3 Thick film interdigital capacitor: design parameters and simulations

One of the issues never addressed in the previous design using thin films was the skin effect and its relation to the thickness of the metal film or skin depth. First, the skin effect is a phenomenon where the current density decreases exponential with depth from the surface of a conductor. Furthermore, the skin depth ( $\delta$ ) is defined as the depth below the surface of a conductor at which the current density reaches  $\frac{1}{e}$  of the current on the surface ( $J_s$ ). The skin depth is a variable that measures how far electrical conduction occurs in a conductor and as it is shown in equation (1), it depends on the frequency of operation. At DC, the skin depth can be neglected since the entire cross-section of the conductor is used for propagation. However, when it comes to higher frequencies of operation, the skin depth plays an important role to reduce losses. The higher the frequency of operation the smaller the skin depth is. For our purposes, since our target frequency is between 1 and 2 GHz, the thickness of the conductors can considerable decreased, as it was done in the thin-film approach, using a 1- $\mu\text{m}$  metal film.

It is important to note that the metal surface nearest to the dielectric material is the surface that carries the RF current. Therefore, RF currents are highest in the lower and upper surface of the top and bottom interdigitated electrode. Regardless of this, one of the issues of the thin-film approach was the thickness of the metal. Figure 3.7 shows a plot of the skin depths as function of frequency using copper as a conductor.

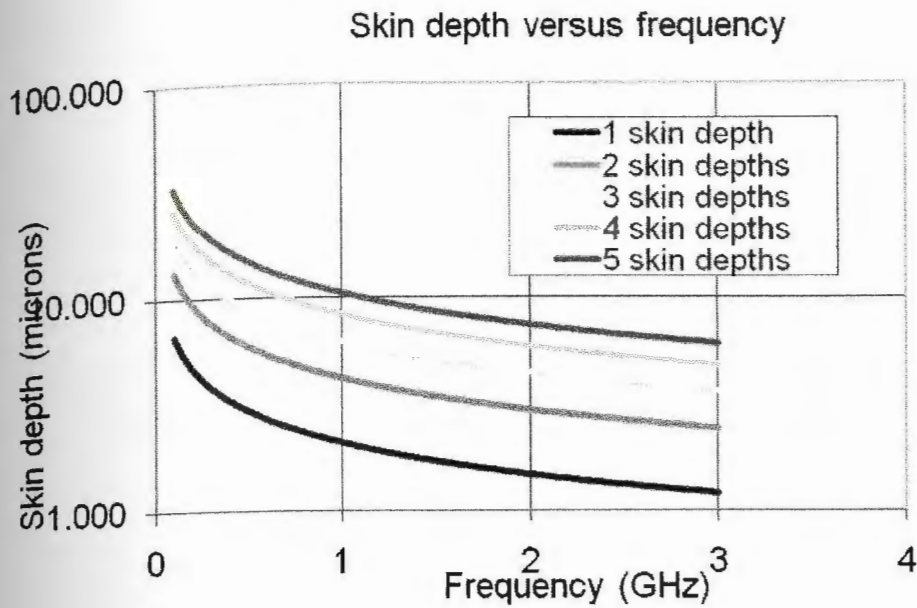


Figure 3.7 Skin depth vs Frequency

For a frequency of operation between 1 and 2 GHz, the minimum skin depth is between 1 and 2  $\mu\text{m}$ . Therefore, the thickness of the film deposited in the previous design, falls short from the minimum skin depth to avoid large RF losses. Additionally, it is the rule of thumb to have at least 5 skin depths of conductor so most of the energy is contained and losses are minimized. As seen in Figure 3.7, the 5-skin depth mark for the 1 to 2 GHz range shows a minimum of 10  $\mu\text{m}$  of film thickness. Based on this analysis, modifications to the thin film approach were made and a thick film design was developed.

The thick film interdigital capacitor consisted of two 4-finger interdigitated copper electrodes with a dielectric in between, just like the previous thin film design. Similarly, the line width and spaces between the electrode fingers remained the same since the main issue to be addressed with the new approach was to reduce the skin effect. Table 3.4 summarizes the design parameters of the thick film approach.

Table 3.4 Design parameters of thick film capacitor

<b>Metal type</b>	Copper
<b>Metal thickness</b>	10 $\mu\text{m}$
<b>Dielectric material</b>	Polyimide
<b>Dielectric constant</b>	3.5
<b>Dielectric thickness</b>	60 $\mu\text{m}$
<b>Dielectric loss tan</b>	0.003
<b>Electrodes line width</b>	150 $\mu\text{m}$
<b>Electrodes spacing</b>	550 $\mu\text{m}$
<b>Number of fingers</b>	4
<b>Antenna length</b>	10 mm
<b>Antenna width</b>	1 mm

Basically, two main changes were made to the thin film approach; first, the metal thickness was increased to 10  $\mu\text{m}$  to stay within the 5-skin depth mark given for a 1 to 2 GHz operation. Additionally, the thickness of the dielectric layer had to be increased to more than 10  $\mu\text{m}$  since this layer is not only deposited on the area where the fingers overlap to form the capacitor but also under the antenna (See Figure 3.8). This is that, the dielectric layer has to come down from the bottom metal layer to the ceramic strain beam, creating a small step on the surface where the top metal layer is deposited. If the dielectric is not at least as thick as the metal film, the step created is too large, so the deposition of the top electrode becomes more difficult and the joint between the antenna and the interdigital electrodes are at risk. Note that Figure 3.8 does not show the step created when the dielectric layer is deposited.

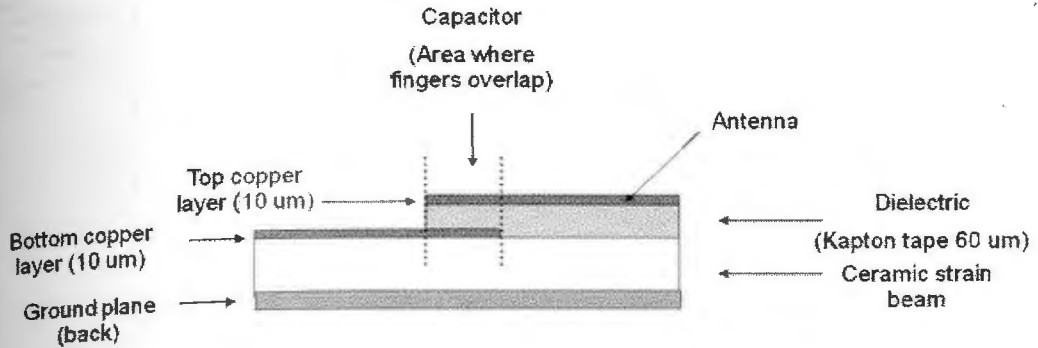


Figure 3.8 Cross-section area of thick-film capacitor

These changes in the design changed not only the expected base capacitance and the resonant frequency of the sensor; the fabrication procedure had to be also changed since the film deposition time becomes too lengthy when the thickness of the metal increases. These issues and other observations are addressed in Chapter 5.

Sonnet Lite was also used to simulate the response of the new design. First, the expected base capacitance and the change in capacitance when strain was applied were assessed. From basic theory of parallel capacitor plates, a decrease in the base capacitance was expected. Since the distance between the interdigital electrodes increases by almost a factor of 8 (from 10  $\mu\text{m}$  in the thin film design to 60  $\mu\text{m}$  in this approach), it was expected to see a decrease in the base capacitance of similar magnitude. As mentioned before, the EM simulation tool calculates the capacitance base in the admittance, using equation (8). Figure 3.9 shows the plot given by Sonnet Lite when calculating the capacitance.

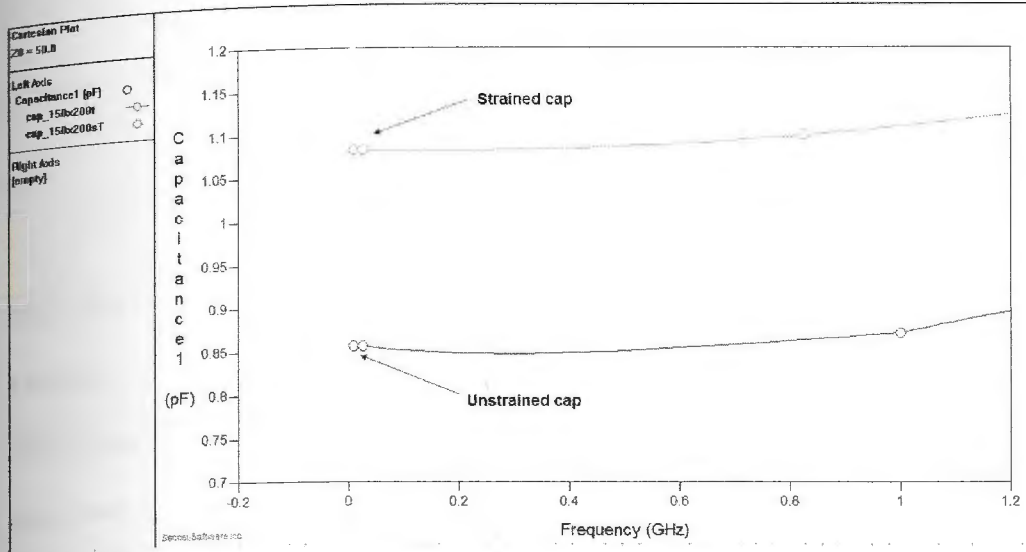


Figure 3.9 Capacitance plot for thick-film capacitor given by Sonnet Lite

As shown in the previous figure, the base capacitance (unstrained capacitance) is about 0.857 pF, which is 1/6 of the base capacitance value of the thin-film approach, i.e. 4.921 pF. Although, the new unstrained capacitance value is not eight times smaller, this new values is close to what was expected. When strain was induced on the thick-film capacitor, the capacitance increased to 1.083 pF. Therefore, using equation 2 and a strain value of about 20,000  $\mu$ strain, a gage factor of 11.87 was estimated. Table 3.5 shows a comparison between the capacitance and gage factor values of the thin-film capacitor and the new thick-film approach.



Table 3.5 Comparison of capacitance values and gage factors

	<b>Base capacitance (pF)</b>	<b>Strained capacitance (pF)</b>	<b>ΔC (pF)</b>	<b>μStrain</b>	<b>Gage factor</b>
<b>Thin-film capacitor</b>	4.921	6.491	1.57	22,222	14.35
<b>Thick-film capacitor</b>	0.857	1.083	.226	22,222	11.87

Based on the simulation results shown in Table 3.5, the gage factor is smaller in the thick-film approach than the thin-film one. One hypothesis for this behavior is that since the dielectric layer is thicker, the strain applied to the bottom electrode of the capacitor does not transfer efficiently to the top electrode, undermining the change in capacitance and therefore, the gage factor.

The thicker dielectric layer not only decreases the base capacitance value but also changes the resonant frequency of the circuit. A smaller capacitance value results in an increase in the resonant frequency. In the thin-film capacitor, a 6 – 7 mm long antenna was needed to shift the resonant frequency from the upper 2 GHz range to the 1.30 – 1.40 GHz range. For the thick-film capacitor, it was expected that the resonant frequency would be increased by a factor of  $\sqrt{6}$  since the base capacitance decrease  $1/6$  and the resonant frequency formula is  $f = 1/\sqrt{LC}$ . Therefore, the expected resonant frequency of thick-film capacitor was about 7.1 GHz. Simulations corroborated this estimation and it is shown in Figure 3.10.

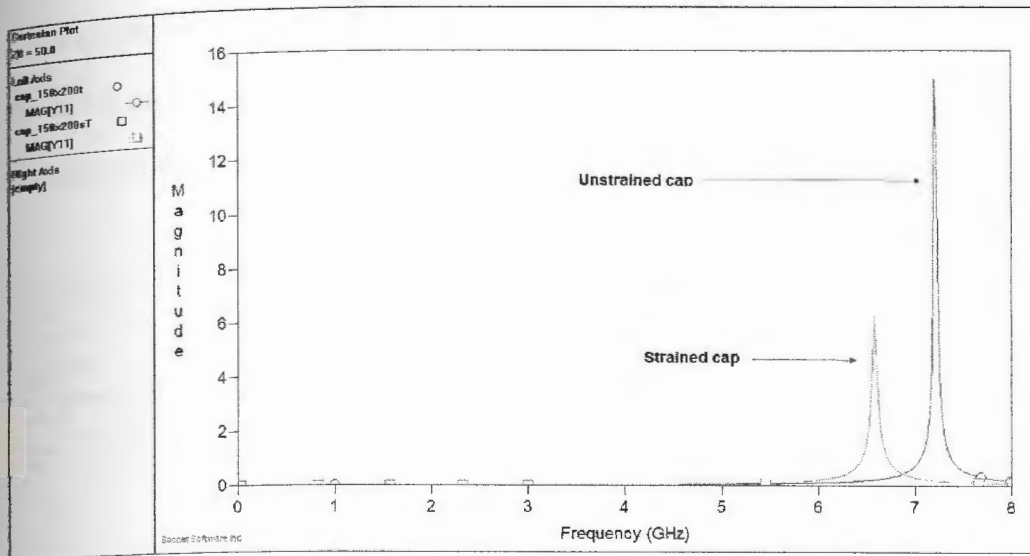


Figure 3.10 Resonant frequency of thick-film capacitor

The resonant frequency of the thick-film capacitor given by Sonnet Lite is 7.225 GHz, only about 0.1 GHz from the expected value. Figure 3.10 also shows the shift in the resonant frequency. When the thick-film capacitor is strained by about 20,000  $\mu$ strain, the resonant frequency moves to 6.575 GHz, for an estimated gage factor of 4.04, which is consistent with the gage factor obtained in the thin-film approach with no antenna element. Regardless of the gage factor, the resonant frequency was completely outside the 1 to 2 GHz range of operation targeted. Therefore, an antenna element was needed for the frequency range of interest. Naturally, the length of the antenna needed was expected to be longer than the 6-mm long antenna used for the thin-film approach. Unfortunately, an antenna length of more than 10 mm was not possible because of the size limitations of the constant strain beam. If the antenna would be longer, the interdigital capacitor had to be placed too close to the wider part of the strain beam.



A simulation with an antenna length of 6 mm and 10 mm long was executed to see the effect in lengthen the antenna. Figure 3.11 shows the change in the resonant frequency of the thick-film capacitor when the antenna was added.

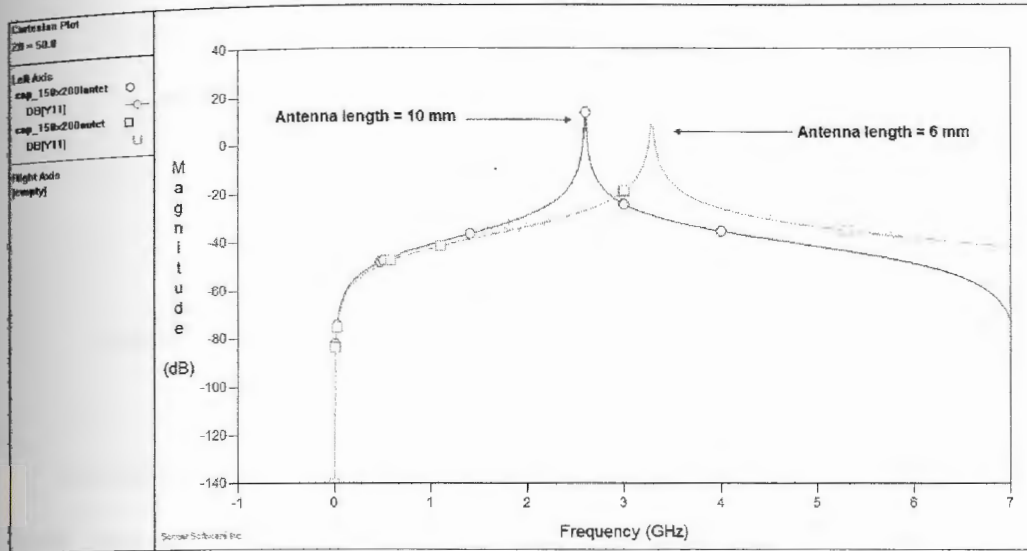


Figure 3.11 Effect of the antenna in the thick-film capacitor resonant frequency

A 6-mm antenna made the resonant frequency to decrease to 3.3 GHz, whereas a 10 mm antenna further lowered it to 2.6 GHz. Although this resonant frequency is still outside the desired range of operation, size limitations made the design remain with this antenna length for the fabrication stage.

A final, simulation was executed using the chosen 10-mm long antenna to see the effect of strain on the capacitor and to have an estimation of the expected gage capacitor in terms of resonant frequency. Figure 3.12 shows the simulation results given by Sonnet Lite for an applied strain of about 20,000  $\mu$ strain.

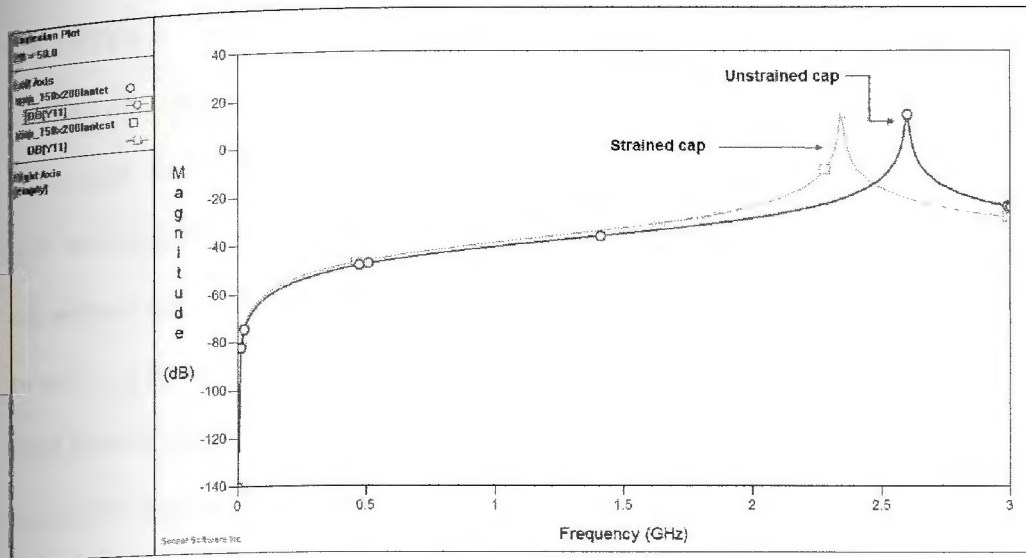


Figure 3.12 Shift in resonant frequency when using a 10-mm antenna

The resonant frequency of the capacitor shifted to 2.34 GHz, or a  $\Delta f = 0.26$  GHz when strain was applied and the estimated gage factor was 4.5. The gage factor is once again consistent with what had been seen so far in the previous simulations what led us to believe that either using a thin-film or thick-film approach, the gage factor that can be achieved with an interdigital capacitor is in the range of 4 – 5, and in terms of capacitance, the expected gage factor is around 11 and 14.

Therefore, two additional approaches were explored in order to increase the gage factor. This time, free standing structures were used to design a couple of transponders with the particularity that the sensing element is not completely attached to the surface of the substrate. Chapter 4 reviews the proposed designs, expected capacitance and projected gage factor.

## **CHAPTER 4 Free standing structure approach**

This chapter presents a different approach to solve the problem of the wireless strain gage. As mentioned in the previous chapters, the simulation results of the thin-film and thick-film capacitor designs yielded gage factors in the range of 11 – 14 for capacitance and gage factors between 4 -5 when measuring the shift in frequency with respect to a unstrained resonant frequency. It was of considerable interest to boost the gage factor as much as possible in order to maximize the resolution of the sensor, i.e. maximum capacitance or frequency change for a given strain value. Therefore, an additional literature review was performed at this stage of the research to consider other types of transponder designs with improved gage factors. One the technologies explored was the passive sensors used in automobiles, specifically the strain monitoring systems used to develop smart tires or tires with integrated sensors that measure their pressure or deformation during service (Todoroki et al. 2003; Matsuzaki and Todoroki 2005, 2006). In addition, the concept of mechanical amplification was explored by means of a buckled beam scheme incorporated to a capacitive strain sensor used for torque measurements among other applications (Young and Ko 2004; Guo et al. 2004, 2005). At the end, a buckled beam capacitor design was proposed as well as several modifications to the initial design.

The part of this chapter explains the second free standing structure investigated. In this case, the transponder was not formed by a capacitor or based on a capacitance change. Rather, the design proposed includes the use of an antenna as the sensing element. So by looking at the change in the tuning frequency of the antenna, the induced strain can be calculated. When strain is applied, the distance to ground along the antenna increases which modifies the frequency of operation of the antenna.

#### 4.1 Development of the buckled beam capacitor concept

The idea of the buckled beam capacitor came from the combination of two applications previously developed by other researchers; a wireless strain monitoring system for tires (Todoroki et al. 2003), using capacitance and tuning frequency changes; and second, a high-grain mechanically amplified MEMS capacitive strain sensor using a buckled beam scheme developed by Young and Ko (2004).

Todoroki (2003) proposed a wireless strain monitoring method that uses the tire itself as a sensor, attached to an oscillating circuit with a battery to activate it which made it a non-passive approach. Still, the steel wire belt of a tire is an electrically conductive material the rubber is a dielectric material, and all the structure together resembles a capacitor. Figure 4.1 shows the capacitor model of a steel wire belt of a tire.

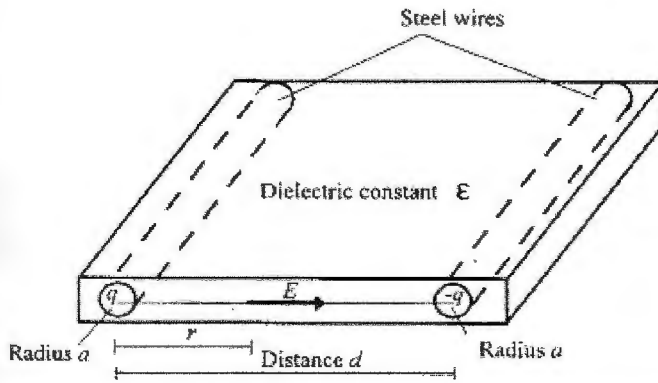


Figure 4.1 Capacitor model of a steel wire belt of a tire thread (Matsuzaki and Todoroki 2005)

In this model, the capacitance is given by

$$C = \frac{\pi \cdot \epsilon \cdot \epsilon_0 \cdot l}{\ln\left(\frac{d-r}{r}\right)} [pF] \quad (9)$$

where:  $C$  is the total base capacitance

$\epsilon$  is the dielectric constant of rubber

$\epsilon_0$  is the permittivity of free space ( $8.85 \times 10^{-12}$ )

$l$  is the length where the steel wire overlap

$d$  is the distance between two steel wires (center-to-center)

$r$  is the radius of a steel wire

Later, the authors improved their own design to produce a passive wireless sensor and enhanced the tire capacitance by building an interdigital electrode shown in Figure 4.2. It must be noted that the tire thread is made of several layers of woven steel wires, so an interdigital electrode was constructed by connecting several steel wires to form the electrodes of the capacitor.

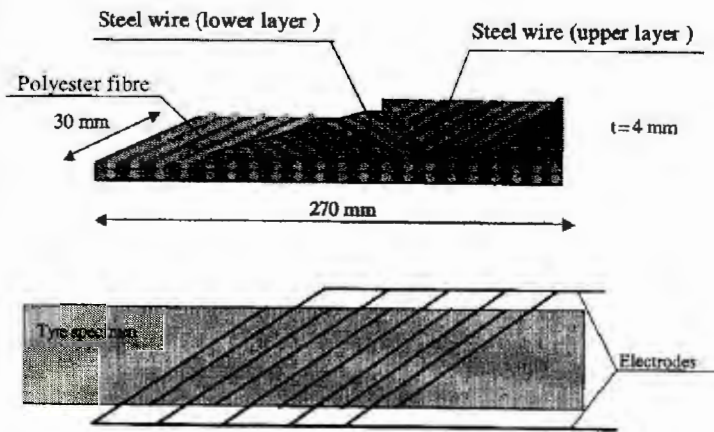


Figure 4.2 Tire specimen and interdigital electrode configuration (Matsuzaki and Todoroki 2005)

As tension was applied in the longitudinal direction of the tire thread, the total capacitance of the structure increased because the space between wires decreased; therefore, the tuning frequency decrease by  $f = \frac{1}{2\pi\sqrt{LC}}$ . The authors reported a base capacitance of 170 pF when the tire thread was not strained. This capacitance value increased to 260pF with 2000  $\mu$ strain applied. This was a  $\Delta C$  of 90pF which



yielded a gage factor of 264 in terms of capacitance. The authors also reported a resonant frequency of about 100 kHz since they used a 10 mH inductor to form a resonant circuit. When the same amount of strain was applied, the resonant frequency decreased to 85 kHz, for an estimated gage factor of 75 in terms of frequency. This is less than the gage factor in terms of capacitance as expected, since only the capacitance change is contributing the change in resonant frequency. This large gage factors led us to develop a capacitor made of small-diameter wires, with interdigitated electrodes, similar to the structure of a tire thread.

The other important component of the buckled beam capacitor design came from a mechanically amplified capacitive strain sensor based on the buckled beam amplification scheme developed by Guo et al. (2004). Figure 4.3 shows the schematic diagram of this amplification scheme.

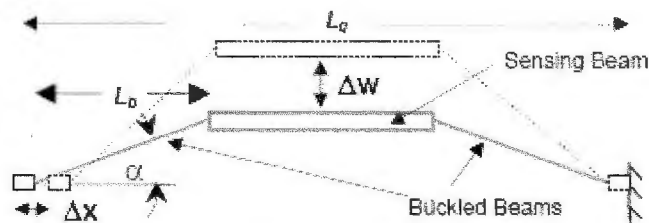


Figure 4.3 Schematic of buckled beam amplification scheme (Guo et al. 2004)

The principle of operation is based on the fact that when strain is applied, a small lateral displacement,  $\Delta x$ , is induced. If the buckling angle,  $\alpha$ , is small, i.e. less than  $10^\circ$ , then the center deflection of the sensing beam,  $\Delta w$ , is larger than the lateral displacement,  $\Delta x$ , which results in a mechanical amplification. For their application, the authors determined that the best angle  $\alpha$  was  $5.7^\circ$  based in their nominal gain and

gain errors as a function of buckling angle. This was starting point for the present design. At the end, the limitation in the footprint of the buckled-beam capacitor and the overlapping area of the interdigital electrodes determined the angle for our design as it is discussed in the following section.

The authors fabricated a device using MEMS technology that had a sensitivity of 282 aF/ $\mu\epsilon$ , with a base capacitance of 0.44 pF, for an estimated gage factor of 640. Again, the large gage factor reported by the authors led us to explore the buckled beam approach to develop a capacitor, also using interdigitated electrodes.

#### 4.1.2 Design parameters

For the design of the buckled-beam capacitor, several key factors were taken into account among which was the footprint of the sensor, the total base capacitance and the buckled-beam angle. As mentioned in the previous section, the buckled-beam angle with the largest amplification occurs when the buckled-beam is set at  $6^\circ$  from the horizontal axis. Such a small angle has several complications when designing the capacitor. Among the difficulties faced were the fact that the smaller the angle the longer the buckled beams. Longer buckled beams result in less space to place the interdigital electrodes, in this case made out of metal wires. The fewer interdigital wires, the smaller the capacitance is, which then leads to a smaller resonant frequency which may be outside the desired range of operation. Additionally, longer buckled beams mean that the ratio between center of deflection  $\Delta w$  and the distance  $w$ , i.e. the distance from the base of the interdigital wires to the horizontal of the buckled beams, is smaller. Thus, the capacitance change is smaller compared to shorter buckled beams. Therefore, as an initial design, it was decided to start with a buckled beam angle of  $10^\circ$  with respect to the horizontal axis as shown in Figure 4.4.

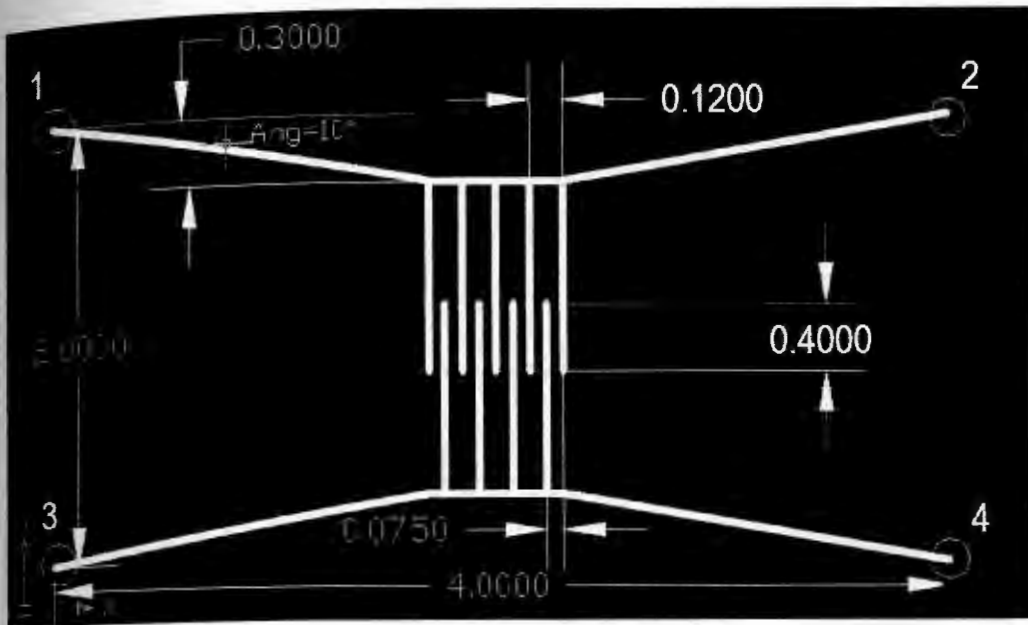


Figure 4.4 Schematic of the buckled beam capacitor

Several observations need to be made from Figure 4.4. It must be noted that the number of wires shown above are not the total number of wires used in the design and are only shown for reference purposes. Additionally, all the dimensions shown above are in millimeters and the buckled beam capacitor is represented by the thick white lines.

Figure 4.4 also shows four circles; these circles are parts of the structure that need to be pinned to the strain beam. Thus, when strain is induced, the mechanical amplification of the buckled beam scheme would be transferred into a larger change in the overlapping length of the interdigital fingers, and therefore, yielding a larger change in capacitance. Furthermore, the joint points circled by 1 and 2 not only have to attach the top rail (non-grounded electrode) to the substrate, but also these joint points have to isolate the top rail from the substrate or ground plane. The reason for



this was that the antenna is meant to be connected to the top rail and then the tip of the antenna would be grounded, grounding the entire top rail. Similarly, the joint points circled by 3 and 4 are parts of the structure that not only had the purpose of pinning the bottom rail (grounded electrode) of the capacitor but also for grounding purposes. It is worth to mention at this point that the buckled beam capacitor was meant to be fabricated on titanium constant strain beams similar to the ceramic constant strain beams used to fabricate the thin-film and thick-film capacitors. More details on how the top and bottom rail of the buckled beam capacitor are pinned to the substrate are discussed in Chapter 5

The following table summarizes the parameters of the initial buckled beam capacitor design.

Table 4.1 Parameters of initial buckled beam capacitor design

<b>Metal type</b>	Nickel
<b>Wire diameter (<math>2r</math>)</b>	50 $\mu\text{m}$
<b>Wire spacing</b>	10 $\mu\text{m}$
<b>Wire distance center-to-center (<math>d</math>)</b>	60 $\mu\text{m}$
<b>Overlapping length (<math>l</math>)</b>	400 $\mu\text{m}$
<b>Number of wires (<math>N</math>)</b>	16 (8 in top rail and 8 in bottom rail)

Kapton tape (polyimide) was used as isolation. However, this dielectric material was not meant to be used as the dielectric layer of the capacitor. Instead, kapton tape was used to isolate the interdigital wires from the titanium strain beam; otherwise, the

wires and substrate would come in contact since both are made from conductive materials. Therefore, the top and bottom rails connected to the wires were located on top of an insulation layer of kapton tape. The dielectric that is between the wires of the interdigital capacitor is air ( $\epsilon=1$ ).

Finally, the initial design was arranged in such way so the buckled beam amplification scheme would be implemented. Both the top and bottom rails that form the capacitor were setup parallel to the horizontal axis of strain, i. e. the wire electrodes are perpendicular to the axis of strain.

#### 4.1.3 Expected base capacitance and gage factor

Based on the design parameters, the total capacitance of the buckled beam capacitor can be determined, as well as the change in capacitance that would be introduced due to strain in the long axis of the titanium beam.

Using equation (9) multiplied by the number of wires in the interdigital capacitor, and the design parameters from Table 4.1, the capacitance is given by:

$$\text{(Unstrained base capacitance)} \quad C = \frac{\pi(1)(8.85 \times 10^{-12})(400 \times 10^{-6})(16-1)}{\ln\left(\frac{(60 \times 10^{-6} - 25 \times 10^{-6})}{25 \times 10^{-6}}\right)} = 0.4958 pF$$

According to Figure 4.4, the distance  $w$ , from the base of the interdigital wires to the horizontal section of the buckled beam is  $300 \mu\text{m}$ . When  $100 \mu\text{strain}$  is applied to the buckled beam capacitor, a displacement  $\Delta x = 0.2 \mu\text{m}$  is introduced. This is comes from the following calculations:

$$\text{(Unstrained)} \quad x = \frac{300 \times 10^{-6}}{\tan 10^\circ} = 1.7013 \text{mm}$$

$$\text{(Strained)} \quad x' = x(1 + \varepsilon) = x(1 + 100 \times 10^{-6}) = 1.7015 \text{ mm}$$

$$\Delta x = 0.2 \mu\text{m}$$

The displacement  $\Delta x$  translates into a decrease in the distance  $w$  from  $300 \mu\text{m}$  to  $298.8 \mu\text{m}$ , or a  $\Delta w = 1.8 \mu\text{m}$ , which provides the mechanical amplification scheme of the buckled beam.

As  $\Delta w$  changes the length in the region where the interdigital wires overlap the capacitance decreases. The wires overlapped  $400 \mu\text{m}$  when no strain was applied and when the titanium beam is strained, the overlapping length decreases to  $398.8 \mu\text{m}$ . Similarly, using equation (9), the capacitance value when strained is given by:

$$\text{(Strained capacitance)} \quad C = \frac{\pi(1)(8.85 \times 10^{-12})(398.8 \times 10^{-6})(16-1)}{\ln\left(\frac{(60 \times 10^{-6} - 25 \times 10^{-6})}{25 \times 10^{-6}}\right)} = 0.4943 \text{ pF}$$

Therefore,  $\Delta C = 0.0015 \text{ pF}$  for  $100 \mu\text{strain}$ , which yields a gage factor of approximately 30. It is important to note that the change in the overlapping length is the contribution of only one side of the buckled beam capacitor. So, if both top and bottom rails of the capacitor move similarly when strain is applied, then  $\Delta C = 0.0030$  for a gage factor of about 60. The steps followed to fabricate the buckled beam capacitor are explained in Chapter 5.

#### 4.2 Antenna strain gage design

The antenna strain gage concept was based on the idea that the resonant frequency of an antenna can vary depending on the distance between the whole length of the antenna and the ground plane. This phenomenon was observed in a very thin antenna

prototype developed by Argon ST (formerly SDRC). In the initial configuration, an 8-mm long copper tape antenna was placed over a 50- $\mu\text{m}$  layer of kapton tape. The frequency of resonance of the antenna was 4.83 GHz. Figure 4.5 shows the sketch of the initial configuration of the very thin antenna.

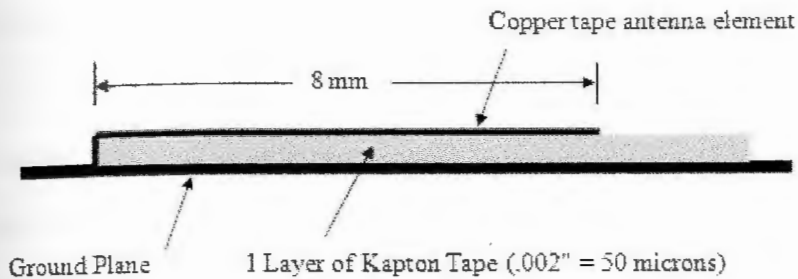


Figure 4.5 Side view of antenna element (not to scale); initial configuration

Then, the design was modified so the antenna height was doubled over just one-third of its original length. The result was a resonant frequency shift of 280 MHz, from 4.83 GHz to 5.11 GHz. A gage factor was not calculated from this design since no strain was introduced; rather, the distance between the antenna and the ground plane was increased during fabrication. Figure 4.6 shows the sketch of the antenna height modification.

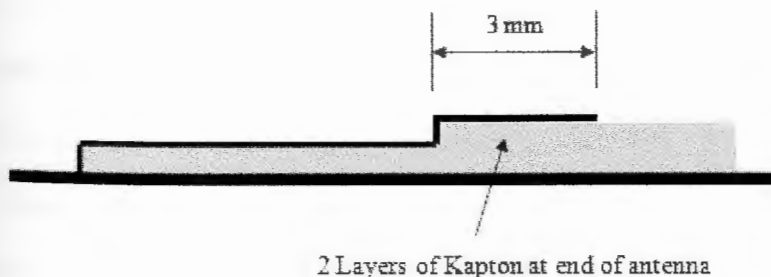


Figure 4.6 Side view of antenna height modified configuration (not to scale)

A 5.8% change in frequency was observed in this prototype, compared to a 2.2% shift in frequency obtained by one of the designs of the buckled-beam capacitor (See Chapter 6, section 3). Based on these results, an antenna strain gage design was developed using the very thin antenna prototype and combining it with the concept of free standing structures.

#### **4.2.1 Antenna gage configurations**

As seen in the very thin antenna prototype, the length of the antenna was 8 mm, which yielded a frequency of resonance close to 5 GHz. For our study, we wanted to decrease the frequency of operation to at least below 3 GHz. Therefore, the first approach was double the length of the antenna to 16 mm. One of the problems of using larger sensing elements is that the strain measurements are not a spot measurement of strain and rather an integration of the strain along the entire antenna element.

The antenna was made of tungsten wire with 50  $\mu\text{m}$  in diameter. The material and diameter wire were chosen because small diameter and stiffer wires are not affected by large “g” loading, as long as the entire structure is thinner than the boundary layer of the gas path flow in a rotating blade. Additionally, a titanium frame was built around the antenna wire and it was designed only for protection purposes. Titanium was the material of choice since the constant strain beam was also made of titanium, so the fabrication process would be simplified. Finally, the initial configuration also included a diode so the frequency of resonance could be measured wirelessly. The diode would generate a second harmonic, with a frequency twice the fundamental frequency of resonance of the antenna; this would allow distinguishing the Rx signal



from the Tx signal. Figure 4.7 shows the top view of antenna strain gage design proposed.

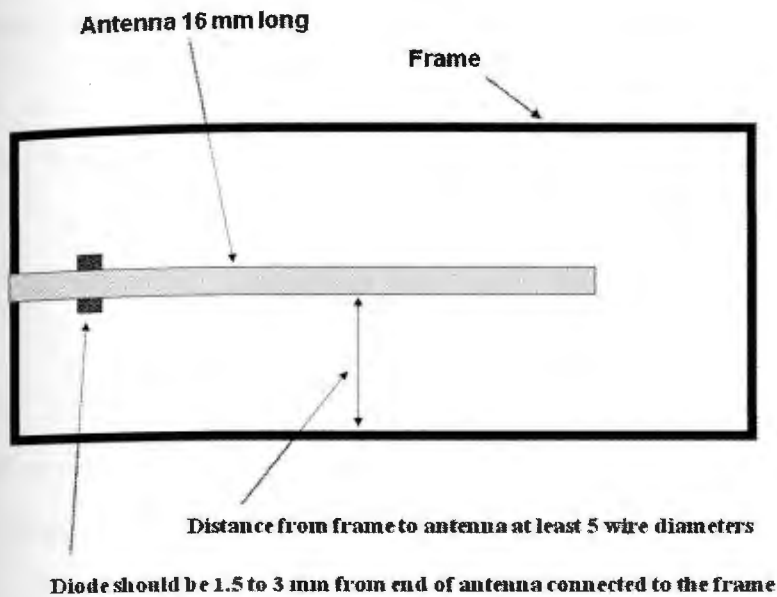


Figure 4.7 Top view of strain antenna design

As shown in the previous figure, the antenna wire had to be kept at least 5 wire diameters from the frame so the frequency of resonance is not affected by the titanium frame that surrounds the wire. In addition, the diode needed to be placed between the antenna wire and the ground plane and at distance between 1.5 to 3 mm from the base of the antenna connected to the frame. Figure 4.8 shows a side view of the same design. It must be noted that a layer of kapton tape was placed at the tip of the antenna so it would not come in contact with the ground plane.



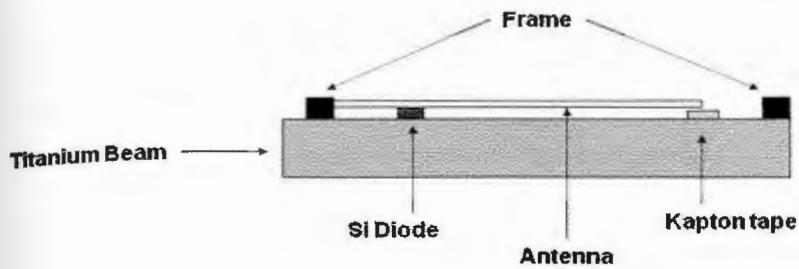


Figure 4.8 Side view of strain antenna design

Once the prototype was fabricated (See Chapter 5, section 4), the initial prototype was tested to measure its resonance frequency and the second harmonic produced, as well as the effect of strain and how much change in frequency would be obtained. Unfortunately, as discussed in Chapter 6, section 4, the expected frequency of resonance was about 3 GHz, which means that the backscattered signal would be twice as much that frequency. This required different filters, amplifiers and Tx/Rx antennas. Therefore, a slight change in the design was made by increasing the length of the antenna and increasing the starting height of the antenna from 25  $\mu\text{m}$  to 75  $\mu\text{m}$  to prevent the antenna from being too close to ground.

The antenna was lengthened enough to move the resonance near the 2.4 GHz band. In this band, much higher power and cheaper amplifiers were available for RF measurements. Therefore, the length of the antenna was increased to 27 mm. Figure 4.9 shows a top and side view of the modified antenna gage design.

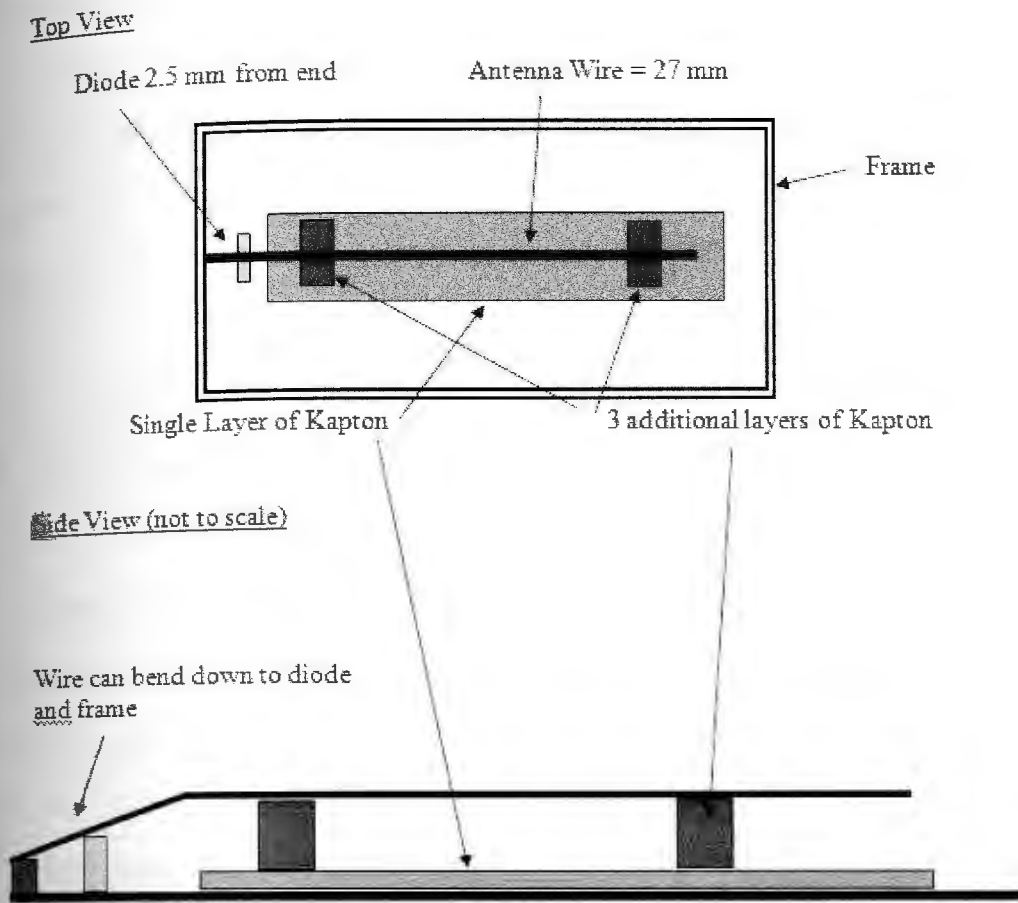


Figure 4.9 Top and side view of modified antenna gage design

Three different prototypes were fabricated: one for the initial configuration and 2 for the modified design. One of the prototypes fabricated using the modified configuration did not include a diode; instead a solderable wire was placed. The purpose of this wire was to be able to attach an external diode. More details on the fabrication of these prototypes in Chapter 5.

## CHAPTER 5 Fabrication process

This chapter discusses the different fabrication process used for all four different designs. The first ones to be discussed are the fabrication steps for the thin-film and thick-film capacitors which are quite similar. Later in this chapter, the fabrication process for the free-standing structures is discussed.

### 5.1 Fabrication steps of thin-film interdigital capacitor

The fabrication of the thin-film interdigital capacitor involved several steps. Before the description of these steps, it is important to mention that the interdigital capacitors were deposited on ceramic constant strain beams. These substrates are fabricated with a material called YSZ (yttria-stabilized zirconia). Figure 5.1 shows one of the YSZ substrates used throughout the fabrication process.

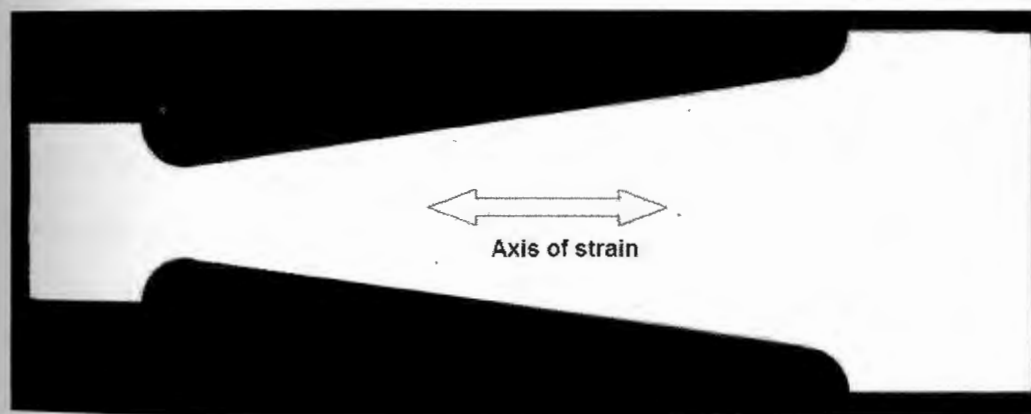


Figure 5.1 YSZ ceramic constant strain beam

The particular shape of the strain beams allows depositing the sensor anywhere on along the center line of the long axis of the substrate and still induce a constant strain. However, it was decided to place the interdigital capacitor as close as possible to the

center of the strain beam, with the antenna element perpendicular to the axis of strain. That is why there is a limitation in the length of the antenna to 6 to 7 mm; otherwise the sensor would be deposited too close to the narrower part of the beam or too close to the wider part.

For the fabrication of these sensors, the YSZ substrate is cleaned by rinsing it with de-ionized water, acetone and methanol. Then, it is blown dry with nitrogen, followed by a bake for 10 to 15 minutes at 135° C.

Then, a photolithography process is used to deposit both the bottom and top layers of the interdigital capacitor. For these purposes, a photomask with the sensor pattern was designed using AutoCAD according to the design parameters discussed in Chapter 3. First, LOR 10B polyimide is spin-cast on the substrate at 500 rpm for 15 seconds followed by spinning at 2500 rpm for 45 seconds, resulting in a nominal thickness of 10 $\mu$ m. Then, the substrate is baked at 139° C for 15 seconds. Once the substrate cools down, SC1827 photo-resist is spin-cast on the substrate, for 500 rpm for 15 seconds followed by spinning at 2500 rpm for 45 seconds. Then, the substrate needs to be baked for 2 minutes and 40 seconds at 110° C. Next, the photomask with the pattern is placed over the photo-resist layer and it is exposed to UV light for 6:45 minutes. Care needs to be taken when exposing the substrate to UV light, not to over or under expose it. Next, AZ developer is applied to the exposed resist layer to achieve a clear and well-defined pattern. The last step in the photolithography process is to hard bake the substrate for 10 minutes at 139° C. After this process, the ceramic strain beam has a clear pattern of the sensor so a thin-film layer of metal can be deposited.

The thin-film is deposited using a sputtering machine. The metal of choice is copper since it is a material that does not take long time to sputter, especially when

the thickness of the metal is around 1  $\mu\text{m}$ . For more details on the sputtering process, see Appendix C. After the metal is deposited, a process called lift-off is required to remove the additional metal deposited and have a clear metal interdigital electrode. Lift-off is achieved by soaking the substrate in acetone for a few minutes. Acetone attacks the LOR/photo-resist layer that remains under the metal layer and that is not part of the pattern. Figure 5.2 summarizes the photolithography and lift-off processes. For more information on these procedures, see Gardner et al. (2001)

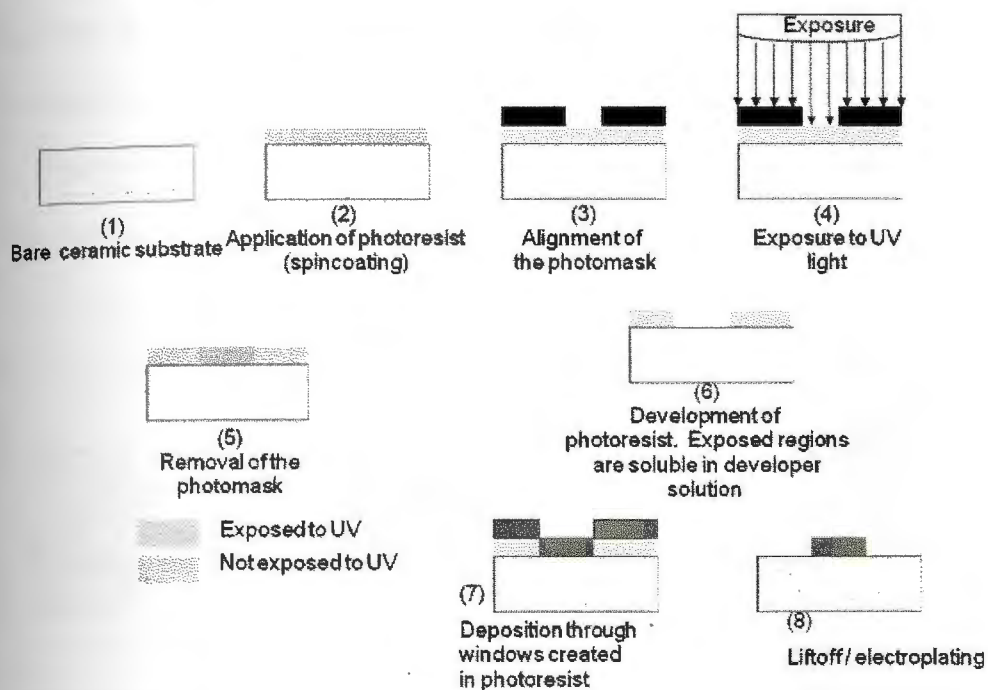


Figure 5.2 Photolithography and lift-off process

The process just described takes care of the bottom layer of the interdigital capacitor. Then, the dielectric material needs to be deposited. The material used is a LOR 50B polyimide that is also spin-casted on the substrate. Depending on the rpm's used, the thickness of the polyimide can vary. For our case, the LOR 50B was spin-casted for 45 seconds at 1000 rpm, following the specifications of the manufacturer



MicroChem). The desired thickness of the dielectric is about 8  $\mu\text{m}$ . Then the LOR 50B is baked above 250  $^{\circ}\text{C}$ .

Next the process repeats for the top layer of the interdigital capacitor, following the steps previously described. The final step in the fabrication process of this interdigital capacitor design is to sputter copper on the back of the beam for ground plane. Both the bottom and top electrodes are grounded through the edge of the ceramic strain beam. The sputtering process sputters copper all over the edge so at the end, both the antenna element and the large piece of metal of the bottom layer are connected to the ground plane.

Figures 5.3 and 5.4 show the front and back views of a fabricated interdigital thin-film capacitor with an antenna length of 7 mm.

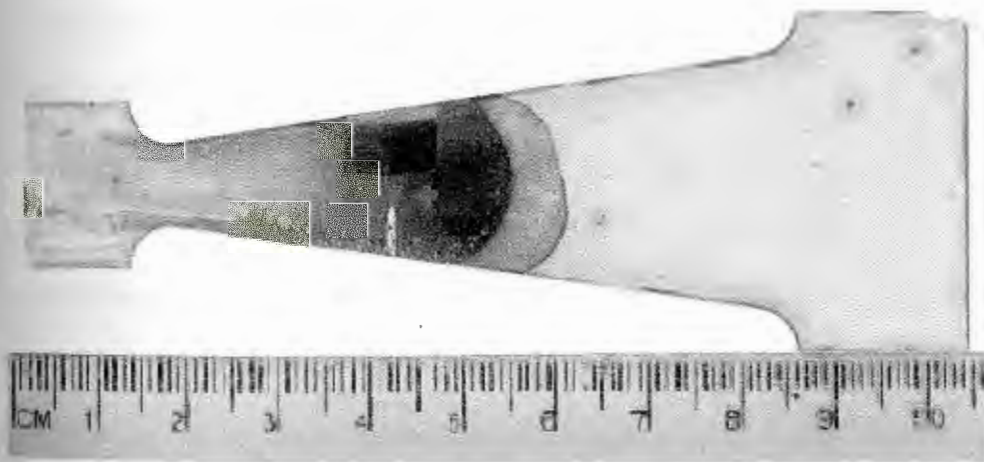


Figure 5.3 Front view of thin-film capacitor



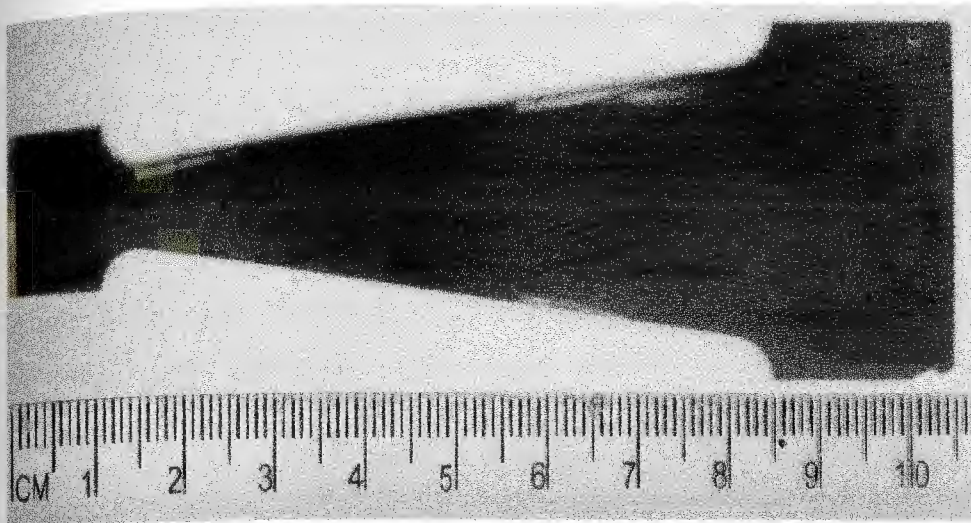


Figure 5.4 Back view of thin-film capacitor: ground plane

Several issues had to be addressed during the fabrication process of the thin film capacitor. One of the biggest difficulties was the deposition of the dielectric material in between the metal layers. As mentioned before, a material called LOR 50B was used as the dielectric layer. This material needed to be fired up to above 250 °C for about 25 minutes in order to change its properties, evaporate some of the compounds that make it sensitive to acetone. It is important to point out that during the lift-off process of the second metal layer acetone comes in contact with the LOR 50B dielectric layer. If this material is not heated up such high temperature, the dielectric layer is dissolved by acetone and when the second layer of metal is deposited, the interdigital electrodes may come in contact, shorting the capacitor.

In the other hand, care was taken when firing up the LOR 50B. Some initial tests using this material showed that if the substrate is heated up too rapidly, bubbles develop on the surface of the ceramic substrate, specifically in the area where the LOR 50B was spin-casted. This is because the temperature of the LOR 50B is increased so suddenly that the evaporated compounds get trapped in bubbles.

Eventually, these bubbles disappeared when the substrate temperature reached 200 °C but left a very rough and irregular surface. Such surface is not suitable for depositing the metal film, since the thickness of the film is only 1 μm and some of these irregularities were more than 1 μm thick. This is the reason why the temperature has to be increased slowly, at a rate of about 8 °C per minute, during 25 minutes. Still, some bubbles developed on the surface of the ceramic substrate, especially on the edge of the substrate as shown in Figure 5.3, in the lower edge of the sensor area.

Three different thin-film interdigital capacitors were fabricated during this stage. For pictures and more details on the remaining two interdigital capacitors, refer to Appendix D.

## 5.2 Fabrication steps of thick-film capacitor

The thick-film capacitor was fabricated following a process similar to that of the thin-film capacitor. Using photolithography was used to create the electrode pattern and then deposit a thin film by sputtering copper on the surface of the ceramic substrate. The only difference is that, this time, the thin-film electrode thickness was increased by electroplating. As mentioned in Chapter 3, the electrodes of the capacitor should be thicker to avoid the skin effect between 1 to 2 GHz.

The electroplating was accomplished by connecting the negative terminal of a DC power supply to the object. Likewise, the positive terminal of the DC power supply was connected to the platinum surface electrode. Figure 5.5 shows a schematic of the electrical circuit used for thickening the sputtered thin-film electrodes by electroplating.

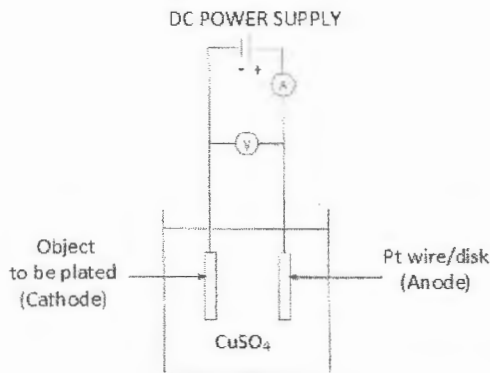


Figure 5.5 Schematic of electric circuit for electroplating

As shown in the previous figure, the anode was initially made of a platinum wire. Unfortunately, the surface area of the wire was much smaller than the surface of the capacitor electrodes to be plated. Therefore, the wire was substituted by a larger silicon wafer with a layer of platinum previously deposited. Additionally, the solution used for plating the thin films was cupric sulfate ( $\text{CuSO}_4$ ) and water ( $5\text{H}_2\text{O}$ ). Another observation for the electroplating process is that both the cathode and the anode need to be in parallel so copper is deposited evenly on the surface of the interdigital capacitor electrodes.

Several attempts were made to find the best deposition rate and conditions. The deposition rate depends on the current applied to the circuit and the time the current runs through the circuit. Likewise, the electric current depends on the applied DC voltage as well as, on the distance between the cathode and anode. In our experiments, this distance was no more than 4 cm and a variable current supply of 9 V was used to control the current. Some of our initial tests showed that the higher the deposition rate, the worse the definition of the electroplated metal lines. Thus, the contour of the original thin film becomes more distorted and metal grows beyond the

original boundaries of the metal. This is especially critical in the case of the interdigital fingers since the spacing between the interdigitated electrodes is only a few micrometers. Thus, better results were achieved by extending the deposition time and lowering the deposition rate. The best deposition rate in our experiments in terms of definition was  $3\mu\text{m}/\text{minute}$  and this was achieved by applying 200 mA of current and keeping the cathode and anode distance at approximately 3 cm, requiring just 3 minutes to achieve a total thickness of  $10\ \mu\text{m}$ .

Once the lower metal layer was electroplated, a layer of kapton tape applied to form the dielectric. Ideally, the kapton tape should only be applied underneath the interdigitated fingers, to keep the antenna on top of the ceramic substrate, and not on top of the dielectric. Unfortunately, for the reasons previously mentioned in the design chapter, the kapton tape had to be placed underneath the upper metal layer as seen in Figure 5.6.

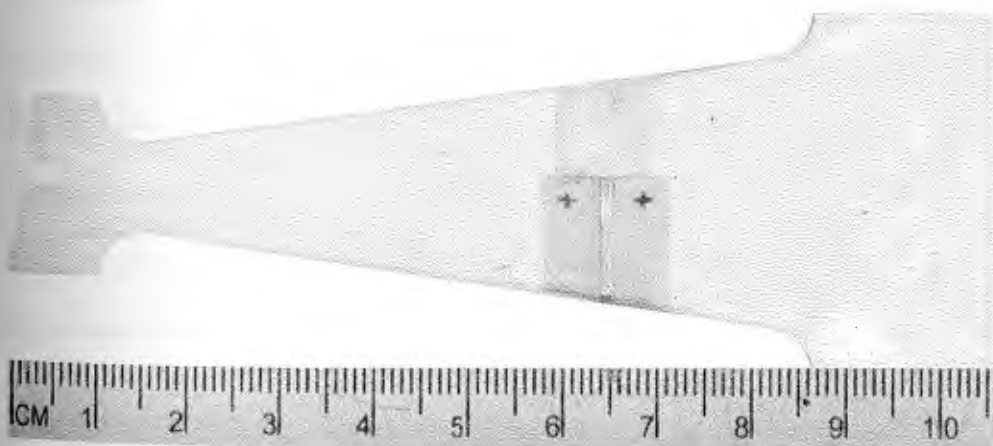


Figure 5.6 Thick-film capacitor fabricated by electroplating

After the kapton tape was applied, the upper thin-film layer was deposited using photolithography and sputtered copper deposited onto the surface of the ceramic



strain beam. Then, the thin film was electroplated onto the copper using the same procedure described above. The final steps in the fabrication of the thick-film capacitor were the deposition of the ground plane by sputtered copper on the back of the ceramic substrate and make a physical connection from the top and bottom metal layers to the ground plane by applying silver paint on the edge of the ceramic beam. Once again, DC measurements were performed before the electrodes of the capacitor were shorted to ground. An additional thick-film capacitor was fabricated but the quality of the interdigital electrodes was not good enough since some of the fingers were shorted due to a too rapid deposition rate. Details on this prototype can be found in Appendix D.

### **5.3 Fabrication steps of buckled beam capacitor**

The fabrication steps used for the implementation of the buckled beam capacitor were completely different from those used to fabricate the thin-film and thick-film capacitors. No photolithography steps or sputtering processes were involved since no thin films were necessary. Instead, small wires were mounted on a metal wire rail and were welded together to create a buckled beam interdigital capacitor. Moreover, the constant strain beams up to this point were made of YSZ (yttria-stabilized zirconia) but in the case of the buckled beam capacitor, titanium constant strain beams were used. The reason for this is that an electrical connection from one of the electrodes or rails of the capacitor to ground was required. Instead of sputtering copper onto the back of the ceramic strain beam, the titanium strain beam would act as ground plane itself.

Figure 5.7 shows a cross-section of the buckled beam capacitor. In this figure, the buckled beam consisted of wires attached to the ground plane over the dielectric layer that serves as an isolating material. The dielectric material, in this case was a 25- $\mu\text{m}$

thick sheet of kapton tape that was used to prevent the capacitor interdigital fingers from contacting the ground plane. Furthermore, as mentioned in the design section of the buckled beam approach, one of the rails/electrodes had to be grounded whereas the other rail was floating; both rails have to be attached to the titanium beam at the same time.

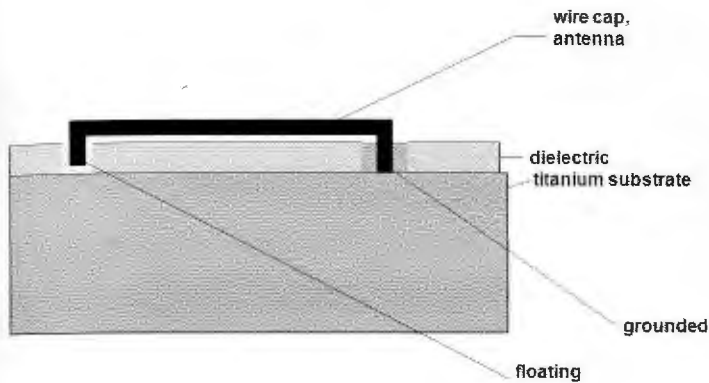


Figure 5.7 Cross-sectional view of buckled beam capacitor

In order to attach the buckled beam rails to the titanium beam, a conductive and non-conductive connection were required for the bottom and top rails, since the first rail had to float and the other had to be grounded. Therefore, silver epoxy and non-conductive epoxy were used for these connections respectively.

The first step in the fabrication process was to roughen up the surface of the titanium beams using a piece of SiC paper to remove the oxide layer and make good electrical connections to ground. Then, a small piece of kapton tape applied to the surface approximately at 6 cm from the narrow end of the strain beam. Next, small cuts were made in the kapton tape so the top and bottom rails could be attached to the titanium substrate. Before attaching the electrodes to the rails the larger diameter wires had to be bent to form a  $10^\circ$  as specified by the design. The rails were too stiff



to bend to the desired angle. Instead, as shown in Figure 5.8, both the top and bottom rails were bow-shaped. As a consequence, the mechanical amplification scheme of the buckled beam was diminished.

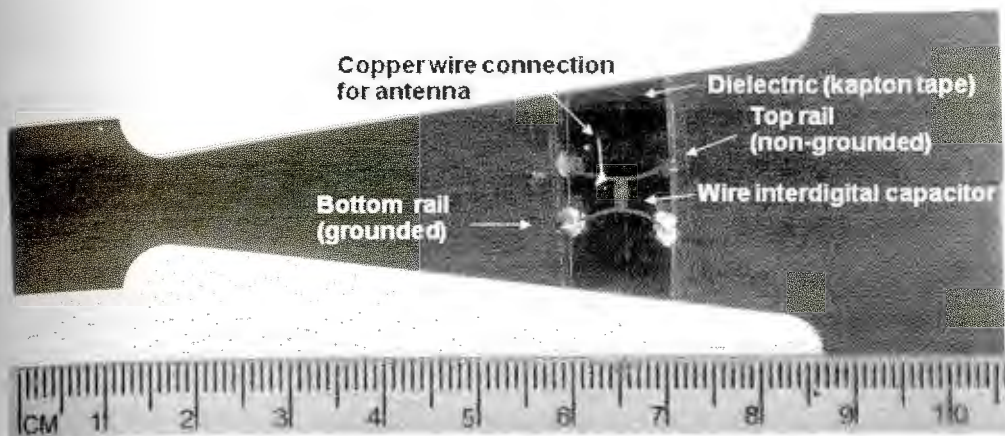


Figure 5.8 Photograph of buckled beam capacitor

The next step in the fabrication was to apply a small drop of epoxy to the grounded and non-grounded rails. The material used for the conductive epoxy was Metaduc 1202 base, fabricated by Mereco Technologies, with 2 parts of epoxy per 1 part of Metaduct 1202 activator. The most difficult part of fabricating the buckled beam capacitor was to make sure the interdigital electrodes did not contact each other and that the overlapping length was as close as possible to the 400  $\mu\text{m}$  design length. Using a microscope, the top and bottom rails were align to the notches in the kapton tape, and small drops of epoxy were applied to the four joint points. As seen in the figure 5.8, large globs of silver and non conductive epoxy were used to pin the top and bottom rails which further decreased the amplification effect of the buckled beam. Finally, the epoxy was let dried out for around 8 hours to make sure the buckled beams stayed attached to the titanium substrate when strain was applied.

Two additional buckled beam capacitor designs were developed as well. The reason was that the original design did not yield the results and a number of parasitic capacitances were introduced during the fabrication process due to the large globs of epoxy. These capacitances were of greater magnitude than the designed base capacitance allowed in the design. Thus, the  $\Delta C$  was smaller with respect to the total base capacitance (including the parasitic capacitances), which led to a smaller gage factor. The modifications to the original buckled beam capacitor are described in Appendix E.

The fabrication steps used in the modified designs were similar to those described above. However, the greatest difference was in the way the top and bottom rails were attached to the titanium substrate. For the last buckled beam design, laser welding was used instead of silver epoxy to attach the bottom rail to ground. Furthermore, the length of the buckled rails was shortened in one of the designs and the thickness of the kapton tape was increased to see the effect on the parasitic capacitances. Additional details are discussed also in Appendix E.

#### **5.4 Fabrication steps of antenna strain gage**

The steps followed to fabricate the prototypes, for the most, used a similar laser welding technique than the latest buckled beam design. Basically, the prototype consisted of 5 components: the titanium strain beam, the titanium frame, the tungsten antenna wire, a layer of kapton tape and a silicon diode.

First, the surface of the titanium strain beam was roughed up with sand paper. Then, the frame was built with four small titanium shims, all of them welded by a laser beam. The next step was to attach the tungsten wire to the metal frame, also by means of a laser-welding machine. One of the most difficult steps in this process was

to attach the diode to the tungsten wire. This was done also by aiming the laser beam to the join of the wire and the surface of the silicon diode. Some of the diode material was removed and melted by the laser, so the melted material would attach the two pieces together. After these three pieces were all connected, a layer of kapton tape was placed on the substrate. Finally, the last step was to weld the frame to the substrate by shooting the laser beam at an angle of 45 degrees at the joint of the two pieces. The laser parameters used in every step of the fabrication process are included in Appendix F, as well as some observations and comments.

Figure 5.9 shows the prototype fabricated with the initial configuration. Appendix G includes the two additional prototypes fabricated using a longer antenna wire and additional kapton tape layers.

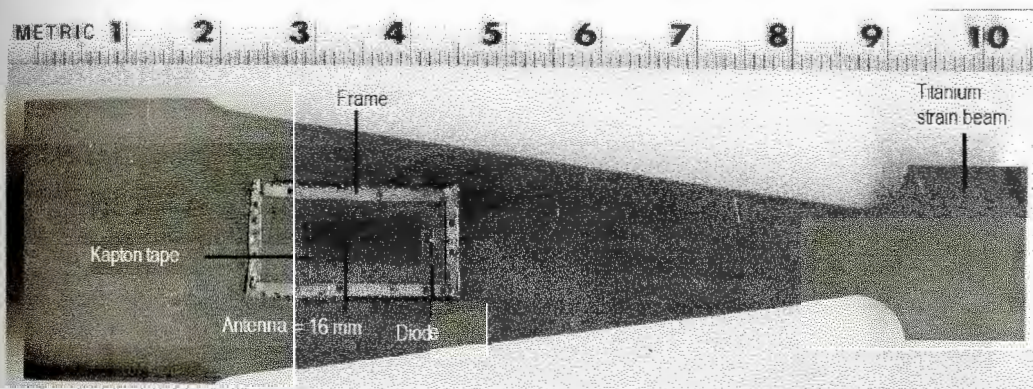


Figure 5.9 Antenna strain gage fabricated according to original parameters

## CHAPTER 6 Testing and results

This chapter explains the testing procedures used to verify the estimated capacitance, resonant frequency and gage factor for the different approaches used in this study. Most of the testing performed at URI was DC measurements because of the limited measuring capability at higher frequencies. High frequency measurements were performed by San Diego Research Center (SDRC), now Argon ST, since they had the appropriate filters, amplifiers, Tx/Rx antennas and signal processing equipment to test all of the prototypes fabricated at URI

Before presenting the test results of the different capacitor and antenna designs, an initial assessment of the ceramic substrate was performed. The purpose was to determine the dielectric loss of ceramic substrate at these frequencies. It is important to note that these measurements were performed by SDRC but provided important insight when designing and fabricating the sensors.

The loss tangent of the material was quite high, about -19 dBi peak gain. Such a low gain would impact the ability to measure the back-scatter signal. However, this was solved by using a Tx signal with a 20 to 30 dBm of power and placing the Tx antenna as close as possible to the strain beam under test. In addition, an antenna of similar dimensions was used for the thin-film and thick-film capacitors, i. e. 1 mm x 6 – 10 mm was deposited on the ceramic substrate. Because the material was lossy, the antenna had a Q value of about 25. In order to track the back-scattered signal, a change in capacitance had to be as large as possible.



### 6.1 Thin-film capacitor: analysis and results

Capacitance measurements were performed on the three different thin-film capacitors by means of a capacitance meter with a resolution of 0.01 pF in the range of 0.01 to 10 pF. The following procedure was used: the ceramic beams were clamped at the narrower end while applying stress to the wider end of the ceramic beam in bending mode. The ceramic constant strain beams used were designed to have the same strain along the longitudinal axis of the substrate. For this specific substrate, the strain introduced by deflecting the end 2 cm is about 800  $\mu$ strain. So the gage factor was estimated by relating the change in capacitance from the base capacitance when 800  $\mu$ m strain was applied.

The capacitance measurements for the 3 thin-film capacitors fabricated are as follow:

Table 6.1 Capacitance measurements of thin-film capacitors

Antenna length (mm)	Unstrained (base cap pF)	Strained (800 $\mu$ s) pF	$\Delta C$ (pF)	Gage Factor (G= $\Delta C/C \cdot 1/\text{strain}$ )
6 (broken)	1.90	1.92	0.02	13.15
6	8.40	8.42	0.10	14.88
7	7.25	7.30	0.05	8.62

The thin-film capacitor was designed to have a base capacitance of about 4.9 pF. From the measurements above, it can be seen that two of the fabricated capacitors had a capacitance value above the aimed base capacitance whereas, the other capacitor had a very small base capacitance. The reason for the small capacitance of the latter capacitor with an antenna length of 6 mm (broken when strained) is that the interdigital fingers were not aligned correctly during fabrication. Thus, the overlapping area was smaller than originally designed and a decrease in the total capacitance was observed. In the other designs, the reason for the larger total

capacitance was that the dielectric layer would have to be thinner than the originally 10  $\mu\text{m}$  design. Still, the gage factor of the two thin-film capacitors was about 14 which is what was anticipated from the simulations.

For the high frequency measurements, a test cable (micro-coax) was soldered to one of the fabricated sensors to verify the resonant frequency vs. strain behavior. Unfortunately, some of the deposited metal layer vaporized when in contact with the soldering iron. Even though the micro-coax was attached, no resonant frequency was found in any of the three the thin-film transponders. At first, it was believed that the ground plane was too thin so additional copper tape was placed on the bottom surface of one of the ceramic beams. Still, no discernible resonance between 1 to 6 GHz was observed. It was suspected that either the capacitor became shorted or the capacitance was so small that the resonant frequency was outside the frequency sweep previously performed. Therefore, the connection between the capacitor and the antenna was broken to measure only the resonance of the antenna which resulted in no antenna resonance. At this point it was determined that the skin depth might be an issue. Base on these experiments and skin depth calculations, it was concluded that the metal film had to be thickened to 10 micrometers if possible. The hypothesis here was that, maybe plating the ground plane with copper tape introduces losses; we believed that the reason was that when the ground plane was covered with copper tape, the electric field must first penetrate the lossy layer and the tape might not be making good contact with the ground plane. This led us to the development of a new approach with thicker films using an electroplating technique, to increase the thickness of the interdigital capacitor, antenna and ground in order to bypass the copper tape.



## 6.2 Thick-film capacitor: analysis and results

Capacitance measurements were performed on one thick-film sensor since interdigital electrodes of the second thick film sensor were shorted. This was corroborated by conductivity measurements. Once again, the measurements were performed by means of a capacitance meter with using a similar setup to the thin-film measurements. The ceramic beam was clamped at the narrower end while bending it at the wider end, introducing 800  $\mu$ strain for every 2 cm that the ceramic beam was bent.

The result of the capacitance measurement for the thick-film capacitor as a function of strain is as follows:

Table 6.2 Capacitance measurements of thick-film capacitor

Antenna length (mm)	Unstrained (base cap pF)	Strained (800 $\mu$ s) pF	$\Delta C$ (pF)	Gage Factor (G= $\Delta C/C \cdot 1/\text{strain}$ )
10	0.90	0.91	0.01	13.8

The thick-film capacitor was designed to have a base capacitance of about 0.85 pF, and the fabricated thick film sensor had a capacitance of 0.90 pF. The resulting gage factor of the fabricated sensor was approximately 14, slightly higher than the gage factor of 12 obtained with the simulation. The fabrication of the thick-film capacitor was easier than the thin film because both the thickness of the dielectric (kapton tape) and the thickness of the film were well controlled. Thus, the fabricated sensor had very similar parameters to the ones used for simulation.

Once again, the only accurate way to measure the resonant frequency of the sensor is to connect a test cable (2 connections: antenna element and ground) or by using a

diode to differentiate the input signal from the output signal by a doubling effect when using an RF pulse of energy.

High frequency measurements showed at resonant frequency of 2.4 GHz under normal condition, i.e. unstrained condition. The targeted resonant frequency was 2.6 GHz when using a 10 mm-long antenna. The fabricated sensor had a smaller resonant frequency, possible due to its slightly higher capacitance. The higher the capacitance for a given antenna length, the smaller the resonant frequency. When a strain of 800  $\mu$ strain was applied, a shift of 7 MHz was observed. This change in the resonant frequency yielded a gage factor of 3.64, as opposed to a gage factor of 4.5 from the simulator. The hypothesis for this smaller gage factor was attributed to dielectric (kapton tape) not adequately transferring the strain to the sensor.

These small gage factors led us to develop a totally different approach in order to boost the sensitivity of the strain gage. The design of free standing structures such as the buckled beam capacitor or the antenna strain gage, were the result of the pursuit for better resolution and a larger shift in the resonant frequency.

### **6.3 Buckled beam capacitor: analysis and results**

To obtain a better understanding of the original buckled beam capacitor concept, a buckled beam sensor was analyzed as a 6-component circuit. Figure 6.1 shows the physical layout of the buckled beam capacitor and associated components that form the complete structure.

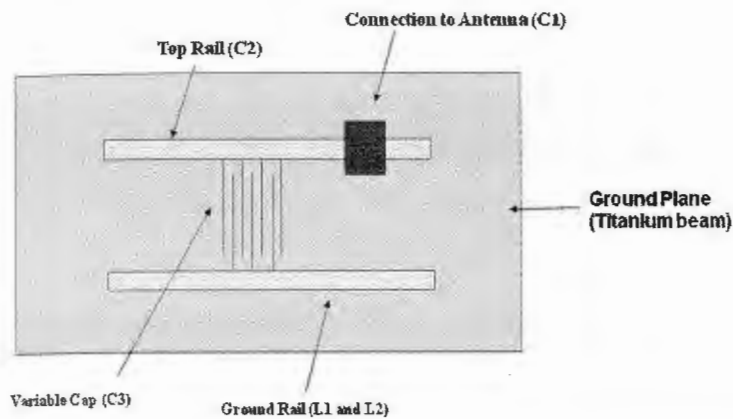


Figure 6.1 Physical sketch of buckled beam capacitor; circuit components

A circuit model was obtained from the physical model shown in Figure 6.2. In the circuit model, a fixed inductor was incorporated in place of the antenna. Ideally, the inductor forms a series resonant circuit with the variable interdigital capacitor (C3). The frequency of resonance enabled an accurate determination of C3 and the  $\Delta C$  due to flexing the beam.

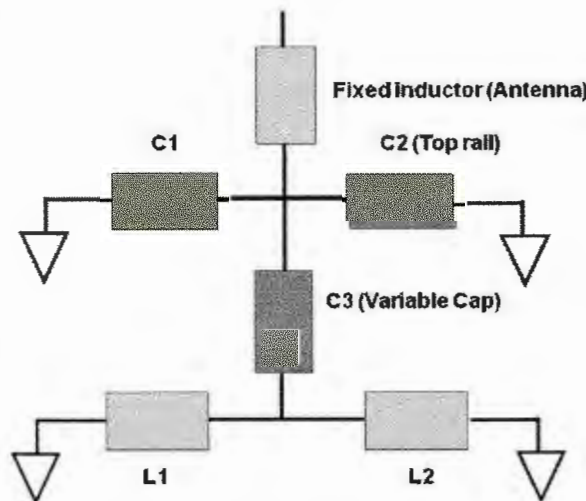


Figure 6.2 Circuit model of buckled beam capacitor

The calculated component values are as follows:

Table 6.3 Buckled beam capacitor: component values

Component	C1 (pF)	C2 (pF)	C3 (pF)	L1 (nH)	L2 (nH)
Value	0.75	1.5	0.5	1	1

C1 and C2 dominated the resonant circuit and prevented the small change in C3 from shifting the resonant frequency since the capacitors appear in parallel with the variable interdigitated capacitor C3. L1 and L2 tune the resonant frequency but did not reduce the shift in magnitude of the resonant frequency. Therefore, the problem with this circuit was the parasitic capacitances (C1 and C2) created by the non-conductive epoxy that attached the top rail to the ground plane.

On the other hand, the circuit model matched the measurements well. A 10 nH inductor was connected to the top rail of the buckled beam capacitor. The resulting LC network was measured as a shunt resonant circuit, shown in Figure 6.3.

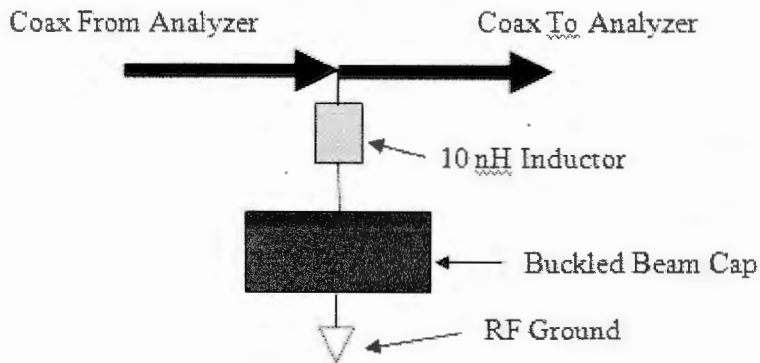


Figure 6.3 Setup for measurements of buckled beam capacitor

The resonance of the first buckled beam capacitor design was found approximately 880 MHz. When 800  $\mu$ strain was applied to the titanium beam, a very

small shift was measured (6 MHz), for a gage factor of 8.5 as compared to the expected gage factor of 60. Also, the resonance of the buckled beam capacitor was very low because of the large parasitic capacitances C1 and C2, which also degrade the gage factor since the contribution to the shift in frequency is largely due to the variable interdigital capacitor C3.

This provided motivation to modify the design to decrease the parasitic capacitances. As discussed in Appendix E, the thickness of the dielectric (kapton tape) was increased to 200  $\mu\text{m}$  and the length of the top rail was decreased in the second design by increasing the number of fingers from 16 to 60 for the third buckled beam design.

### **6.3.1 Second buckled beam cap design: shorter top rail**

The setup shown in Figure 6.3 was used to test the modified design of buckled beam capacitor. The nominal capacitance and  $\Delta C$  was measured by flexing the beam. A strong resonance at 1.503 GHz and a shift in the resonance of 1.565 MHz with 2 cm of deflection were obtained for an applied strain of 800  $\mu\text{strain}$ . This yielded a gage factor of 51, very close to the design value of 60. A shift in frequency of about 4.1% was both repeatable and stable. The calculated parasitic capacitance from the short (top rail) and the non-conductive epoxy was about 0.29 pF in total (C1 + C2). Adding the parasitic capacitance to the nominal capacitance from the interdigital capacitor (C3) gave a total capacitance of 0.66 pF. This compared favorably to the expected base capacitance of 0.62 pF. The deflected beam lowered the buckled-beam capacitor to 0.57 pF. The change in the buckled-beam capacitor is about 15% so the total circuit response was affected to some degree by the parasitic capacitance.



Lowering the parasitic capacitance further was difficult since the third buckled beam design included more wires which increased the base capacitance C3.

### **6.3.2 Third buckled beam capacitor design**

The best results to date were achieved with the third buckled beam capacitor design. This design included 60 interdigital wires to form the capacitor, a 200  $\mu\text{m}$  dielectric, a bottom rail that was laser-welded to the titanium beam and a smaller volume of non-conductive epoxy to keep the parasitic capacitance low.

The buckled beam capacitor design appeared to have about 1.8 pF of capacitance. This was the total capacitance between the wires and the capacitance to ground from the top rail and the non-conductive epoxy. The targeted capacitance was 1.42 pF, so the actual capacitance of the fabricated buckled beam capacitor was close to that of the original design. The contribution of the parasitic capacitances was approximately 40 pF. The resonant frequency was 953 MHz with a 10 nH inductor as shown in Figure 6.4. This resonance was expected due to the large total capacitance for this design.



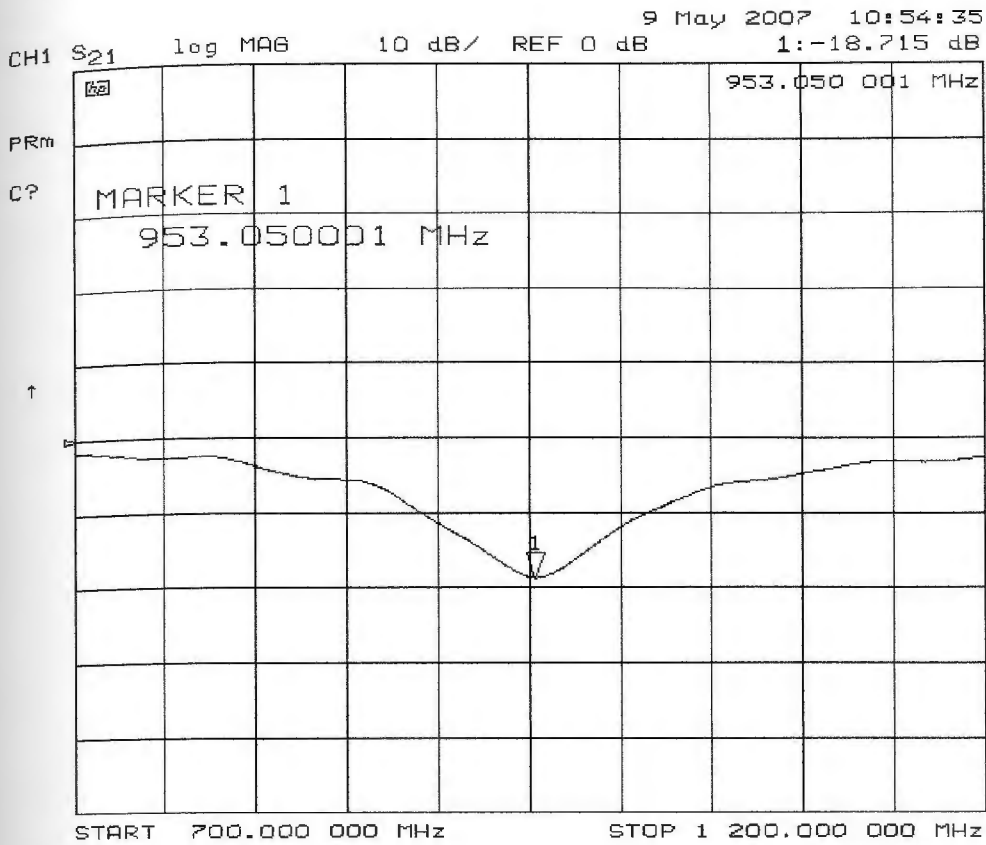


Figure 6.4 Resonance of third buckled beam capacitor design; no beam deflection

Bending the titanium beam approximately 10 mm (400  $\mu$ strain) moved the resonance to about 975 MHz (See Figure 6.5). This represents a shift in frequency of 22 MHz, and resulted in a gage factor of 57. This was the largest gage factor achieved of all the approaches used to date. This is a 2.2% change in the resonant frequency.

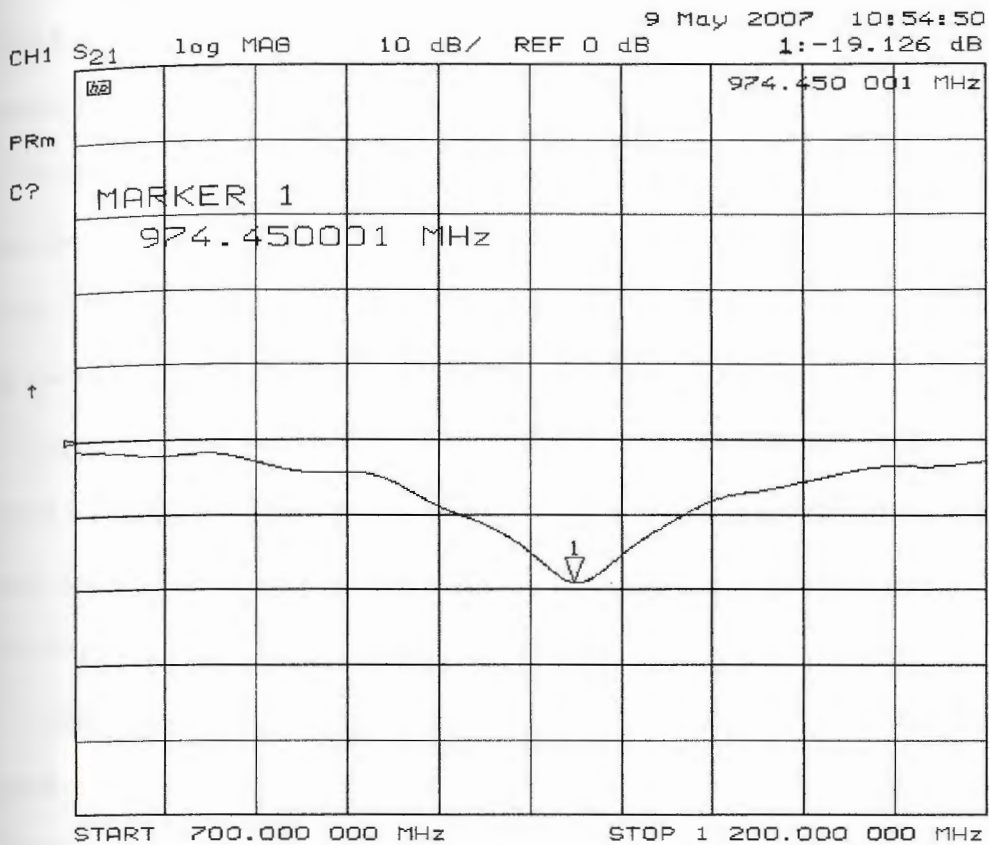


Figure 6.5 Resonance of third buckled beam capacitor design; 400  $\mu$ train

#### 6.4 Antenna strain gage: analysis and results

A test fixture was put together to generate the fundamental excitation for the antenna strain gage prototypes. As mentioned in the antenna gage design section, it was expected that the resonant frequency would be around 3 GHz. Adjustments to the filters, amplifiers and Tx/Rx antenna were necessary since the original setup was tuned for a lower frequency of operation.

The initial configuration using a 16-mm long antenna was illuminated from 1 to 3.6 GHz but the second harmonic produced by the diode could not be found. It was possible that the antenna resonance was higher than 3.6 GHz, which was the highest frequency attainable by the test fixture and capable to generate enough RF power. The

other hypothesis was that the diode might have not been working or that its response wouldn't be good enough to generate a second harmonic.

Further analysis using a test cable on the antenna showed that its efficiency was only about 4%. With the diode connected, the second harmonic was also not possible to see, even knowing where to look around 6 GHz. The low efficiency was caused by the low conductivity of the ground plane which was made of titanium.

One idea to get around this problem and still being able to use the titanium strain beams was to lengthen the antenna to move its resonance to the 2.4 GHz band. In this band, higher power amplifiers were available, so more power could be use to illuminate the antenna.

Therefore, the design was changed as mentioned in Chapter 4, increasing the length of the antenna to 27 mm and putting a solderable wire instead of the fabricated (chip) diode to measure the frequency of resonance of the modified design. A second prototype included a chip diode on the antenna.

The frequency of resonance measured in the modified prototype was exactly where it should be, around 2.44 GHz, measured by attaching a test cable to the solderable wire. The resonance moved about 360 MHz to 2.8 GHz with just 3 mm of deflection of the beam, i.e. 120  $\mu$ strain. Therefore, the estimated gage factor for this prototype was 1229, the largest gage factor seen during this investigation by far.

Figure 6.6 and figure 6.7 show the frequency of resonance of the antenna gage with solderable wire with no strain induced and when it was flexed 3 mm.

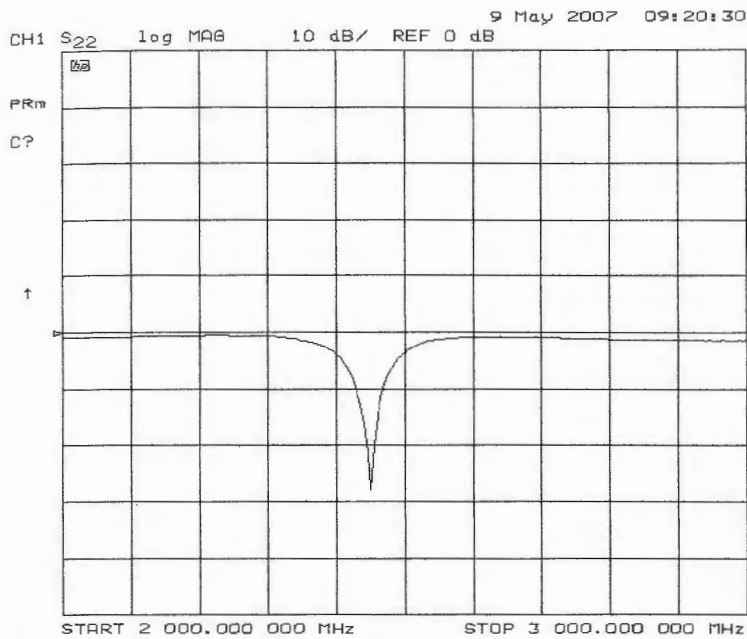


Figure 6.6 Resonance of antenna gage with solderable wire (no strain)

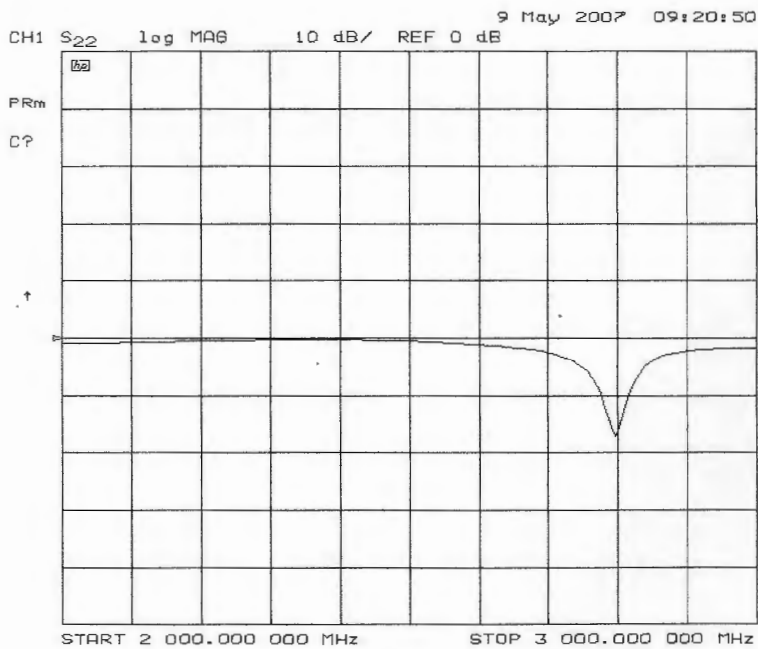


Figure 6.7 Resonance of antenna gage with solderable wire bent 3mm

See Appendix H for a plot of the shift in frequency vs the amount of deflection.



The second prototype fabricated with a 27-mm antenna and a chip diode included showed no second harmonic visible from 4.7 to 5.2 GHz. Thus, and external diode was attached to the antenna wire. This time a large second harmonic was visible at 4.99 GHz. Two millimeters of deflection, i.e. 80  $\mu$ strain, moved the second harmonic up to about 5.32 GHz. So, the antenna gage was working only with an external diode, not with the chip diode made of a silica slab. Either the diode was not good enough at RF or the connection to ground planes was still weak, even though a copper tape was used between the diode and ground plane. Two spectrum plots are shown in figure 6.8 and figure 6.9. The input to the spectrum analyzer was connected to the Rx antenna, i.e. a wideband horn, through two high-pass filters and a preamp. The Tx signal was manually stepped thru the band of interest, at the fundamental frequency and the spectrum analyzer was set for "Max Hold" in a 200 MHz band around the second harmonic of the fundamental frequency. The peak response was held on the screen.

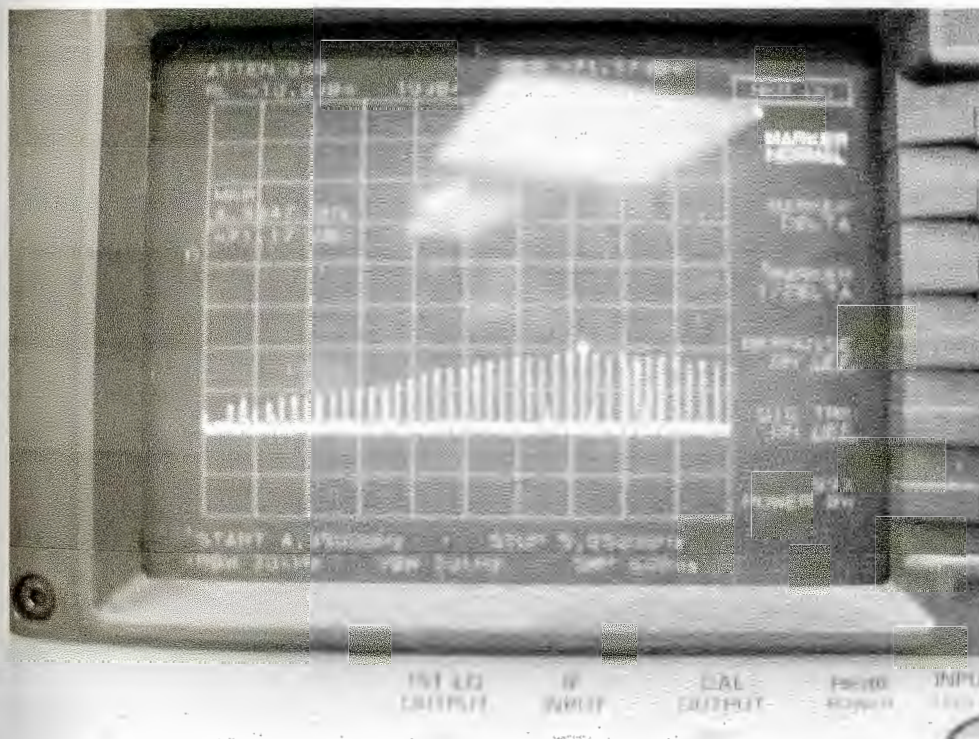


Figure 6.8 Second harmonic response - no beam deflection

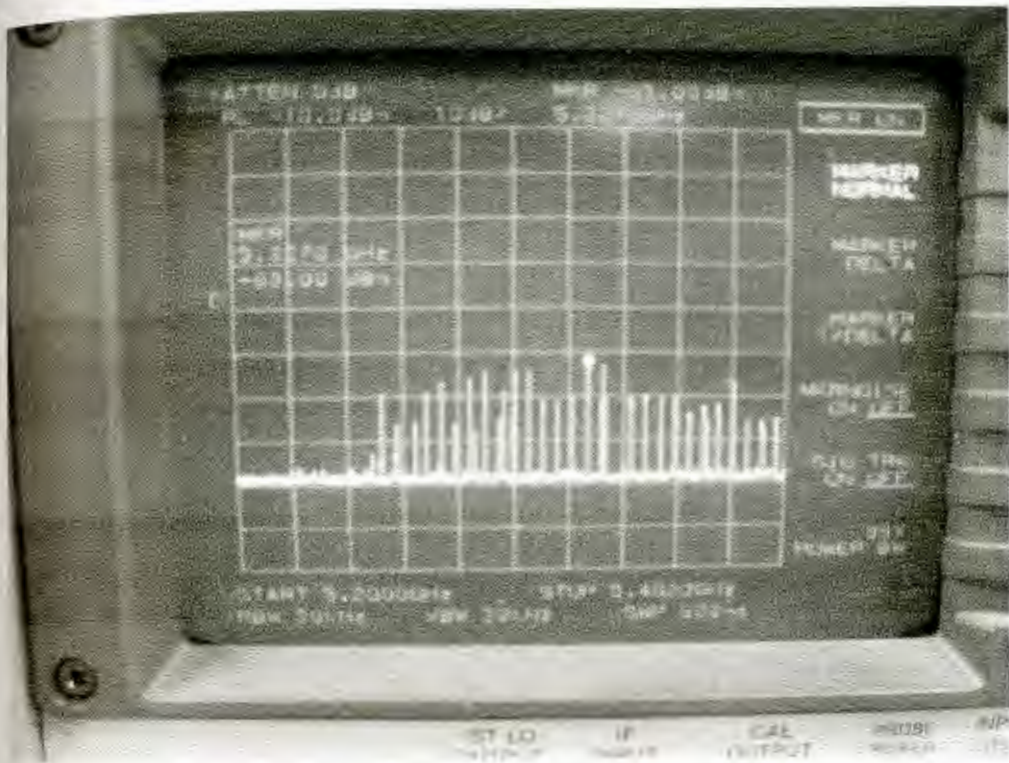


Figure 6.9 Second harmonic response – 2 mm deflection

Some additional details of these measurements are shown in Appendix I.



## CHAPTER 7 Conclusions

Strain measurements on compressor blades of jet engines are currently performed through wire strain gages routed to the acquisition system through a slip-ring assembly. However, slip ring systems tend to wear off, especially the brush/ring contacts which make the signal noisy. This performance degradation leads to high maintenance costs in addition to the high cost of installing slip-ring systems. Therefore, there is the need to develop non-contact systems to measure strain on compressor of jet engines. This thesis described the research work performed during the last year and a half to develop a prototype of a passive RF transponder that works as a wireless strain gage for gas turbine engines. The design, simulation, fabrication and testing of several prototypes have been described in the content of this thesis. The signal processing concept to be employed by the wireless strain gage system was beyond the scope of this research work. The passive transponder prototype needed to be printed, welded or deposited directly onto compressor blades; thus several key issues had to be addressed during the design of the transponder. Among these issues are the thickness of the transponder, the footprint and weight of the sensor and the large "g" loading experienced by the blades.

The proposed wireless strain gage concept uses a shift in the frequency of the resonance of a capacitive/inductive transponder or antenna wire over a ground plane, to measure strain. The principle of operation of all the approaches explored by this investigation is the same: a pulse of energy within a shot frequency band is transmitted to the transponder which, depending on the surface strain, returns a signal with a different resonant frequency. A change in the capacitance or in the distance between the antenna wire and ground introduced by strain, changes the frequency; thus a gage factor can be calculated.

Four different approaches were used to develop a prototype with the largest gage factor possible. Initially, thin-film and thick-film capacitors were designed, simulated, fabricated and tested to determine the maximum possible change in capacitance using such planar structures. Thin-film capacitors were developed by photolithography and sputtering processes. Simulations showed that the interdigital capacitor was a resonant circuit itself, but its resonance was above the frequency of operation required by the signal processing module. Therefore, an antenna element was added to move the frequency of resonance to the 1 to 2 GHz range. Measurements were performed at DC using a capacitance meter and a gage factor of 14 was observed in terms of capacitance. It was expected that the gage factor in terms of frequency would be lower since only the capacitance change would contribute to the change in resonant frequency; thus, the gage factor expected for the thin-film capacitor was around 5. Unfortunately, the skin depth of the thin-film capacitors was too thin to so the transponder was not able to operate in the 1-2 GHz range. No resonance was detected when high frequency measurements were performed. Therefore, a thick-film capacitor was developed to address the skin effect issue.

It was expected that the thick-film capacitors would yield very similar gage factors, and when tested at DC, a gage factor of 4 and 11 were obtained in terms of resonant frequency and capacitance respectively. Since the thick-film capacitors required a thicker dielectric, the capacitance decreased, increasing the frequency of resonance of the transponder; therefore, longer inductive elements were required to decrease the frequency of operation. High frequency tests showed only a 7-MHz frequency shift out of a base resonance of 2.4 GHz, for a gage factor of about 3.7. This was probably due to the fact that a thicker dielectric was not correctly transferring strain from the surface of the substrate.

A third approach using a buckled beam amplification scheme combined with a capacitor made of interdigital wires yielded gage factors as large as 57. Parasitic capacitances introduced in the sensor during fabrication reduced the gage factor; the only contribution to a change in resonant frequency came from the variable interdigital capacitor and not from the parasitic capacitances. A laser-welding technique to attach the buckled beam capacitor to the titanium strain beam minimized the parasitic capacitances and boosted the gage factor close to 60.

The last approach explored was the antenna strain gage design. This prototype correlated the change in the distance from the antenna to the ground due to strain, to a change in the tuning frequency of the antenna. Very large gage factors of around 1000 were observed with this approach. Although, this approach had two main issues: first, the length of the antenna was about 27 mm which means that strain is measured over the entire length of the antenna; and second, the chip diode placed on the antenna did not work as expected. An external diode was needed to perform RF measurements.

In summary, this research examined four different prototypes for the wireless strain gage concept, two of them using thin-film and thick-films and two more using free standing structures. It has been shown that the free standing structures yielded larger gage factors compared to the thin-film and thick-film capacitors. This is due to the fact that the free standing structures are only in contact with the substrate at one or two places and not over the whole structure. Therefore, if a large gage factor is what is needed by the signal processing system, the free standing approach is the best. On the other hand, thin-film and thick-film structures can be more easily fabricated than free standing structures, besides the fact that they can probably withstand the large "g" loading better.

## **CHAPTER 8 Future work**

### **8.1 Temperature compensation**

All the designs proposed by this research did not address an important factor such as the effect of temperature on the measurements. For the thin-film and thick-film capacitors, temperature becomes an issue; first, because the dielectric might not withstand high temperatures, but more importantly, the dielectric constant can vary as temperature changes. Therefore, a temperature compensation scheme is needed. One approach that can be used to compensate the temperature effect is the use of dielectrics, where the dielectric constant remains fairly constant for different temperatures or the combination of two dielectrics with opposite dielectric constant behavior so the net effect cancels out the temperature effect.

Another approach is the use of two different resonant elements. The temperature effect would affect the resonant frequency of both capacitors and antennas, but if the two signals are combined to obtain the difference in frequency, again the temperature effect is cancelled since what has been measured is not the individual resonant frequencies but the net resonant frequency difference. Figure 8.1 shows a sketch of an envisioned antenna gage with a second antenna for temperature compensation.



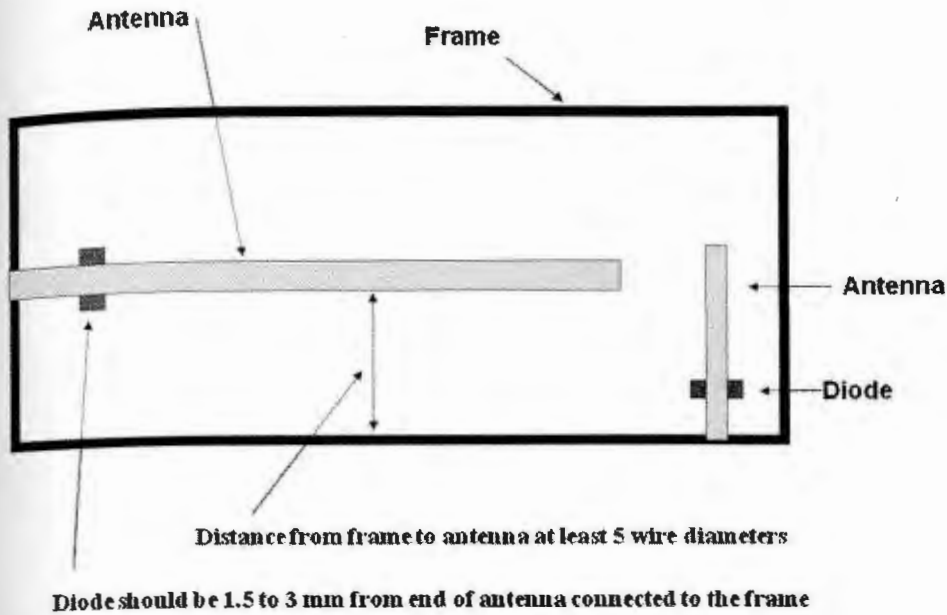


Figure 8.1 Antenna gage with temperature compensation approach

## 8.2 Dynamic testing

Throughout this investigation, all testing was performed with the strain beams stationary; this is that the substrates were not rotating, while the measurements were performed. Ultimately, if the prototypes developed in this thesis are to be modified and improved for rotating blades, dynamic tests need to be performed. With a dynamic testing scheme, the signal processing issues can be addressed since the antenna of the sensor only passes the Tx antenna in an instant of time. A dynamic testing approach needs to determine the amount of strain that is introduced on the strain beam.

A schematic of the proposed dynamic testing scheme is shown in figure 8.2

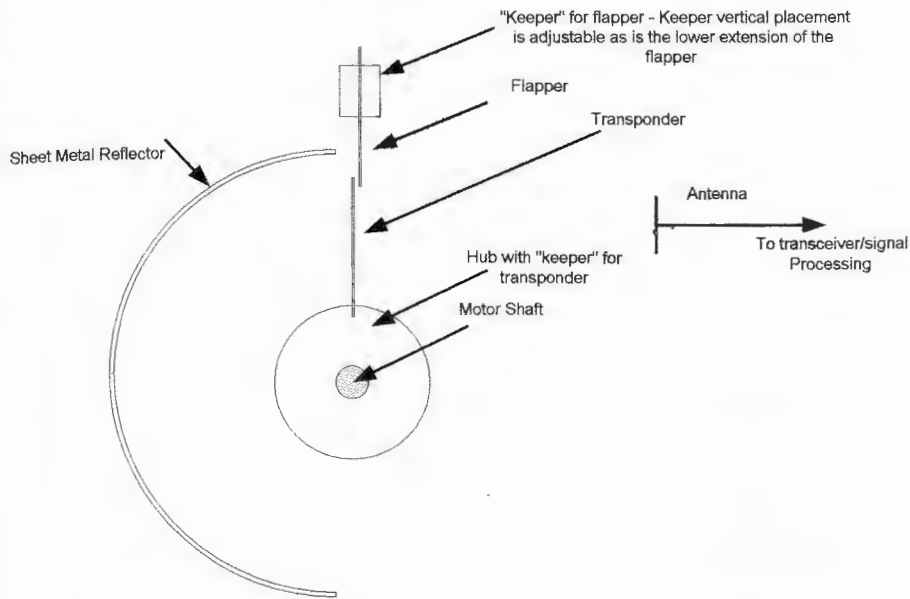


Figure 8.2 Dynamic test setup for RF strain measurements

The figure above shows a motor shaft could be use to spin the fabricated prototype. A flapper made of teflon would snap the transponder introducing certain amount of strain still to be investigated. An actual prototype for the dynamic test has been built and it is show in figure 8.3.

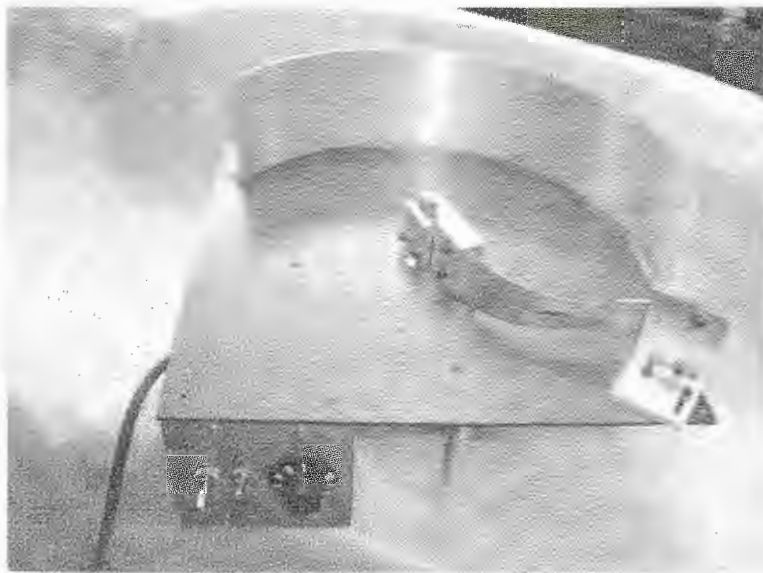


Figure 8.3 Prototype for dynamic testing



## APPENDIX A SAW resonator design

The lumped equivalent circuit of the SAW resonator near resonance is shown in the following figure.

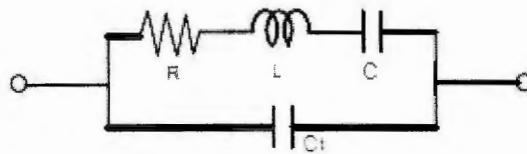


Figure A.1 Lumped equivalent circuit of a SAW resonator

The input admittance of the IDT appears like a series resonant circuit in parallel with the transducer capacitance  $C_T$ . The capacitance  $C_T$  contributes to the major part of the reactance. The impedance  $Z(f)$  is then given by:

$$\begin{aligned} Z(f) &= [G_a(f) + jB_a(f) + j2\pi C_T]^{-1} \\ &= R_a(f) + jX_a(f) + (j2\pi C_T)^{-1} \end{aligned} \quad (\text{A1})$$

where  $G_a(f)$  and  $B_a(f)$  are the conductance and susceptance, and  $R_a(f)$  and  $X_a(f)$  are the resistance and the reactance respectively.

From the crossed-field model (Morgan 1976),  $G_a(f)$  and  $B_a(f)$  are given by:

$$G_a(f) = 2f_0 C_s k^2 \left( \tan \frac{\theta}{4} \sin \frac{N\theta}{2} \right)^2 \quad (\text{A2})$$

$$B_a(f) = f_0 C_s k^2 \tan \frac{\theta}{4} \left( 4N + \tan \frac{\theta}{4} \sin N\theta \right)^2 \quad (\text{A3})$$

where  $\theta = 2\pi f / f_0$

$f_0$  is the resonant frequency

$C_s$  is the static capacitance per section of the IDT in  $pF/m$

$k^2$  is the piezoelectric coupling factor of the substrate

$N$  is the number of sections of the IDT

$G_a(f)$  has a maximum at  $f = f_0$  given by:

$$G_a(f_0) = \left( \frac{4k^2 N}{\pi} \right) 2\pi f_0 C_T \quad (A4)$$

where  $C_T = NC_s W$

$W$  is the aperture or length of the fingers of the IDT in meters

According to Farnell et al. (1970), the capacitance per meter of a finger length is given by:

$$C_s = K(\epsilon_o + 1) \quad (A5)$$

where  $C_s$  is in  $(pF/m)$ ,  $\epsilon_o$  is the dielectric constant of the substrate and  $K$  as a empirical value given by

$$K = 6.5 \left( \frac{D}{L} \right)^2 + 1.08 \left( \frac{D}{L} \right) + 2.37 \quad (A6)$$

Figure A.2 shows the line width of the fingers ( $D$ ) and the electrode section ( $L/2$ ) which is half of the periodicity of the IDT when the line width and the spacing is the same.

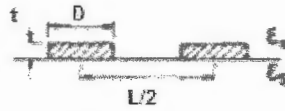


Figure A.2 Cross-section of an electrode section

The following equations from Morgan (1976) correspond to the series combination of  $R, L, C$

$$R = \frac{2k^2}{\pi^2 f_0 C_s} = \frac{G_a(f_0)}{(2\pi f_0 C_T)^2} \quad (\text{A.7})$$

$$C = \frac{1}{4\pi^2 f_0^2 L} \quad (\text{A.8})$$

$$L = \frac{l_c}{\lambda} \frac{1}{(4f_0 G_a(f_0))} \quad (\text{A.9})$$

where  $l_c$  is the effective cavity length (distance from closest reflector on the left of IDT to closest reflector on the right of IDT).

Based on equations A.1 thru A.9, the design parameters proposed were as follows:

Finger line width ( $D$ ):	25 $\mu\text{m}$
Spacing between fingers( $S$ ):	25 $\mu\text{m}$
Number of IDT sections ( $N$ ):	12
Number of total fingers:	25

Aperture of fingers ( $W$ ):	2.5 mm
Number of reflectors:	50
Effective cavity length ( $l_e$ ):	2.5 mm
Metal thickness:	1000 Å
Coupling factor ( $k^2$ ):	0.14

The periodicity of the IDT will be  $100 \mu\text{m}$  ( $2S+2D$ ), therefore the resonant frequency expected is  $f_0 = \frac{2250\text{m/s}}{100E - 6m} = 22.5\text{MHz}$

The value of the elements of the lumped equivalent circuit is as follows:

$$R = 1.297 \text{ k}\Omega$$

$$L = 4.0289 \text{ mH}$$

$$C = 12.4499 \text{ Ff}$$

$$C_s = 54.43 \text{ pf/m}$$

$$C_T = 1.6326 \text{ pF}$$

$$G_a(f_0) = 6.911775\text{E-}5 \text{ mhos}$$

## APPENDIX B Design and simulations of thin-film interdigital capacitor

### Simulation results for interdigital capacitor design 1 and design 2

Figure B.1 and B.2 show the plots obtained from the simulation using Sonnet Lite.

These simulations show the capacitance values included in Table 3.2

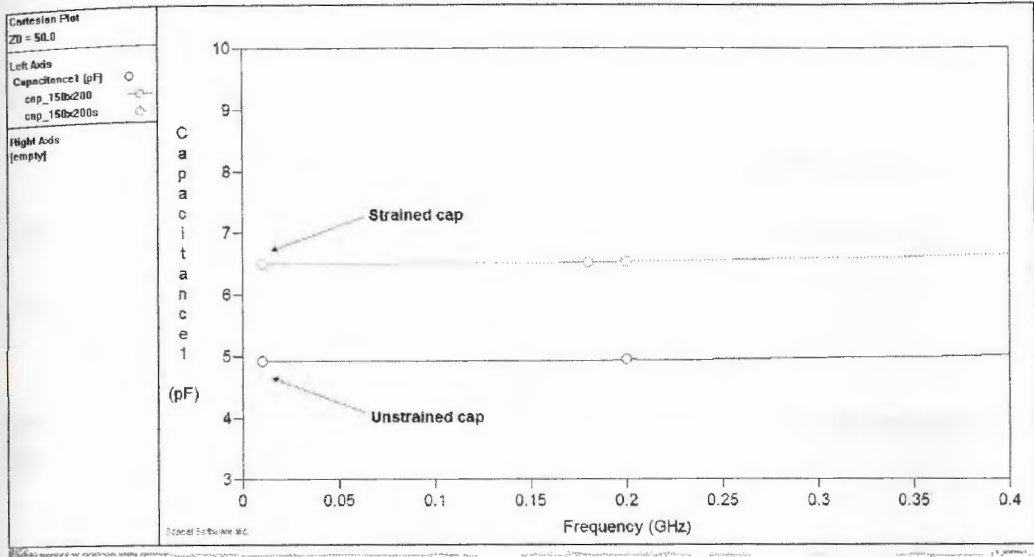


Figure B.1 Strained and unstrained capacitance values for design 1

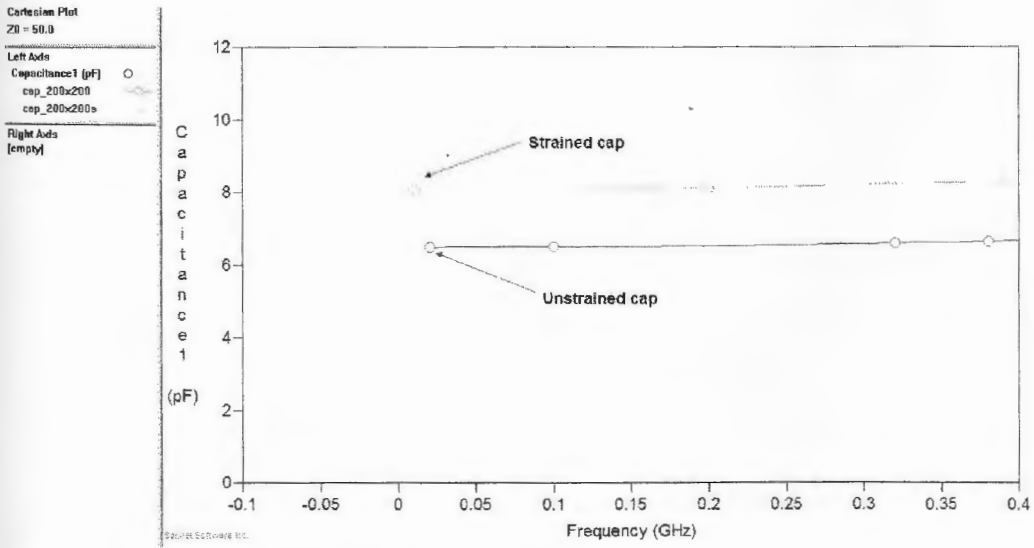


Figure B.2 Strained and unstrained capacitance values for design 2



As mentioned in Chapter 3, although the change in capacitance for design 1 and 2 is the same, the base capacitance of the first design is smaller with a similar induced strain, which makes the gage factor larger compared to design 2.

### Visual representation of design 1 parameters

The following figures show a 3D dimensional view of the proposed interdigital capacitor design, as well as the top and bottom layers that form the electrodes of the capacitor.

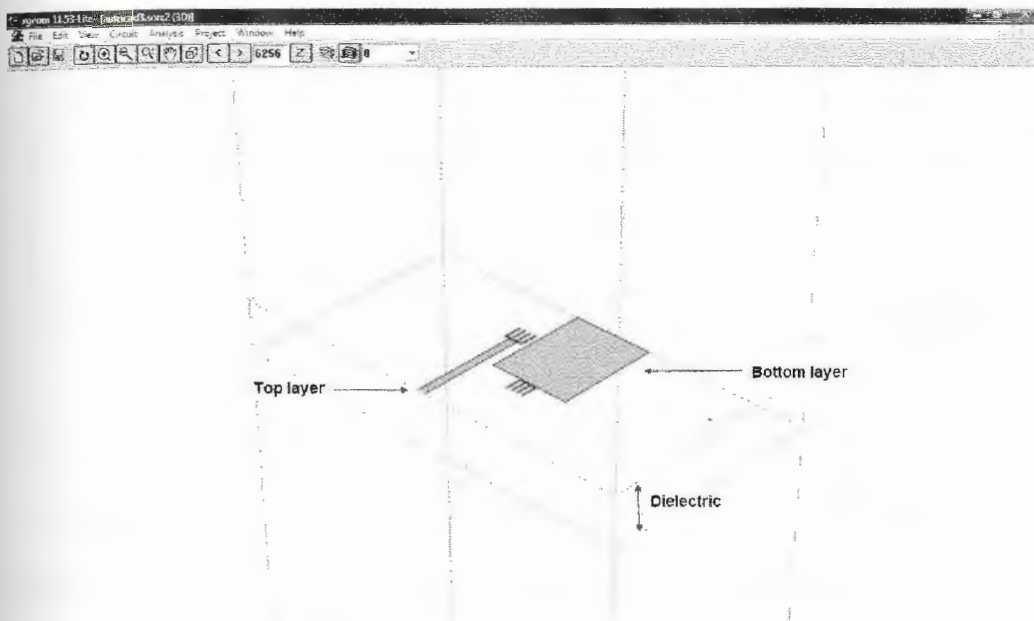


Figure B.3 3D view of interdigital capacitor

It must be noted that the dimensions shown in Figure B.3 are not to scale. That is why the dielectric layer looks more than the  $8\ \mu\text{m}$  specified by the design parameters. Additionally, for simulation purposes, a larger layer of air was left on top and below

the planar structure. The reason for this is that the simulator sees every side of the virtual (transparent) box as a ground plane and it is important to keep the planar structure as far as possible from the walls.

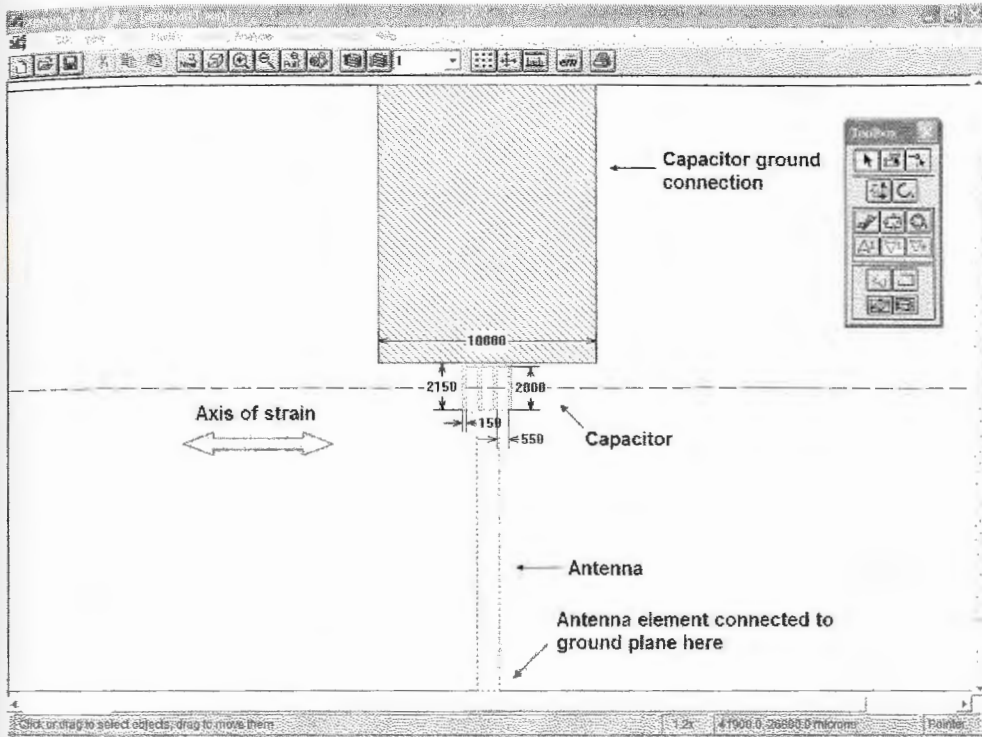


Figure B.4 Bottom layer of interdigital capacitor

Figure B.4 shows the bottom layer of the interdigital capacitor. It must be noted that the interdigital fingers (shown in green in figure above) are connected to ground through a large piece of metal (shown in red in figure above). In practice, this piece of metal will physically ground one side of the interdigital capacitor. As it will be discussed in Chapter 5, the interdigital capacitor is deposited on a ceramic constant strain beam, which is coated with a thin film of metal on the back to simulate a

ground plane. Therefore, the bottom layer is connected to ground by shorting the large piece of metal through the edge of the strain beam.

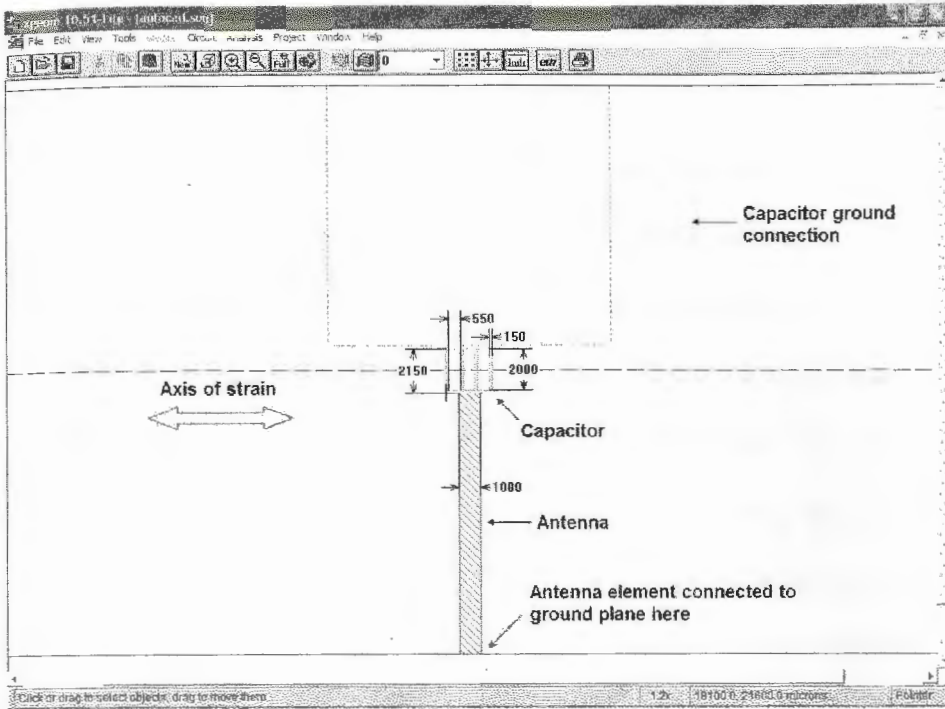


Figure B.5 Top layer of interdigital capacitor

Figure B.5 shows the top layer of the interdigital capacitor. It must be noted that the interdigital fingers (shown in green in figure above) are connected to an antenna element (shown in red in figure above). The antenna will shift the resonant frequency to the desired frequency of operation.

## APPENDIX C Sputtering procedure

The following steps were used to deposit the different metal thin films. Prior to sputtering a background pressure between  $4.9 \times 10^{-6}$  Torr and  $6.5 \times 10^{-6}$  Torr was desired.

Argon gas was introduced into the high pressure chamber after the throttle valve was closed and the Argon gas was introduced. The Argon introduced into the chamber was also monitored with the Pirani gage on the sputtering machine.

The RF power level was increased and the reflected power must be kept close to zero using load and target tuning features. The tuners should be adjusted until a stable plasma was reached, keeping the reflected power close to zero. Once again, Argon gas was decreased to 5-7 mTorr and the RF power level increased to the desired value.

The surface of the metal targets is etched for 15 minutes before sputtering. Then the sample is rotated to the desired position underneath the target. The sputtering process time depends on the thickness of the metal desired.

After sputtering is complete, wait for 30 minutes until targets and substrate holder cools and the chamber is vented.

To vent the chamber, make sure ionization gage is closed, close Cryo Pump (HI VAC button), open tank and open vent knob, let the chamber reach  $7.6 \times 10^2$  Torr. And finally pull up chamber.

To pressurize back the chamber, pull down the chamber and close vent knob, hit Rough Pump. Every other pump should be closed and bring the chamber to  $1 \times 10^2$  Torr. Once the chamber reaches this pressure, close Rough Pump and Open Cryo Pump, switch on Pirani gage.

## APPENDIX D Fabricated thin-film and thick-film capacitors

### Additional thin film capacitors

Figures D.1 and D.2 show two additional thin-film capacitors that were fabricated following the procedure described in Chapter 5. As shown in Figure D.1, the narrower part of the ceramic strain beam broke during testing due to excessive stress applied to the strain beam.

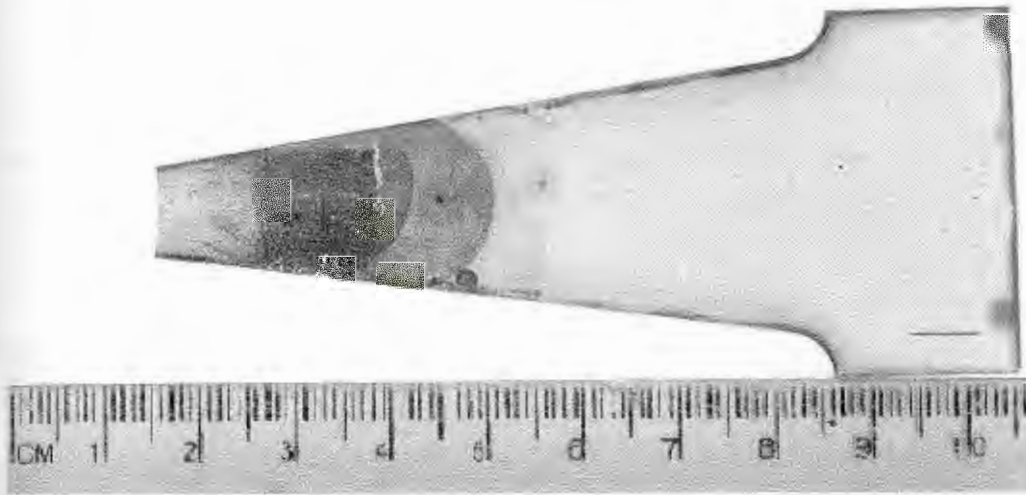


Figure D.1 Second fabricated thin-film capacitor on ceramic beam: 6mm

The fabricated thin film-capacitor shown in the previous figure shows a lot more bubbles developed not only in the lower edge of the substrate but also close to the interdigitated fingers of the capacitor. It is believed that the reason for this was that the temperature of the ceramic substrate reached 250 °C in less than 25 minutes previously specified.

Another important detail during the fabrication process was the fact that once the bottom metal layer was deposited, at least the edge of this layer had to be protected before spin-casting LOR 50B for the dielectric layer. The reason for this is that for



capacitance measurements, access to the top and bottom metal layers is needed. Therefore, if LOR 50B is deposited on the entire surface without protecting the bottom metal layer, this layer gets buried underneath the dielectric and measurements are not possible. A small strip of uncovered metal can be seen on the top edge of the ceramic beam in the sensor area in Figure 5.3 and Figure D.1. This area was protected when depositing the dielectric material so a clear access to the bottom electrode was achieved

Figure D.2 shows the third and last thin-film capacitor fabricated. In terms of quality, this last prototype had a clearer pattern, since almost no bubbles developed on the surface of the substrate, achieving a smoother surface to deposit the metal film for the top electrode.

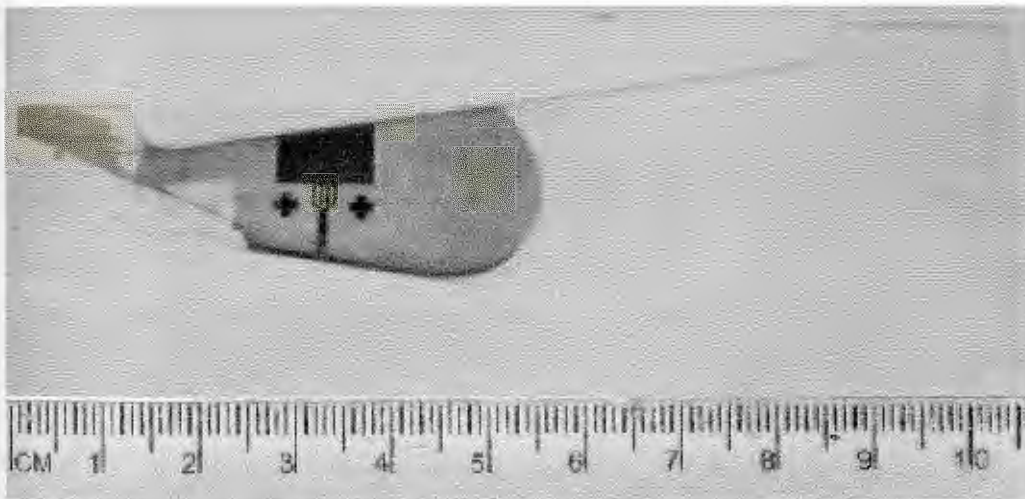


Figure D.2 Third fabricated thin film capacitor on ceramic beam: 6 mm

A final comment on the fabrication of this type of capacitors is that before sputtering the back of the ceramic strain beams for the ground plane, measurements and testing had to be performed on the capacitors. This is because once the back of

the strain beam was sputtered with copper, the bottom and top electrodes are connected to ground and it is technically impossible to measure the capacitance of the interdigital electrodes since they are shorted.

### **Additional thick film capacitors**

Following the same procedure described in Chapter 5, a second thick-film capacitor was fabricated with a faster deposition rate. This time, the deposition rate was  $5\mu\text{m}/\text{minute}$ , applying an electric current of 350 mA for 2 minutes. Figure D.3 shows the fabricated capacitor. It can be seen that the shape of the antenna was deformed as well as the shape of the interdigital fingers.

DC measurements were not possible on this capacitor because the top and bottom metal layer were shorted out after electroplating.

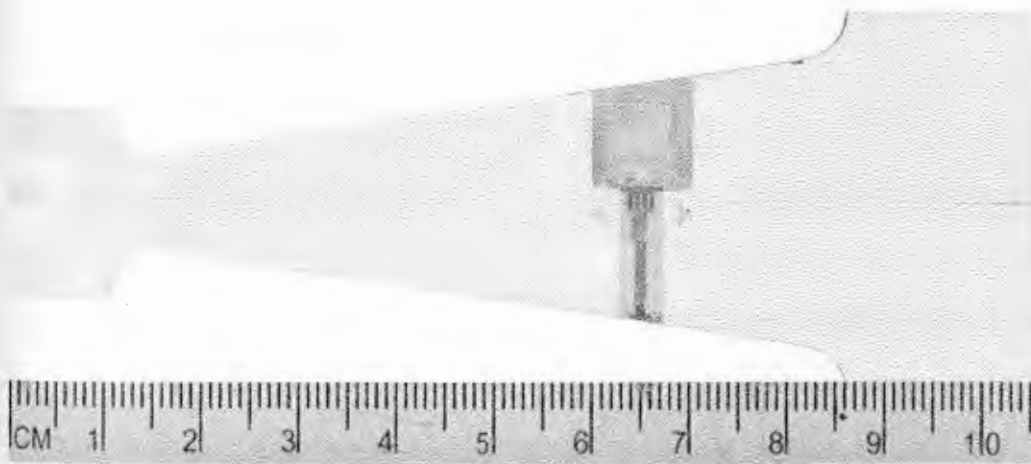


Figure D.3 Additional fabricated thick-film capacitor; antenna length: 10mm

## APPENDIX E Additional buckled beam capacitor designs

Some issues arose after the initial buckled beam was fabricated and tested, as described in Chapter 5 and further analyzed in Chapter 6. The biggest concerns with the buckled beam capacitor were the parasitic capacitances created when attaching the non-grounded electrode (top buckled rail) to the titanium beam; and the fact that the large globs of silver epoxy were preventing the grounded electrode (bottom buckled rail) from achieving the maximum displacement; thus decreasing the mechanical amplification which leads to a smaller  $\Delta C/C$ . Therefore, several observations to the initial fabricated buckled beam capacitor were made and some modifications were scheduled for the next designs. Figure E.1 shows a close-up of the buckled beam capacitor

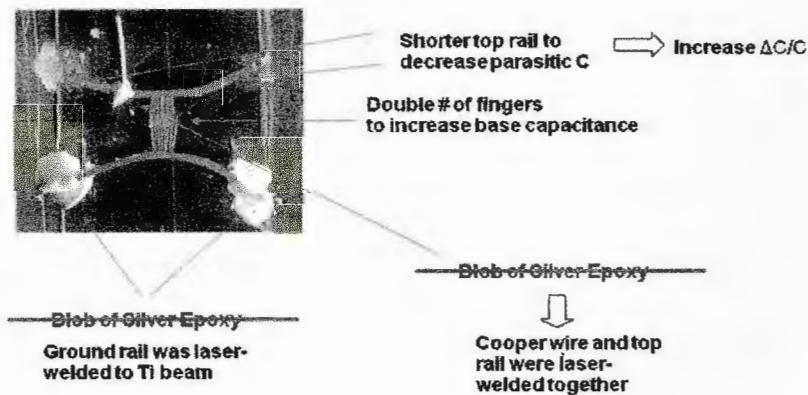


Figure E.1 Buckled beam capacitor close-up and proposed modifications

The previous figure shows the large globs of non-conductive and silver epoxy developed after small drops were put in place to hold the buckled rails to the titanium beam. The non-conductive epoxy globs create some parasitic capacitances ( $C_1$  and  $C_2$  as shown in Figure E.2). The variable capacitance ( $C_3$ ) given by the interdigital electrodes was designed for 0.49 pF. As discussed in Chapter 6, it was estimated that

the nominal capacitance of the fabricated capacitor was close to 0.5 pF which is what was expected. The problem was that the magnitude  $C_1 = 0.75$  pF and  $C_2 = 1.5$  pF were much larger than the actual variable capacitance given by  $C_3$ . Therefore,  $C_1$  and  $C_2$  dominated the resonant circuit and prevented the small change in  $C_3$  from shifting the resonant frequency.

In order to address the problem of the parasitic capacitances created by the non-conductive or regular epoxy, it was suggested reducing the length of the top rail as well as increasing the thickness of the kapton tape to decrease these capacitances. By shortening the top rail and thickening the dielectric, the parasitic capacitances would shrink since, by a basic parallel capacitor theory, the distance between the top rail and the ground plane was increased and the area where the top rail and the titanium substrate decreases because of the shorter length. Figure E.2 shows a schematic of changes proposed to address the parasitic capacitances.

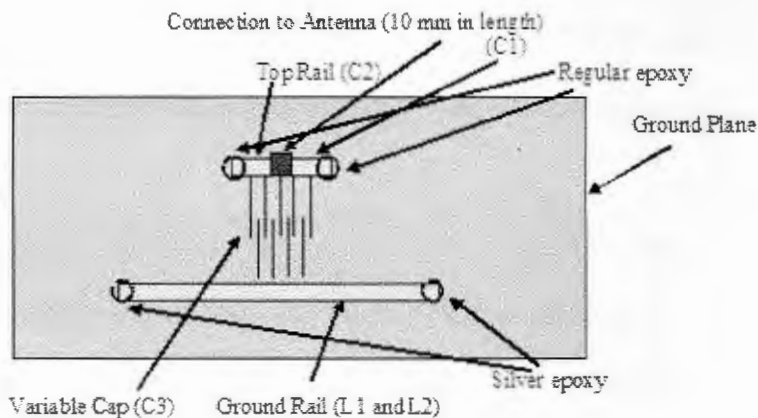


Figure E.2 Schematic of modified buckled beam capacitor

Unfortunately, the down side of these changes is that by shortening the top rail, the buckled beam amplification scheme modified. In this case, only the bottom rail

would contribute to change of capacitance. But the biggest concern of these modifications was that, if the buckled beam capacitor was arranged in a horizontal position with respect to the axis of strain, the non-conductive epoxy was not going to be able to hold the top electrode to the titanium beam. This is that, since there is no buckled beam, the top rail would tend to elongate as strain is apply to the substrate. So in order to corroborate that the changes in the design were going to decrease the base capacitances, the buckled beam capacitor was rotated 90°, so that now the capacitor is perpendicular to the axis of strain. The fabricated capacitor is shown in Figure E.3.

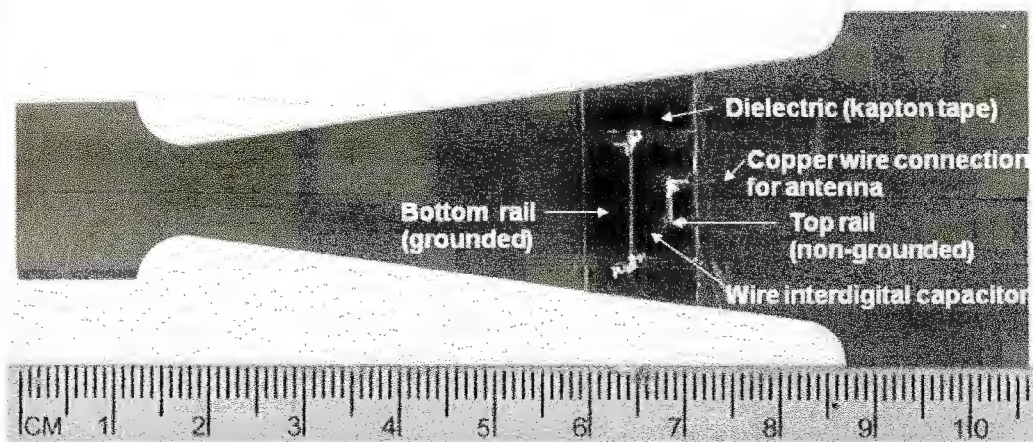


Figure E.3 Fabricated capacitor with non-buckled shorter rails

As seen in the figure above, the buckled beams of the bottom rail were also cut-off to make sure strain was transferred adequately. The fabrication steps were the same as for the original design with the exception that this time, instead of only 1 layer of kapton tape, 8 layers were placed to thickening the dielectric up to 200  $\mu\text{m}$ . The overlapping length was also increased to 500 $\mu\text{m}$  to increase the variable base capacitance ( $C_3$ ) to 0.62 pF. The diameter and space between the interdigital wires



was the same as in the original design. Results of these modifications are discussed in Chapter 6.

In addition to the previous modifications, a third design was proposed to address the issue of the large globs of silver epoxy used to hold the bottom rail to the titanium substrate. Also, the number of interdigital fingers was increased from 16 to 60 to increase the variable base capacitance (C3) and the overlapping length was about 300  $\mu\text{m}$ . Using equation (9), C3 is given by:

$$C3 = \frac{\pi(1)(8.85 \times 10^{-12})(300 \times 10^{-6})(60-1)}{\ln\left(\frac{(60 \times 10^{-6} - 25 \times 10^{-6})}{25 \times 10^{-6}}\right)} = 1.46 \text{ pF}$$

The greatest modification was the substitution of silver epoxy with a difference approach. This time, instead of using a drop of silver epoxy, a laser-welding machine was used to attach the bottom rail to the titanium substrate. The fabrication procedure was once again similar to the steps followed by the other two designs: the titanium substrate was cleaned up using sanding paper, and then 8 layers of kapton tape were placed. The buckled beam scheme was used again since the bottom rail was attached by laser-welding, while the top beam still used non-conductive epoxy. This time, the non-conductive epoxy deposited was a smaller drop so it would not spread out to form large capacitances. Figure E.4 shows the fabricated buckled beam capacitor with 60 interdigital fingers and using a laser-welding approach.

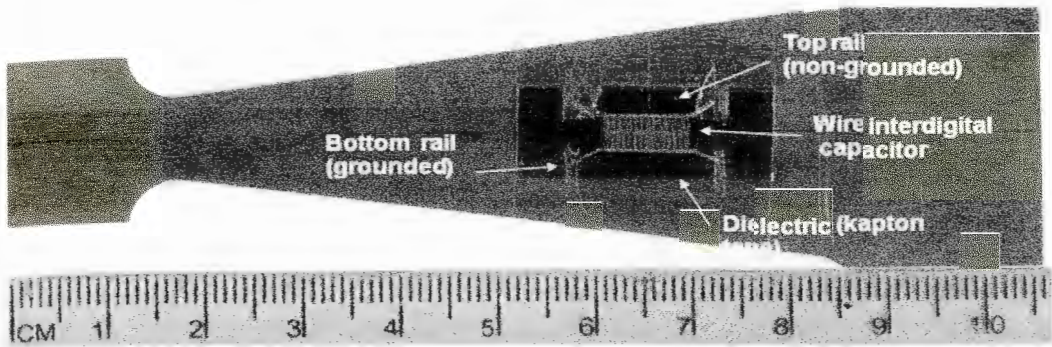


Figure E.4 Fabricated buckled beam capacitor with 60 interdigital fingers

Several parameters can be modified in the laser-welding machine to achieve a better joint: the profile of the laser beam, the aperture, the frequency, the voltage, the time and the energy of the laser beam among others. All these parameters and some other observations are discussed in Appendix F.

## APPENDIX F Laser-welding machine parameters

Profile	Voltage (V)	Time (ms)	Freq. (Hz)	Φ (nm)	Aperture (mm)	Average E (J)	Raw E (J)	Est. Pulse E (J)	Ref.
Pyramid	240	4.0	2.0	0.40	No	3.147	3.160	3.78	1*
							3.120		
							3.160		
Basic	219	3.6	2.0	0.45	No	3.410	3.420	3.55	1*
							3.410		
							3.400		
Pyramid	243	3.6	2.0	0.45	No	2.977	2.980	3.91	1*
							2.980		
							2.970		
Pyramid	175	3.0	2.0	0.30	No	0.439	0.442	1.13	2*
							0.442		
							0.432		
Pyramid	165	3.0	2.0	0.20	No	0.245	0.253	0.94	3*
							0.242		
							0.240		
Pyramid	225	3.5	2.0	0.40	No	1.897	1.917	2.75	4*
							1.900		
							1.875		
Pyramid	165	3.0	1.5	0.20	No	0.242	0.246	0.94	5*
							0.242		
							0.239		
Pyramid	155	3.0	1.5	0.15	No	0.112	0.114	0.78	6*
							0.111		
							0.111		
Pyramid	168	3.0	1.5	0.10	No	0.277	0.283	1.00	7*
							0.274		
							0.275		

\*Comments:

1. No aperture needed. Parameters used to join thick Ti beam and thin Ti shim with a single laser shot.
2. No aperture used. Parameters used to join to pieces of Ti.
3. No aperture used. Parameters used to join thick Ti beam and thin Ti shim using multiple laser shots at an angle of 45°).
4. No aperture used. Parameters used to join thick Ti beam and thin Ti shim using a single laser shot.
5. No aperture used. Parameters used to join thin Ti shim and Tu wire.

6. No aperture used. Parameters used to join thin Ti shim to diode.
7. No gas, no aperture used. Parameters used to join ground rail to thick Ti beam.

\*Ti needs Argon at 40 psi.

## APPENDIX G Fabricated antenna gage prototypes with modified parameters

Figures G.1 and G.2 show the fabricated prototypes using longer antenna wires and 3 additional kapton tape layers to increase the height of the antenna.

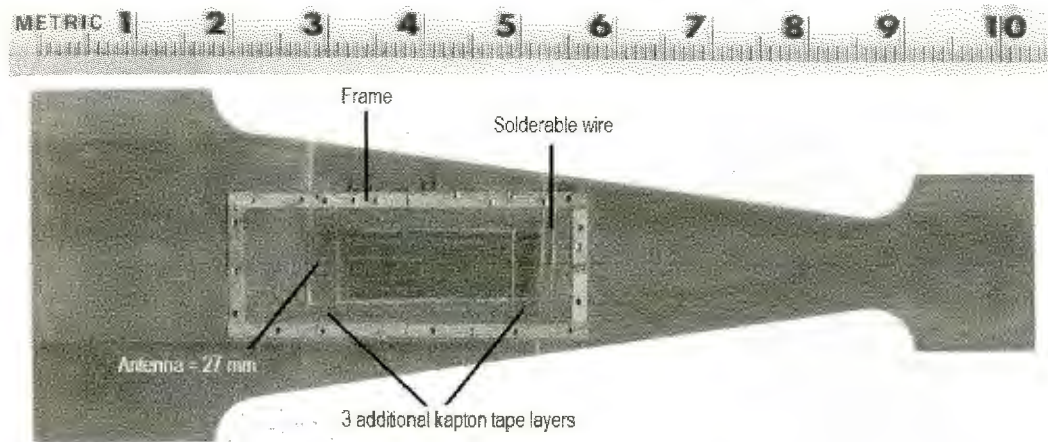


Figure G.1 Modified antenna gage with solderable wire

The prototype shown in the figure above did not include a diode; instead a solderable wire used to attach an external diode was connected to the antenna wire. The figure below includes a diode and a layer of copper tape between the diode and the substrate for better contact.

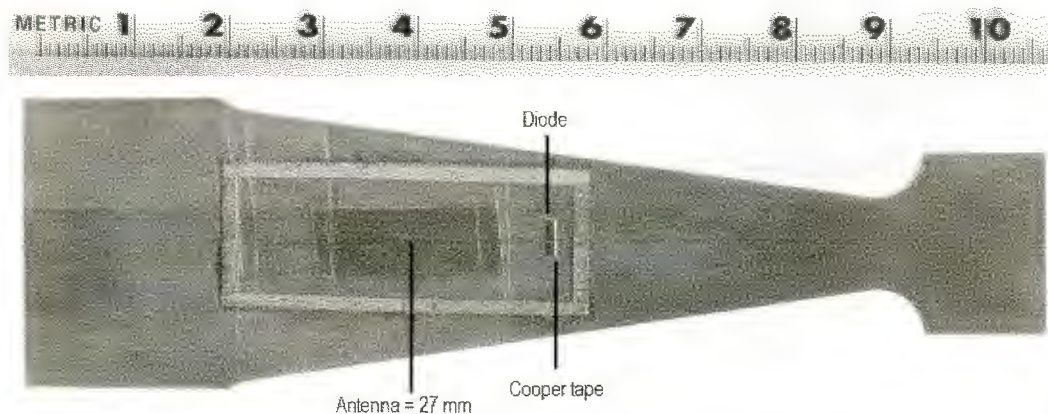


Figure G.2 Modified antenna gage with solderable wire



## APPENDIX H Frequency shift vs deflection for antenna strain gage

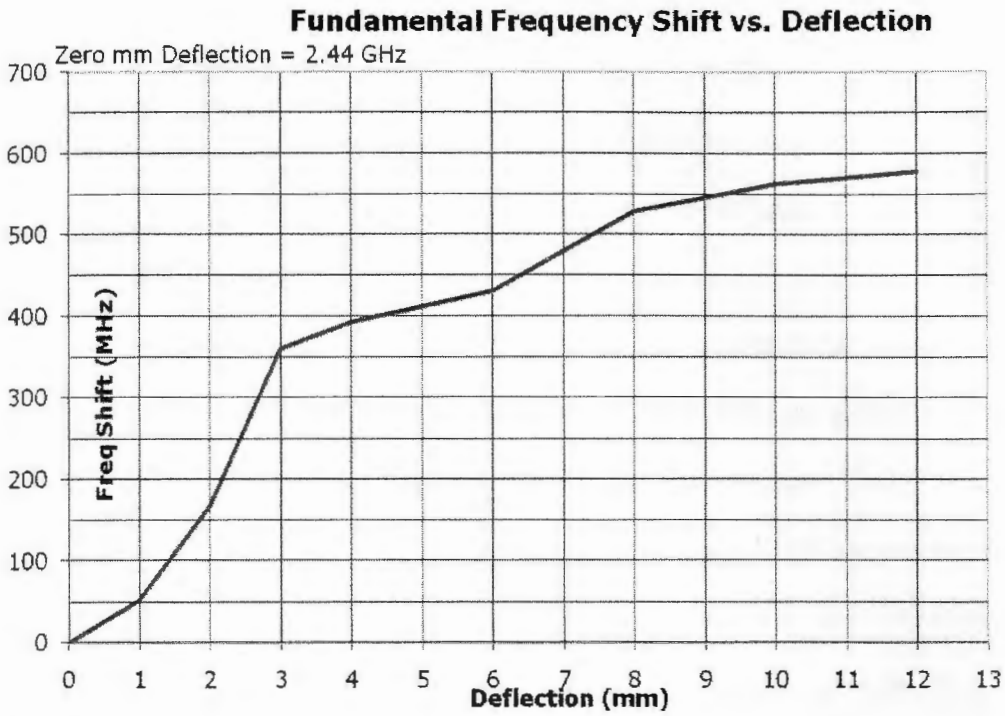


Figure H.1 Frequency shift vs deflection for antenna gage

The figure above shows that the response of the antenna gage remains almost constant until it reaches more than 4mm of deflection. This means that the gage factor remains above a 1000 up to 160  $\mu$ strain or a deflection of 4mm; beyond that point the gage factor falls below 1000, with a minimum value about 546 when deflected 12 mm or 480  $\mu$ strain. Still the gage factor is very large as compared to the previous approaches.

## **APPENDIX I Additional antenna gage measurement details**

Tx amplifier output: +23.5 dBm (224 mW). This is the output power at the fundamental freq (about 2.45 GHz). Tx antenna gain at 2.45 GHz: +6.3 dBi. So, the total ERP (effective radiated power) is almost 1 watt (+29.8 dBm).

The antenna strain gage was located 6" from the Tx antenna. The antenna gage prototype had a gain at 2.45 GHz: -11.5 dBi (only 7% efficiency losing a lot of performance here).

The Tx signal produced about 350  $\mu$ W at the antenna gage terminal (about 2.6 mV in 50 ohms). The 2nd harmonic generated by the 2.6 mV from the external diode is about -32 dBm. This is the signal that is re-radiated by antenna gage.

The antenna gage prototype had a gain at 4.9 GHz: about -9 dBi (a little higher at 5 GHz than at 2.45 GHz). The -32 dBm second harmonic input to the -9 dBi antenna produced about -65 dBm at the output of the Rx horn antenna at a 6" range. (The Rx antenna gain is +8 dBi).

## Bibliography

- Alam, K. 2001. SAW Devices for Integrated Applications. *Microelectronic Engineering Research Conference*.
- Atashbar, M. Z., B. J. Bazuin, and S. Krishnamurthy. 2003. Design and simulation of SAW sensors for wireless sensing. *Proceedings of IEEE Sensors 1*: 584 – 589.
- Atashbar, M. Z., B. J. Bazuin, and S. Krishnamurthy. 2003. Design Steps for prototyping smart SAW sensors and a burst transceiver for interrogation. *Proceedings of IEEE Electro Information Technology Conference, Session 4C*.
- Auld, B. A. 1990. *Acoustic Fields and Waves in Solids*. Malabar, FL: Krieger.
- Bates, S. 1999. Fiber Optic Slip Ring. *Thoughtventions Unlimited LCC (TvU) Research Paper*.
- Beckley, J., V. Kalinin, M. Lee, and K. Voliansky. 2002. Non-contact torque sensors based on SAW resonators. *IEEE International Frequency Control Symposium and PDA Exhibition*: 202 – 213.
- Bell Jr., D. T. and R. C. M. Li. 1976. Surface-Acoustic-Wave Resonators. *Proceedings of the IEEE* 64(5): 711 -721.
- Brady, D. 2002. The Design, Fabrication and Measurement of Microstrip Filter and Coupler Circuits. *High Frequency Electronics* : 22 – 30.
- Buff, W. 2002. SAW sensors for direct and remote measurements”, *Proceedings of IEEE Ultrasonics Symposium 1*: 420-428.
- Buff, W., F. Plath, O. Schmeckeber, M. Rusko, T. Vandahl, H. Luck, F. Moller and D. C. Malocha. 1994. Remote Sensor System using Passive SAW Sensors. *Proceedings of IEEE Ultrasonics Symposium 1*: 585 – 588.
- Bulst, W. E. and C. Ruppel, 1994. Developments to watch in SAW technology. *Siemens Review* : 2 – 6.

Campbell, C. 1989. *Surface Acoustic Wave Devices and Their Signal Processing Applications*. Boston: Academic.

Coquin, G. A. and H. F. Tiersten. 1966. Analysis of the Excitation and Detection of Piezoelectric Surface Waves in Quartz by Means of Surface Electrodes. *The Journal of the Acoustical Society of America* 5.4: 921 – 939.

Das, P., C. Lanzi, and D. Barone. 1978. A surface acoustic wave transmitting hydrophone. *Proceedings of IEEE Ultrasonics Symposium*: 458 – 463.

DeAnna, R. G. 2000. *Wireless Telemetry for Gas-Turbine Applications*. U. S. Army Research Laboratory, Glen Research Center, Cleveland, Ohio, NASA/TM - 2000-209815.

Farnell, G. W., I. A. Cermak, P. Silvester, and S. K. Wong. 1970. Capacitance and Field Distribution for Interdigital Surface-Wave Transducers. *IEEE Transactions on sonics and ultrasonics* 17(3): 188 – 195.

Galipeau, D. W., P. R. Story, K. A. Vetelino, and R. D. Mileham. 1997. Surface acoustic wave microsensors and applications. *Smart Materials and Structures* 6: 658 – 667.

Gardner, J. W., W. K. Varadan, and O. O. Awadelkarim. 2001. *Microsensors MEMS and Smart Devices*. England: Wiley.

Gianchandani, Y. B. and K. Najafi. 1996. Beant-beam strain sensors. *IEEE Journal of Micro Electro Mechanical Systems*: 5(1): 52 – 58.

Gregory, O. J. and Q. Luo. 2000. Ceramic strain gages for propulsion health monitoring. *Proceedings of the 19<sup>th</sup> Digital Avionics Systems Conference 2*: 6E2/1 – 6E2/8.

Grossmann, R., J. Michel, T. Sachs, and E. Schrüfer. 1996. Measurement of mechanical quantities using quartz sensors. *IEE European Frequency Time Forum* 418.

- Guo, J., H. Kuo, D. J. Young, and W. H. Ko. 2004. Buckled beam linear output capacitive strain sensor. *Solid State Sensor, Actuator, and Microsystems Workshop*: 344 – 347.
- Guo, J., M. Suster, D. J. Young, and W. H. Ko. 2005. High-gain Mechanically Amplified Capacitive Strain Sensor. *IEEE Sensors*: 464 – 467.
- Hamsch, M., R. Hoffmann, W. Buff, M. Binhack, and S. Klett. 2004. An Interrogation Unit for Passive Wireless SAW Sensors Based on Fourier Transform. *IEEE Transactions on Ultrasonics, Ferroelectrics, and Frequency Control* 51(11): 1449 – 1456.
- Hoummady, M., A. Campitelli, and W. Wlodarski. 1997. Acoustic wave sensors: design, sensing mechanisms and applications. *Smart Materials and Structures* 6: 647 – 657.
- Joshit, S. G. and M. White. 1968. Excitation and detection of Surface Elastic Waves in Piezoelectric Crystals. *The Journal of the Acoustical Society of America* 5.18: 19 – 27.
- Kadota, M., J. Ago, H. Horiuchi, and M. Ikeura. 2002. Very Small IF Resonator Filters Using Reflection of Shear Horizontal Wave at Free Edges of Substrate. *IEEE Transactions on Ultrasonics, Ferroelectrics, and Frequency Control*: 49(9): 1269 – 1279.
- Kalinin, V. 2004. Passive Wireless Strain and Temperature Sensors Based on SAW Devices. *IEEE Radio and Wireless Conference*: 187 – 190.
- Kalinin, V., G. Bown, J. Beckley, and R. Lohr. 2004. Pulsed Interrogation of the SAW Torque Sensor for Electrical Power Assisted Steering. *IEEE International Ultrasonics, Ferroelectrics, and Frequency Control Joint 50<sup>th</sup> Anniversary Conference* 3: 1577 – 1580.
- Kushibiki, J., I. Takanaga, and S. Nishiyama. 2002. Accurate Measurements of the Acoustical Physical Constants of Synthetic a-Quartz for SAW Devices. *IEEE Transactions on Ultrasonics, Ferroelectrics, and Frequency Control* 40(1): 125 – 135.



- Matsuzaki, R. and A. Todoroki. 2005. Passive wireless strain monitoring of tyres using capacitance and tuning frequency changes. *Smart Materials and Structures* 14: 561 – 568.
- Matsuzaki, R. and A. Todoroki. 2006. Passive wireless strain monitoring of actual tire using capacitance-resistance change and multiple spectral features. *Sensors and actuators A* 126(20): 277 – 286.
- Morgan, D. P. 1973. Surface acoustic wave devices and applications. *IEE Ultrasonics* 11: 121 – 131.
- Morgan, D. P. 1991. *Surface-Wave Devices for Signal Processing*. Amsterdam: Elsevier.
- Nysen, P. A., H. Skeie, and D. Armstrong, 1983 - 1986. System for interrogating a passive transponder carrying phase-encoded information". *U.S. Patent* 4 725 841; 4 635 207; 2 625 208.
- Pohl, A. and F. Seifert. 1997. Wirelessly Interrogable Surface Acoustic Wave Sensors for Vehicular Applications. *IEEE Transactions on Instrumentation and Measurement* 46(4): 1031 – 1038.
- Pohl, A. G. Ostermayer, and F. Seifert. 1998. Wireless Sensing Using Oscillator Circuits Locked to Remote High-Q SAW Resonators. *IEEE Transactions on Ultrasonics, Ferroelectrics, and Frequency Control* 45(5): 1161 – 1168.
- Pohl, A., G. Ostermayer, L. Reindl, and F. Seifert. 1997. Monitoring the tire pressure at cars using passive SAW sensors. *Proceedings of IEEE Ultrasonics Symposium* 1: 471 – 474.
- Pratt and Whitney. 1982. *The aircraft Gas Turbine Engine and its operation*. New York: Pratt and Whitney United Technologies.
- Precision Acoustics LTD. 2007. Properties of Poled Piezo-electric PVDF film <http://www.acoustics.co.uk/static/pdf/PVdF-properties.pdf> (accessed July 29, 2007).

- Reindl, L. G. Scholl, and T. Ostetag. 1998. Theory and Application of Passive SAW Radio Transponders as Sensors. *IEEE Transactions on Ultrasonics, Ferroelectrics, and Frequency Control*: 45(5): 1281 – 1292.
- Reindl, L. M. and A. Pohl. 2001. SAW-Based Radio Sensor Systems. *IEEE Sensors Journal* 1(1): 69 – 78.
- Roh, Y., V. V. Varadan, and V. K. Varadan. 2002. Characterization of All the Elastic, Dielectric, and Piezoelectric Constants of Uniaxially Oriented Poled PVDF Films. *IEEE Transactions on Ultrasonics, Ferroelectrics, and Frequency Control* 49(6): 836 -847.
- Schmidt, F., O. Sczesny, L. Reindl, and F. Seifert. 1994. Remote sensing of physical parameters by means of passive surface acoustic wave devices (“ID-tag”). *Proceedings of IEEE Ultrasonics Symposium* 1: 589-592.
- Smith, W. R., H. M. Gerard, J. H. Collins, T. M. Reeder, and H. J. Shaw. 1969. Analysis of Interdigital Surface Wave Transducers by Use of an Equivalent Circuit Model. *IEEE Transactions on Microwave Theory and Techniques*: 17(11): 856 -864.
- Smith, W. R., H. M. Gerard, J. H. Collins, T. M. Reeder, and H. J. Shaw. 1969. Design of Surface Wave Delay Lines with Interdigital Transducers. *IEEE Transactions on Microwave Theory and Techniques*: 17(11): 865 -873.
- Sun, S. and L. Zhu. 2005. Compact Dual-Band Microstrip Bandpass Filter Without External Feeds. *IEEE Microwave and Wireless Components Letters* 15(10): 644 – 646.
- Suster, M., D. J. Young, and W. H. Ko. 2002. Micro-power wireless transmitter for high-temperature MEMS sensing and communication applications. *The Fifteenth IEEE International Conference on Micro Electro Mechanical Systems*: 641 – 644.
- Suster, M., J. Guo, N. Chaimanonart, W. H. Ko, and D. J. Young. 2006. A High-Performance MEMS Capacitive Strain Sensing System. *Journal of Microelectromechanical Systems* 15(5): 1069 – 1077.

- Suster, M., N. Chaimanonart, J. Guo, W. H. Ko, and D. J. Young. 2005. Remote-Powered High-Performance Strain Sensing Microsystem. *IEEE International Conference on Micro Electro Mechanical Systems*: 255 – 258.
- Todoroki, A., S. Miyatani, and Y. Shimamura. 2003. Wireless strain monitoring using electrical capacitance change of tire: part I – with oscillating circuit. *Smart Materials and Structures* 12: 403 – 409.
- Todoroki, A., S. Miyatani, and Y. Shimamura. 2003. Wireless strain monitoring using electrical capacitance change of tire: part II – passive. *Smart Materials and Structures* 12: 410 – 416.
- Varadan, V. V., V. K. Varadan, X. Bao, S. Ramanathan, and D. Piscotty. 1997. Wireless passive IDT strain microsensor. *Smart Materials and Structures* 6: 745 -751.
- White, R. M. and F. W. Voltmer. 1965. Direct piezoelectric coupling to surface elastic waves. *Applied Physics Letters* 7(12): 314 – 316.
- Wolff, U., F. Schmidth, G. Scholl, and V. Mágori. 1996. Radio accessible SAW sensors efor non-contact measurement of torque and temperature. *Proceedings of IEEE Ultrasonics Symposium* 1: 359 – 362.
- Wright, P. V. 1992. A review of SAW resonator filter technology. *Proceedings of IEEE Ultrasonics Symposium* 1: 29 – 38.
- Young, D. J. and W. H. Ko. 2004. A High-Performance Strain Sensing Microsystem with Remote RF Power Capability. *Proceedings of the 7<sup>th</sup> International Conference on Solid-State and Integrated Circuits Technology* 3: 1677- 1682.